Subsurface CO_2 dynamics in a temperate karst system reveal complex seasonal and spatial variations

Sarah Rowan[1,2], Marc Luetscher[3], Thomas Laemmel[1,2], Anna Harrison[4], Sönke Szidat[1,2], Franziska A Lechleitner[1,2]

[1] Department of Chemistry, Biochemistry, and Pharmaceutical Sciences, University of Bern, 3012, Bern, Switzerland.
[2] Oeschger Centre for Climate Change Research (OCCR), University of Bern, 3012, Bern, Switzerland
[3] Swiss Institute of Speleology and Karst Studies, 2300, La Chaux-de-Fonds, Switzerland.
[4] Institute of Geological Sciences, University of Bern, 3012, Bern, Switzerland.

Correspondence to: Sarah Rowan (sarahrowan96gmail.com)

Abstract. Understanding the carbon cycle of the terrestrial Critical Zone, extending from the tree canopy to the aquifer, is crucial for accurate quantification of its total carbon storage and for modelling terrestrial carbon stock responses to climate change. Caves and their catchments offer a natural framework to sample and analyse carbon in unsaturated zone reservoirs across various spatial and temporal scales. In this study, we analyse the concentration, stable carbon isotopic ratio ($\delta^{13}C$), and radiocarbon (^{14}C) compositions of CO_2 from the atmosphere, boreholes (0.5 to 5 m depth), and cave sampled every two months over two years at Milandre cave in northern Switzerland. High concentrations of up to ~~35'000~~35,000 ppmV CO_2 are measured in the boreholes. The $\delta^{13}C$ values of CO_2 in the boreholes reflect the $\delta^{13}C$ of C3 plants (~ -26 ‰) which dominate the catchment ecosystem. Shallow meadow boreholes host older CO_2 in winter and modern CO_2 in summer, while forest ecosystems consistently export modern CO_2 ($F^{14}C$ = ~1) to the unsaturated zone. Cave CO_2 concentrations exceed atmospheric levels and are diluted by temperature-driven seasonal ventilation. Keeling plot intercepts indicate that the cave CO_2, which mixes with atmospheric CO_2, is younger in summer ($F^{14}C$ = 0.94) and older in winter ($F^{14}C$ = 0.88), with a $\delta^{13}C$ consistent with the C3 plant dominated catchment. Mixing models utilising drip water dissolved inorganic carbon ^{14}C suggest that varying carbonate dissolution and degassing dynamics do not explain the $F^{14}C$ variation and concurrent $\delta^{13}C$ stability of the mixing endmember. Rather, contributions from ~~deeper~~ aged carbon reservoirs in the ~~epikarst~~deeper unsaturated zone are likely. This study provides valuable insights into CO_2 source dynamics and cycling within the karstic Critical ~~Zones~~Zone, highlighting the impact of seasonal variations and ecological factors on downward carbon export from terrestrial ecosystems.

30

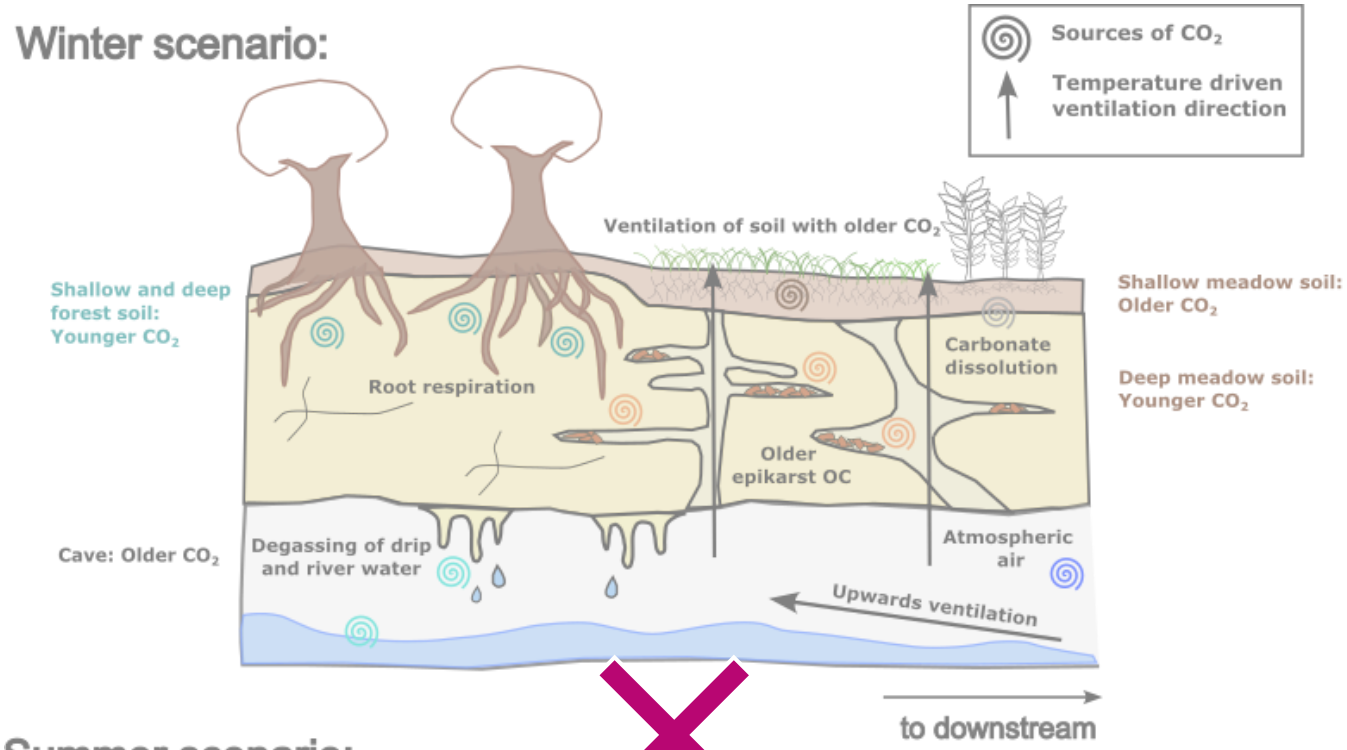
Winter scenario:
Sources of CO_2
Temperature driven ventilation direction
Ventilation of soil with older CO_2
Shallow and deep forest soil: Younger CO_2
Shallow meadow soil: Older CO_2
Carbonate dissolution
Deep meadow soil: Younger CO_2
Root respiration
Older epikarst OC
Cave: Older CO_2
Degassing of drip and river water
Atmospheric air
Upwards ventilation
to downstream

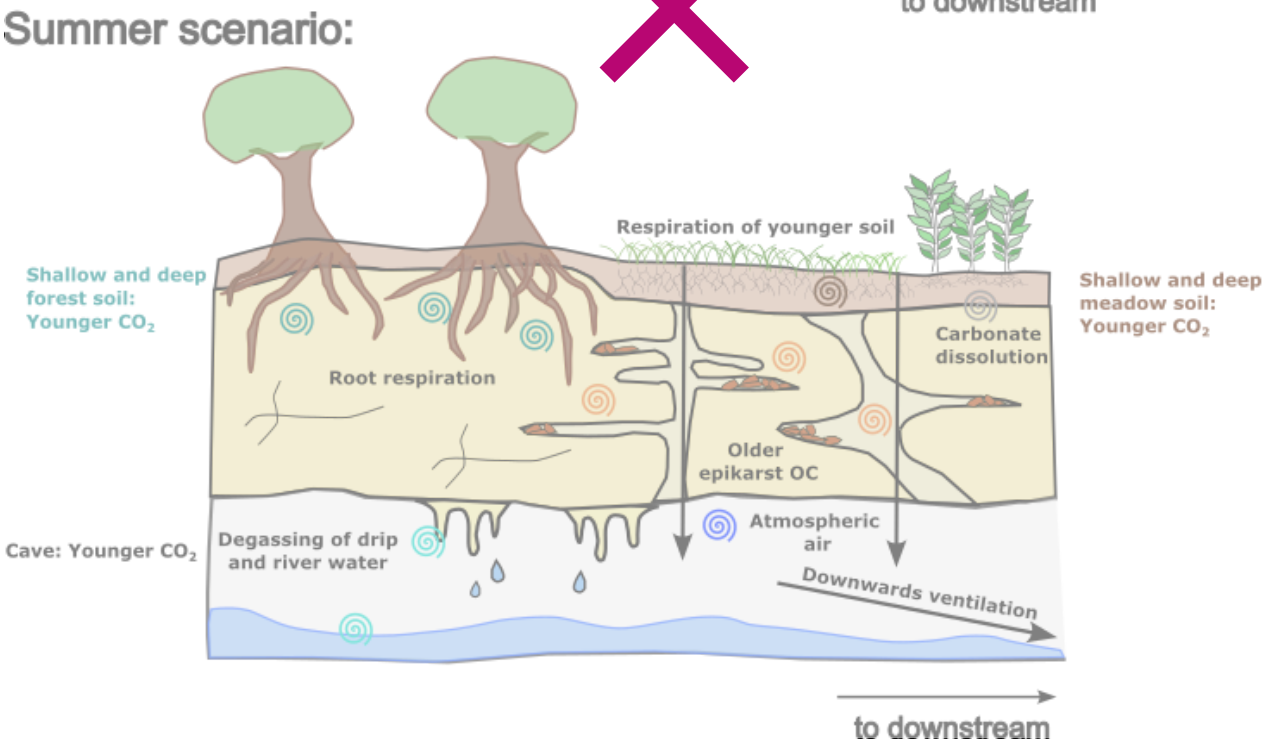
Summer scenario:
Respiration of younger soil
Shallow and deep forest soil: Younger CO_2
Shallow and deep meadow soil: Younger CO_2
Carbonate dissolution
Root respiration
Older epikarst OC
Cave: Younger CO_2
Degassing of drip and river water
Atmospheric air
Downwards ventilation
to downstream

31

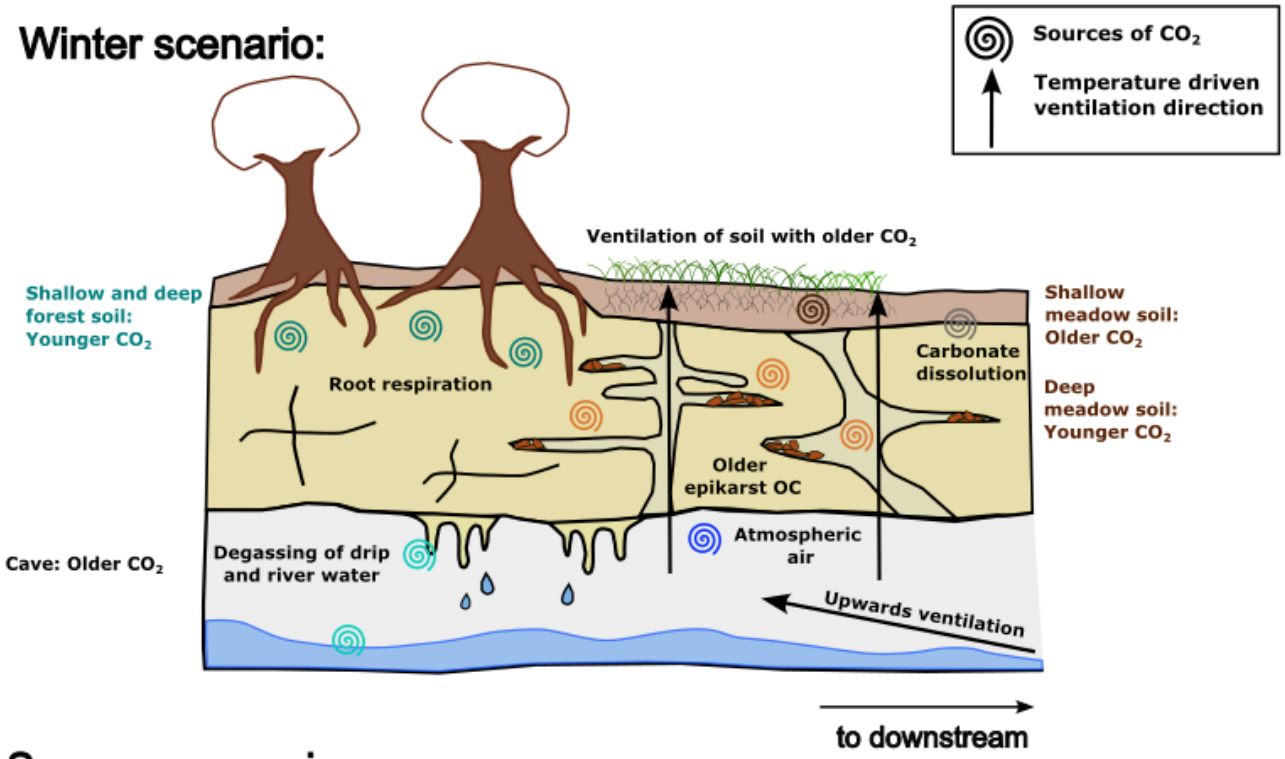
Winter scenario:
Sources of CO_2
Temperature driven ventilation direction
Ventilation of soil with older CO_2
Shallow and deep forest soil: Younger CO_2
Shallow meadow soil: Older CO_2
Carbonate dissolution
Root respiration
Deep meadow soil: Younger CO_2
Older epikarst OC
Atmospheric air
Cave: Older CO_2
Degassing of drip and river water
Upwards ventilation
to downstream

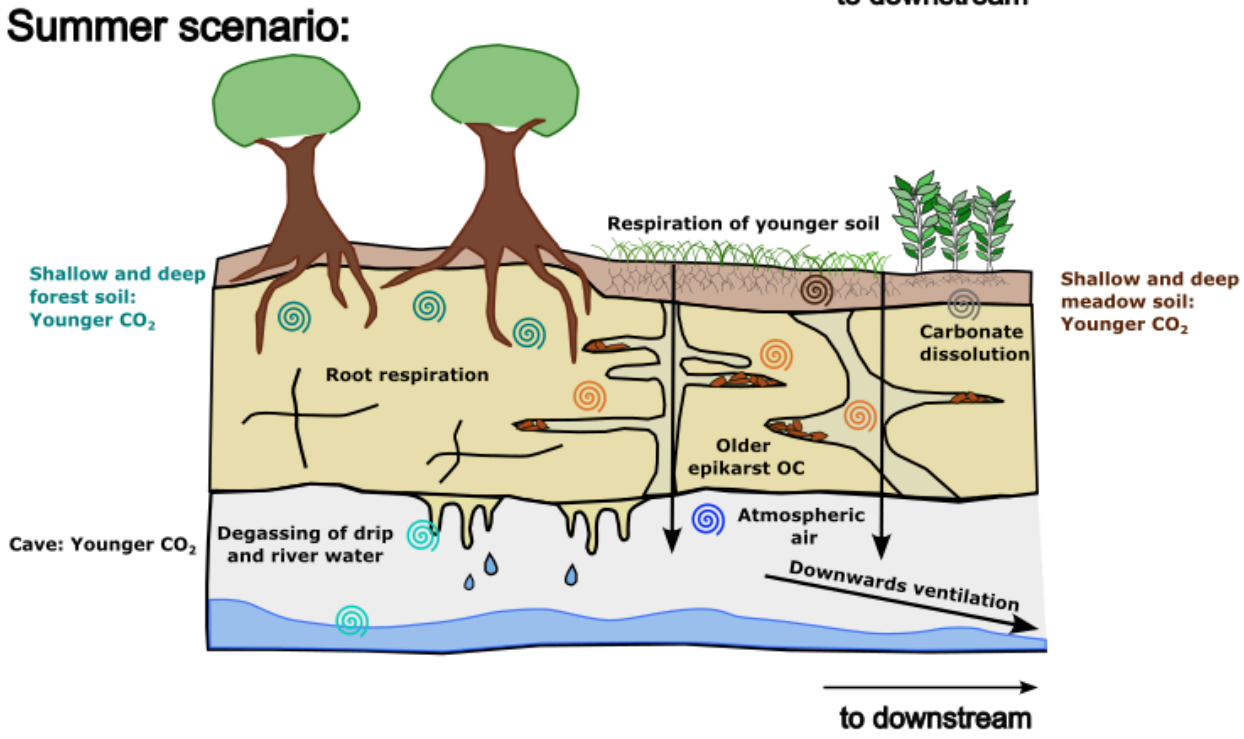
Summer scenario:
Respiration of younger soil
Shallow and deep forest soil: Younger CO_2
Shallow and deep meadow soil: Younger CO_2
Carbonate dissolution
Root respiration
Older epikarst OC
Atmospheric air
Cave: Younger CO_2
Degassing of drip and river water
Downwards ventilation
to downstream

1 Introduction

Within the context of current and future ~~changing climate~~climate change, investigations into the response of Critical Zone carbon pools to rising temperatures and changing hydroclimatic conditions are crucial (Brantley et al., 2007). Recent studies have specifically highlighted the unsaturated zone as a potentially important but poorly constrained reservoir of gaseous CO_2 (Mattey et al., 2016; Noronha et al., 2015; Keller, 2019; Stewart et al., 2022). Estimates suggest that between 2 to 53 PgC could be present in the form of CO_2 in the unsaturated zone globally (Baldini et al., 2018). This carbon is particularly vulnerable to changes in the water table level, whereby rises may easily result in the rapid release of CO_2 into the atmosphere (Baldini et al., 2018). Despite its importance, comprehensive assessments integrating spatial and temporal variability of shallow subsurface CO_2 remain scarce.

Understanding unsaturated zone CO_2 dynamics is complicated by the different sources of carbon contributing to the subsurface reservoir. The CO_2 present in the unsaturated zone is often referred to as ground air and was first defined as CO_2 produced by microbial oxidation of organic material which was transported from the surface (Atkinson, 1977). However, ground air can also refer more generally to high CO_2 concentrations in the subsurface, without linking its presence to a particular source. Early evidence for the presence of a ground air reservoir was the observation of high CO_2 concentrations found in deep cave passages with poor connection to the catchment surface, suggesting an endogenous source of CO_2 (McDonough et al., 2016). The age profile of this high concentration CO_2 reservoir, however, varies by site, suggesting significant variability in its source and processing. ~~Exclusively aged CO_2 reservoirs~~CO_2 reservoirs of a lower $F^{14}C$, corresponding to an older age, have been reported (Breecker et al., 2012; Noroha et al., 2015; Mattey et al., 2016; Bergel et al., 2017), as well as modern subsurface CO_2 pools, likely derived from ecosystem respiration of recently fixed carbon (Campeau et al., 2019; Tune et al., 2020). Consequently, the primary sources of subsurface CO_2 generally considered are 1) the outside atmosphere (Kukuljan et al., 2021), 2) catchment soil and vegetation respiration (Breecker et al., 2012; Li et al., 2024), 3) microbial respiration in the unsaturated zone (Mattey et al., 2016; Ravn et al., 2020), 4) carbon dissolved from the carbonate bedrock (Milanolo & Gabrovšek, 2015), and 6) volcanic and metamorphic hydrothermal input (Chiodini et al., 2008; Girault et al., 2018).

Carbon isotope analysis of CO_2 can be used to differentiate the contributing sources to the subsurface gas mixture. Specifically, the $\delta^{13}C$ of CO_2 in the unsaturated zone can provide information about the influence of biological fractionation by overlying catchment vegetation and ~~respiration by microorganisms~~microbial respiration, and the influence of carbonate dissolution and subsequent degassing (Breecker et al., 2017, McDonough et al., 2016). In addition, due to the contrast between the ^{14}C content of biospheric carbon, which ranges from bomb peak enriched to >~~10'000~~10,000 years old, and carbonate rock which is typically radiocarbon dead, ^{14}C ~~measurement~~measurements of subsurface CO_2 can provide information for both source apportionment and carbon turnover rates in the terrestrial subsurface (Noronha et al., 2015).

Though there has been extensive work investigating unsaturated zone CO_2 reservoirs, questions remain about the concentration, composition and sources of ground air on temporal and spatial scales. This study seeks to address this gap by presenting a detailed assessment of CO_2 concentrations and isotopic compositions over 2 years within the Milandre cave karst system in Switzerland. We aim to 1) Determine the relationships between pCO_2, $\delta^{13}CO_2$, and $^{14}CO_2$ in Milandre cave and its catchment; 2) Assess the effect of seasonality on CO_2 concentration and isotopic characteristics and 3) Gain insights into the ~~provenances~~provenance of CO_2 and how these evolve over time.

2 Site Overview

Milandre cave (47.4852 ° N, 7.0161 ° E, 373m a.s.l.) is located in the municipality of Boncourt in the Jura canton, NW Switzerland (Fig. 1). The Milandre karst structure formed within the Jura mountains, a sub-alpine mountain range which lies laterally in a northwest-southeast direction. The cave is located within the external Plateau unit of the Jura mountains which consists of thin sub horizontal Mesozoic limestone units that have experienced deformation which produced imbricates and ~~tear~~strike-slip faults (Sommaruga, 2011). More specifically, the Milandre karst system formed within the Late Jurassic (Middle Oxfordian) St-Ursanne Formation which overlies Early to Middle Oxfordian marls (Jeannin, 1998). The unsaturated zone ranges between 40 and 80 m depth~~, with a saturated zone of ~ 20 m~~. The active karst level developed in the epiphreatic zone, with the underneath phreatic zone extending for ~ 20 m to reach the low permeable Lower Oxfordian marls (Liesberg Mb) (Perrin et al., 2003). The cave is formed over 2.7 km, with 10.5 km of galleries forming along N-S oriented fractures. The Milandre river flows for 4.5 km in a northerly direction in the lower part of the cave and exits via the perennial Saivu spring where it joins the Allaine River, and the Bame temporary spring. Clays and silts, deposited during hydraulic backflooding, are particularly present in the downstream part of Milandre cave where they contribute to the sediment load during mild flood events. In contrast, during medium to intense flow, allochthonous sediment transport is often associated with higher microbial concentrations (Vuilleumier et al., 2021). Quantifying the contribution of microbial respiration to the cave carbon cycle was beyond the scope of this study and should be addressed by future research. The Milandre river drains a catchment area of approximately 13 km^2 (Perrin et al., 2003). There is a series of dolines in the catchment area which form depressions ~~of~~ ~10 to 20 m deep in the landscape. Notably, one doline is located in the meadow partially covering the upstream section of Milandre cave (Fig. 1).

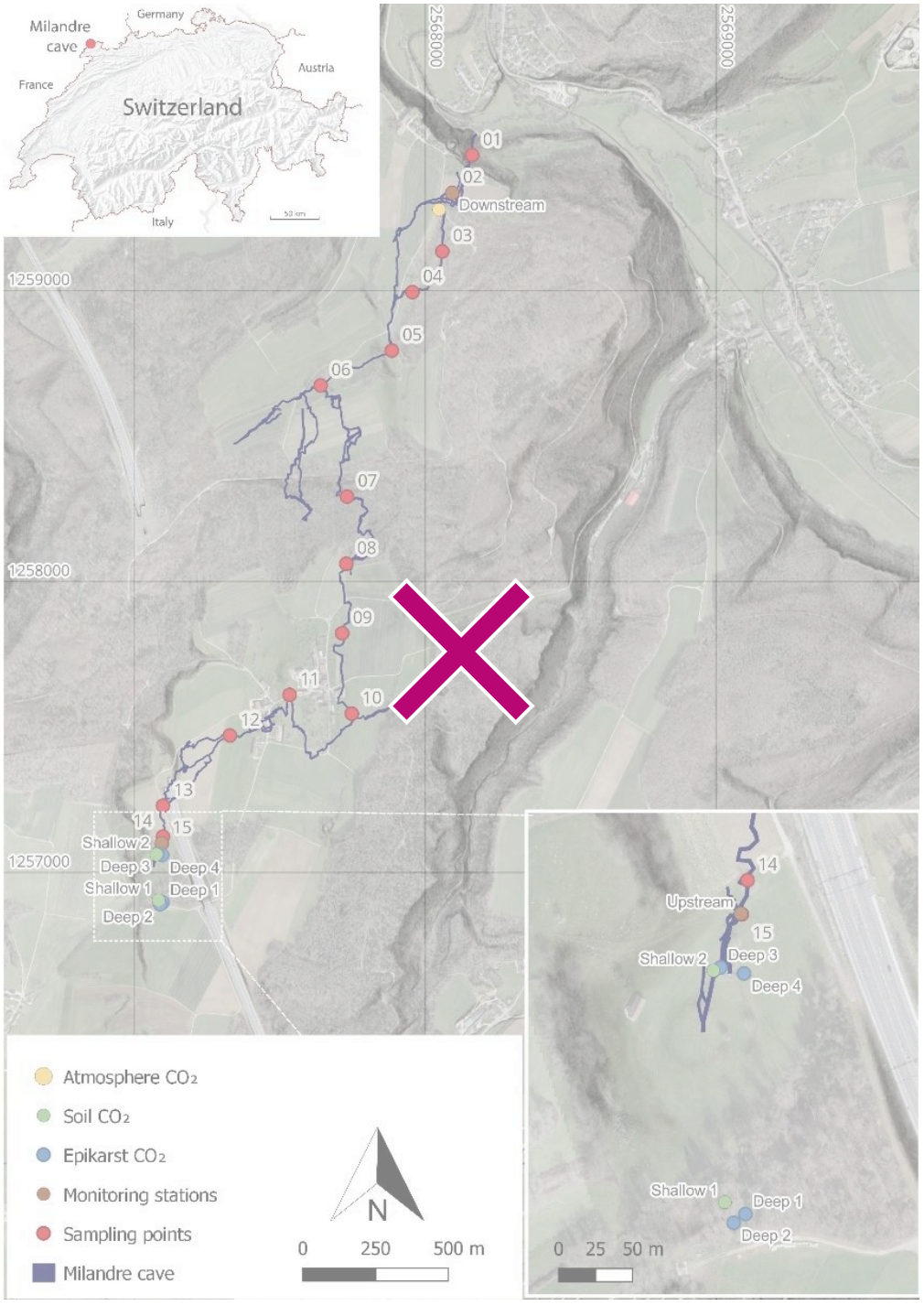
Milandre cave
Germany
France
Austria
Switzerland
Italy
2568000
2569000
1259000
1258000
1257000
01
02
Downstream
03
04
05
06
07
08
09
10
11
12
13
14
15
Shallow 2
Deep 3
Deep 4
Shallow 1
Deep 1
Deep 2
Upstream
Atmosphere CO2
Soil CO2
Epikarst CO2
Monitoring stations
Sampling points
Milandre cave
N
0 250 500 m
0 25 50 m

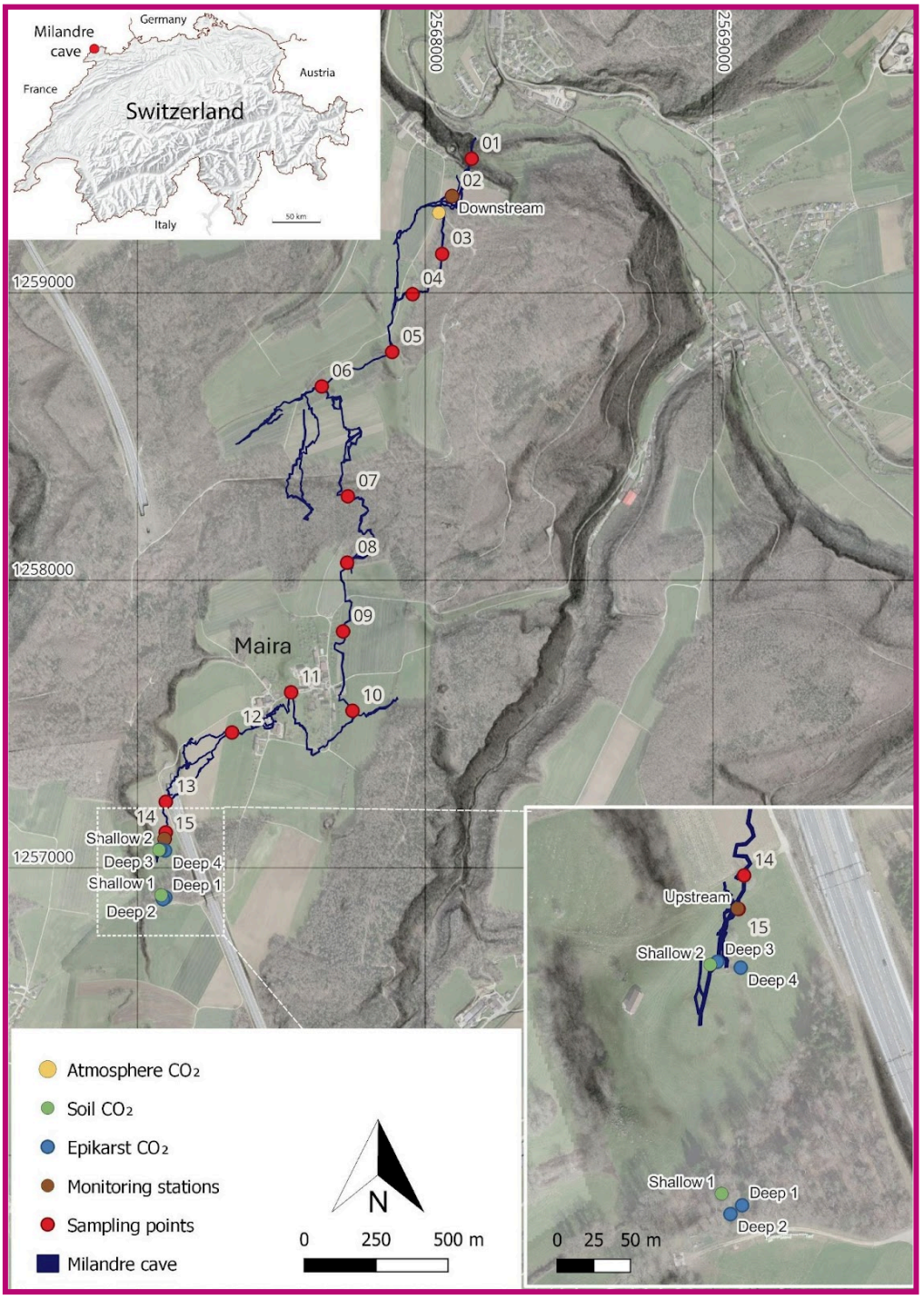

Figure 1. Map of the main passages of the Milandre cave network. The location of the atmospheric sampling (yellow), the soil (green) and ~~epikarst~~unsaturated zone boreholes (blue), and the cross-trip sampling (red) are annotated. Cave survey modified from Gigon & Wenger (1986). Base map from ©swisstopo.

Over the past 40 years, land use in the catchment area has been dominated by farmland (37 %), forest (36 %), and meadows (12 %) as estimated by aerial photo analysis (Jeannin et al., 2016). The crops grown primarily include maize and tobacco, two C4 plants. Long-term land use analysis shows that farmland has decreased slightly in this area and special infrastructures have increased due to the construction of a motorway that overlies part of the cave. The soils of the area are influenced by the ecosystem that is overlying it. Forest soils are shallow leptosols (< 10 cm deep) that are rich in fragments of the carbonate bedrock. The shallow forest soils transition into deeper (up to ~ 80 cm) organic rich histosols in the meadows, particularly in the dolines. The roots from the forest vegetation likely extend into the epikarst and unsaturated zone, however no roots are visible within the cave itself.

The Jura region experiences a marine west coast, warm summer climate (Cfb classification) (Kottek et al., 2006). Daily temperature measurements from the Fahy MeteoSwiss weather station located ~ 9.5 km SW from Milandre cave show ~~an average~~a mean temperature of 9.4 ˚C (1991 to 2020). Temperature seasonality is strong, with monthly ~~average~~mean temperatures fluctuating between a minimum of -1.2 ˚C in January and a maximum of 18.2 ˚C in July from 1991 to 2020 (MeteoSwiss, 2024). In contrast, temperatures within the cave remain almost constant year-round, and vary between 10.3~~-~~ and 11.0 ˚C (Affolter et al., 2020). The temperature difference between the outside and in-cave temperature drives dynamic ventilation on seasonal scales (Garagnon et al., 2022). Regional meteoric precipitation shows ~~an average of 1046~~a mean of 1,046 mm year^{-1}. Monthly precipitation data indicate that precipitation in this area is well dispersed throughout the year (MeteoSwiss, 2024). Monitoring of tritium (^{3}H) in stalagmite drip water was used to estimate the residence time of seepage water at ~ 5.5 to 6.6 years (Affolter et al., 2020).

3 Materials and methods

3.1 Gas sampling set up

All gas samples were taken every two months from December 2021 to January 2024. The samples were collected in 5 L sampling bags (Cali-5-Bond, Calibrated Instruments, USA) using a handheld pump. The gas was dried through a glass tube filled with granular magnesium perchlorate (~ 83 % purity, Supelco, Germany) to reduce the effects of humidity which may affect the isotopic composition of the sample. The sampling set up and procedure were identical for all gas samples. The CO_2 concentration was monitored during line flushing using ~~an in-house built NDIR~~a nondispersive infrared (NDIR) CO_2 sensor (SCD30, Sensirion, Switzerland) to ensure accurate sampling. The magnesium perchlorate was exchanged before each sampling day. Prior to analysis, the samples were stored away from direct sunlight in cool indoor temperatures for a maximum of six weeks. The same bags were reused for each sampling location and were flushed with N_2 gas for at least 48 h before sampling to reduce cross contamination risks.

Atmospheric samples were collected at a defined sampling site above the cave (Fig. 1). Before sampling, the line was manually flushed for 1 min. To reduce the risk of breath contamination, the sampling set up was attached to 3 m long Teflon tubes, and samples were always taken against air flow direction.

The unsaturated zone air was sampled from six boreholes of varying depths between 0.5 and 5 m (Table 1). Spatially, the boreholes cover a large portion of the cave's upstream hydrological catchment, and are overlain by contrasting vegetation cover (mixed-deciduous forest or a grass meadow) (Fig. 1) (Table 1). The gas was sampled in two lines from depths of 0.5 to 0.85 m (Shallow 1), ~~and~~ three lines from 0.6 to 1.5 m (Shallow 2), and ~~from deeper depths in single lines~~in single lines from a depth of 5 m (Deep 1, Deep 2, Deep 3, Deep 4). Due to the nature of the installation, it was not possible to assign a specific depth to the multi-line boreholes. All boreholes were drilled in 2013 and are equipped with aluminium tubes compacted by layers of gravel, bentonite and sand. The sampling line was flushed for 1 min once attached to the borehole, and then samples were taken into the Cali-5-Bond bags. Due to the nature of the borehole installation, we assume that the samples were not taken in steady state conditions, where the production rate of CO_2 would equal the sampling rate. ¶

ID	Well names	SISKA ID	Easting (CH1903+/LV95) (Swiss grid)	Northing (CH1903+/ LV95) (Swiss grid)	Depth (m)	Number of sampling lines	Classification	Ecosystem cover
SG-04	Shallow 1	CO2-13	2’567’083	1’256’904	0.5 to 0.85	2	Soil	Forest
SG-07	Shallow 2	CO2-10	2’567’074	1’257’068	0.6 to 1.5	3	Soil	Meadow
SG-05	Deep 1	EPI-2	2’567’097	1’256’896	5	1	~~Epikarst~~Unsaturated Zone	Forest
SG-10	Deep 2	EPI-4	2’567’089	1’256’890	5	1	~~Epikarst~~Unsaturated Zone	Forest
SG-08	Deep 3	EPI-7	2’567’080	1’257’063	5	1	~~Epikarst~~Unsaturated Zone	Meadow
SG-09	Deep 4	EPI-5	2’567’096	1’257’059	5	1	~~Epikarst~~Unsaturated Zone	Meadow

Table 1 Summary of the boreholes sampled in Milandre cave catchment ~~notating~~noting sample depth, number of sampling lines, classification in soil/ ~~epikarst~~unsaturated zone, and ecosystem cover type. The ID’s are the names given to the boreholes for this study, and are concurrent with the supplementary data provided. SISKA (Swiss Institute for Speleology and Karst Studies) IDs refer to the original names of the boreholes at the time of installation.

Cave air was sampled in two locations within Milandre cave proximal to both entrances, Downstream (topographically lower) and Upstream (topographically higher), with the same procedure as for the atmospheric samples (Fig. 1). To gain insight into possible spatial variability within the cave, a ~~cross-trip through~~through trip across the main passage of the cave was carried out in September 2021, and 14 samples were collected (Fig. 1). The trip was taken against the direction of ~~air-flow, from the downstream to upstream entrance, again to reduce risk of breath contamination~~airflow to reduce the risk of breath contamination, from the downstream to upstream entrance.

3.2 Continuous O_2 and CO_2 concentration monitoring

Soil gas O_2 and CO_2 concentrations were measured continuously nearby Shallow 2 at 40 cm depth and recorded at 10 min intervals between April 2023 and June 2024 using a SCD-41 CO_2 sensor (± 50 ppmV + 5 % of reading) (Sensirion, Switzerland) and SGX-40X O_2 sensor (Amphenol SGX, Sensortech, Switzerland). Calibration was cross-checked with an independent, handheld multi-gas monitor (XAM 5600, Dräger, Germany) before installation.

3.3 CO_2 concentration and $\delta^{13}C$ analysis

The concentration of CO_2 and the stable carbon isotopic composition ($\delta^{13}C$) in all gas samples was measured using a cavity ringdown spectrometer (CRDS) G2131-I Isotopic CO_2 instrument (Picarro, USA) at ETH Zurich (CO_2 concentration = 0.2 ppm, $\delta^{13}C$ = < 0.1 ‰ precision). Standard gases with known CO_2 concentrations, 399.6 ppmV and ~~2000~~2,000 ppmV CO_2 in synthetic air, were measured in addition to standard gases of known $\delta^{13}CO_2$ values, -27.8 ‰ and -2.8 ‰ VPDB, for offline calibration. As there was no equivalent standard gas available for ~~similarly~~ high CO_2 concentrations as in some samples, linearity of the concentration data produced by the CRDS is assumed. All standards and samples were measured by directly attaching the sample bags to the inlet of the CRDS that was previously fitted with a magnesium perchlorate dryer, and measuring gas concentration and isotopic composition for 2 min after reaching steady state. ~~For the evaluation, we~~We used the mean and standard deviation of this measurement interval for evaluation. $\delta^{13}C$ refers to the ratio between the two stable carbon isotopes with respect to the Vienna Pee Dee Belemnite (VPDB) standard:

$$\delta^{13}C\ (‰) = \left(\frac{\frac{^{13}C}{^{12}C}_{sample}}{\frac{^{13}C}{^{12}C}_{standard}} - 1 \right) \times 1000 \qquad (1)$$

3.4 Radiocarbon analysis

The CO_2 from each gas sample was converted into approximately 1 mg of graphite using an Automatic Graphitization Equipment (AGE, IonPlus, Switzerland) (Wacker et al., 2010a) coupled with a custom-made carbon inlet system. In this

process, each sampling bag was successively attached to the inlet system which dried the sample through a fine-grained magnesium perchlorate water trap via a vacuum line. The volume of air required to sample was calculated ~~depending on~~from the CO_2 concentration of the sample, ~~and~~allowing the appropriate amount ~~was~~of CO_2 to be trapped within a stainless-steel coil that was cooled by submersion in a liquid N_2 bath. After trapping, the CO_2 was sublimated by submerging the coil in a room temperature water bath and then adsorbed onto a zeolite trap using helium as a carrier gas between the coil and the trap. The CO_2 adsorbed onto the trap was then ~~thermically~~thermally desorbed and filled into the AGE reactor, where it was reduced to graphite with hydrogen over an iron catalyst (Wacker et al., 2010a). A modern standard of Oxalic Acid II gas ($F^{14}C$ = 1.3407, Oxa II, NIST SRM 4990C, HEKAL AMS Lab, Hungary) ~~as a modern standard~~ and a radiocarbon fossil reference CO_2 gas ($F^{14}C$ = 0, $CO_2 \geq 99.7$ % Vol.abs, Carbagas, Switzerland) were also graphitized and used to calibrate the measurements. The resulting graphite was pressed into targets for radiocarbon analysis through AMS analysis with a MIni CArbon DAting System (MICADAS, Ionplus, Switzerland) (Synal et al., 2007; Szidat, 2020). The resultant radiocarbon data were corrected using the BATS (4.3) software (Wacker et al., 2010b). In this study the ^{14}C content of samples will be discussed in $F^{14}C$ notation, which represents Fraction Modern (defined as the 1950 atmosphere) according to Reimer et al., (2004):

$$F^{14}C = \frac{\left(\frac{^{14}C}{^{12}C}\right)_{sample}}{\left(\frac{^{14}C}{^{12}C}\right)_{standard}} \qquad (2)$$

3.5 Dissolved inorganic carbon analysis

Drip water dissolved inorganic carbon (DIC) ^{14}C was measured to constrain the DIC degassing endmember. Samples were measured over one year from December 2021 and December 2022 at 9 drip sites focused on the actively dripping galleries nearby Upstream and Downstream (Fig. 1). Using a 5 mL syringe, 1 mL of drip water was collected directly from the soda straw stalactites on the cave roof to reduce fractionation effects associated with degassing. The water was injected directly into pre-cleaned Exetainer® (Round Bottom, Borosilicate, 938W, Labco Limited, UK) vials which had been flushed with helium gas and pre-spiked with 150 µL of 85 % H_3PO_4 (Suprapur®, 85 %, Merck KGaA, Germany). The ^{14}C content of the DIC was measured by sampling the vial headspace using the Carbonate Handling System (CHS, Ionplus, Switzerland) and transferring the gaseous sample to the AMS using a gas handling system. Here, the CO_2 was introduced to the gas ion source through the CHS at a flow of 50 mL min^{-1}. The ^{14}C content for each sample was measured for ~ 60 cycles. Standard material with a carbonate matrix of similar composition to the DIC samples were used as standards (IAEA C1 ($F^{14}C$ = 0) and C2 ($F^{14}C$ = 0.411), sodium bicarbonate ($NaHCO_3$, Sigma Aldrich, USA) and potassium bicarbonate ($KHCO_3$, Sigma Aldrich, USA) (both $F^{14}C$ = 0)).

3.6 Data analysis and statistics

All data and statistical analyses and all graphs were generated using the Python 3 programming language (Van Rossum & Drake, 2009).

Relationships between CO_2 concentration, $\delta^{13}C$, $F^{14}C$ for each sample type and the Mean Monthly Temperature (MMT) and Mean Monthly Precipitation (MMP) from Fahy weather station were explored using Spearman's rank correlation coefficient analysis (Kokoska & Zwillinger, 2000). A significantly correlated relationship between two variables is defined by $p < 0.05$, with the correlation coefficient denoted by "~~ρ~~rho", and number of samples involved in the analysis as "n".

4 Results

4.1 Atmospheric CO_2

The atmospheric samples had a ~~CO_2~~CO_2 concentration ranging from ~ 380 ppmV (August 2023) to ~ 485 ppmV (December 2022) with ~~an average~~a mean of ~ 440 ppmV. The $\delta^{13}C$ ranged from -12.5 ‰ (February 2023) to -7.6 ‰ (August 2023) and had a mean of -10.1 ‰ (n = 17). The ~~CO_2~~CO_2 sampled was typically modern, though had some fluctuation from $F^{14}C$ 0.98 (December 2022) to 1.02 (June 2022) and a mean of $F^{14}C$ 1.0 (Fig. 2).

¶

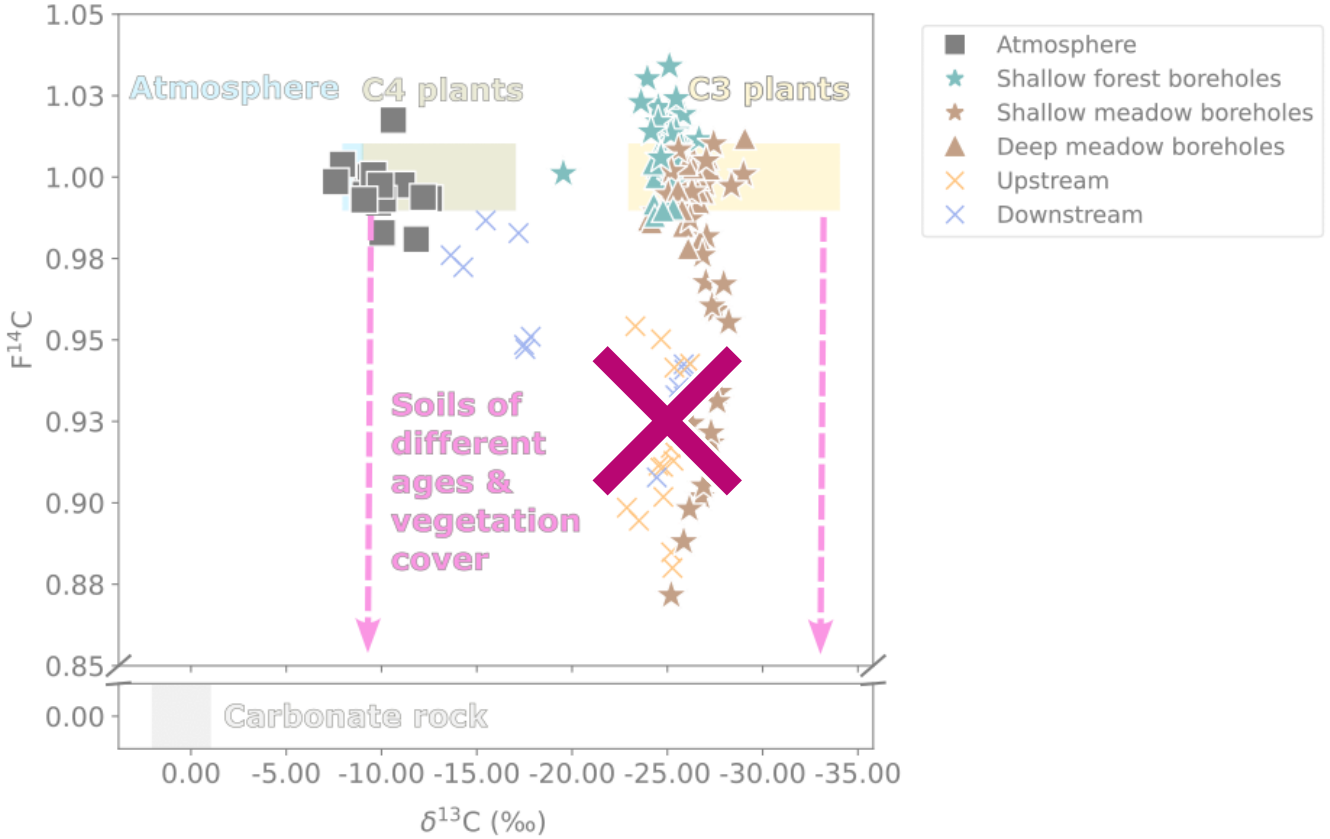
Atmosphere
C4 plants
C3 plants
Soils of different ages & vegetation cover
Carbonate rock
Atmosphere
Shallow forest boreholes
Shallow meadow boreholes
Deep meadow boreholes
Upstream
Downstream
F14C
δ13C (‰)
1.05
1.03
1.00
0.98
0.95
0.93
0.90
0.88
0.85
0.00
0.00
-5.00
-10.00
-15.00
-20.00
-25.00
-30.00
-35.00

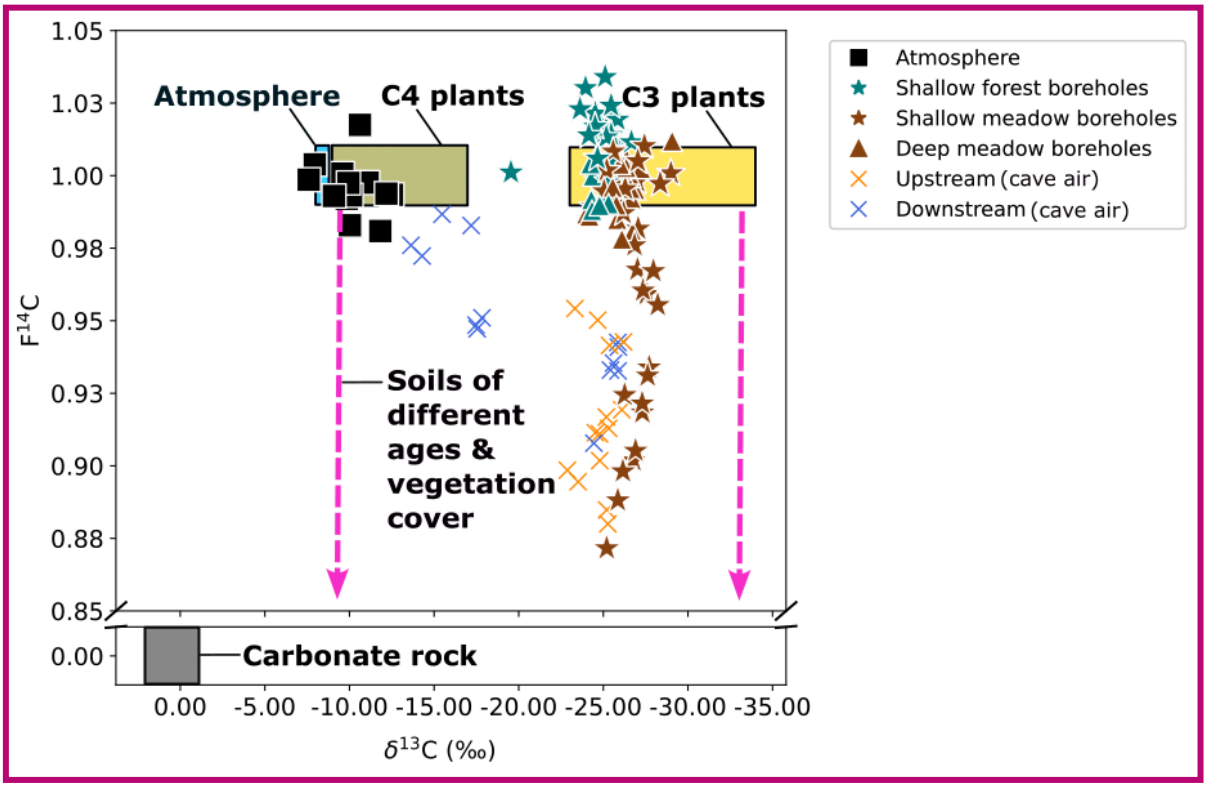

Figure 2. $\delta^{13}C$ and $F^{14}C$ of all gas samples over the monitoring period. The theoretical carbon reservoirs present in the system are shown with the atmosphere (blue), C3 plants (yellow), C4 plants (green), soils of various ages and compositions (pink arrows), and carbonate rock (grey).

¶

¶

¶

¶

4.2 Soil Zone CO_2

Soil boreholes have higher ~~CO_2~~CO_2 concentrations and lower $\delta^{13}C$ compared to the atmosphere (Fig. 2). Concentrations in boreholes that sample the soil zone (Shallow 1 and Shallow 2) (Fig. 3a) vary significantly depending on sampling depth, cover type, and season. The Shallow 1 boreholes (forest) show seasonal high ~~pCO_2~~pCO_2 in the summer months from June to October, which steadily declines during winter until it begins to rise again after April. ~~The Shallow 1 (forest) boreholes~~In these boreholes CO_2 concentrations vary from a maximum of ~ ~~18'000~~18,000 ppmV in August 2022 to a minimum in January 2024 of ~ ~~1200~~1,200 ppmV, with ~~an average~~a mean of ~~10'700~~10,700 ppmV (n = 21). The ~~Shallow meadow~~CO_2 concentrations in Shallow 2 (meadow) boreholes range from ~ ~~27'000~~27,000 ppmV in June 2023 to ~ ~~4800~~4,800 ppmV in February 2023 with ~~an average~~a mean of ~ ~~9900~~9,900 ppmV (n = 30).

The $\delta^{13}C$ varies by 7.0 ‰ in shallow forest boreholes over the sampling period ranging from a minimum of -26.7 ‰ in August 2023 to a maximum of -19.5 ‰ in January 2024 (Fig. 3b). There is ~ 4.0 ‰ isotopic variation in the shallow meadow boreholes with a minimum of -29.0 ‰ in October 2022 and a maximum of -24.4 ‰ in August 2022. The ~~pCO2~~ pCO_2 and $\delta^{13}C$ are negatively correlated in both shallow forest and shallow meadow boreholes (forest: ~~p~~rho = -0.47, p = 0.02, n = 25. meadow: ~~p~~rho = -0.49, p = 0.01, n = 30), and $\delta^{13}C$ is on average lower in shallow meadow than shallow forest boreholes.

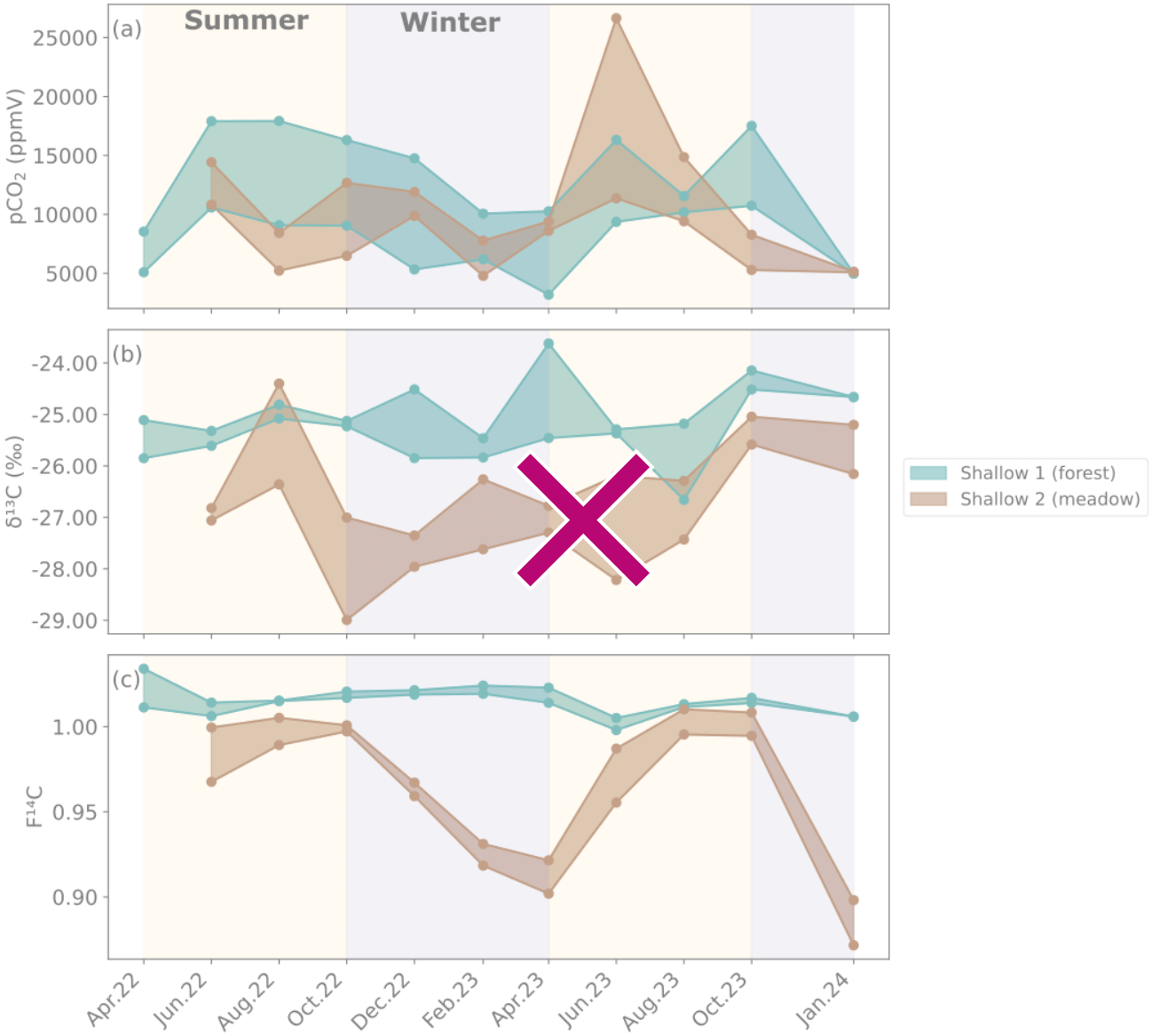
(a)
Summer
Winter
pCO2 (ppmV)
25000
20000
15000
10000
5000
(b)
δ13C (‰)
-24.00
-25.00
-26.00
-27.00
-28.00
-29.00
(c)
F14C
1.00
0.95
0.90
Apr.22
Jun.22
Aug.22
Oct.22
Dec.22
Feb.23
Apr.23
Jun.23
Aug.23
Oct.23
Jan.24
Shallow 1 (forest)
Shallow 2 (meadow)

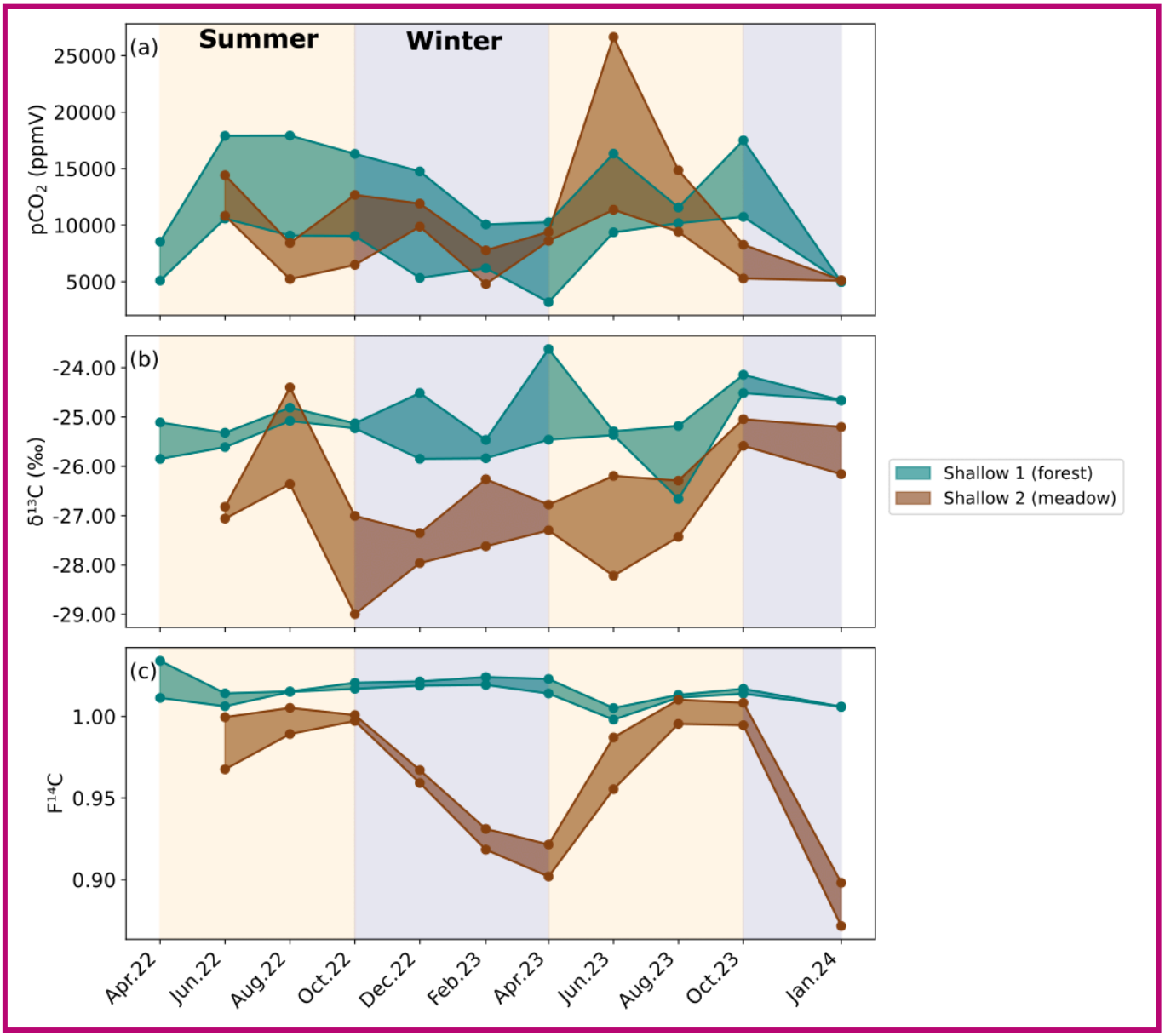

Figure 3. Maximum and minimum a) CO_2 concentration, b) $\delta^{13}C$ and c) $F^{14}C$ of the three soil borehole samples from Shallow 1 in the forest (green), and the two sampling lines in Shallow 2 in the meadow (brown). Summer (yellow) and winter (blue) seasons are highlighted by the coloured background. Concentrations are shown as ranges between maxima and minima as they aggregate over ~~several~~three sampling lines in the soil per location (Table 1).

$F^{14}C$ in Shallow 1 boreholes (forest) shows little annual variability and fluctuates slightly around a modern value (max = 1.03 in April 2022, min = 1.0 in June 2023) (Fig. 3c). Conversely, the shallow ~~meadow~~2 (meadow) boreholes show distinct

annual variation in $F^{14}C$, which steadily decreases from modern (1.0) in August 2022 and 2023 to a low in April 2023 and a minimum in January 2024 (0.87). The samples from the shallow forest boreholes have a positive correlation between $F^{14}C$ and $\delta^{13}C$ (~~p~~rho = 0.48, p = 0.02, n = 25). In the shallow meadow borehole samples, we observe a positive correlation between $F^{14}C$ and MMT (~~p~~rho = 0.67, p = 0.001, n = 30). All other tested parameters show no significant correlations (see Appendix A).

The continuously measured ~~O_2 and CO_2~~O_2 and CO_2 concentrations nearby Shallow 2 in the meadow show an inverse relationship (Fig. 4). The concentrations are relatively stable throughout most of the year with higher ~~O_2~~O_2 and lower ~~CO_2~~CO_2 concentrations. This pattern is disturbed by a sharp decrease in ~~O_2~~O_2 and an increase in ~~CO_2~~CO_2 observed around May/June of both 2023 and 2024. These different conditions last around one month before returning to the typical concentrations. The O_2 concentration ranges from a maximum of 20.2 % in August 2023 to a minimum of 17.8 % during a brief interval in May 2023. Conversely, the CO_2 concentration peaks at ~ ~~17'000~~17,000 ppmV in May 2023 and is the lowest at ~ ~~2500~~2,500 ppmV in August 2023. The Shallow 2 boreholes also show peaks in ~~CO_2~~CO_2 concentration in May to June 2023 (Fig. 4).

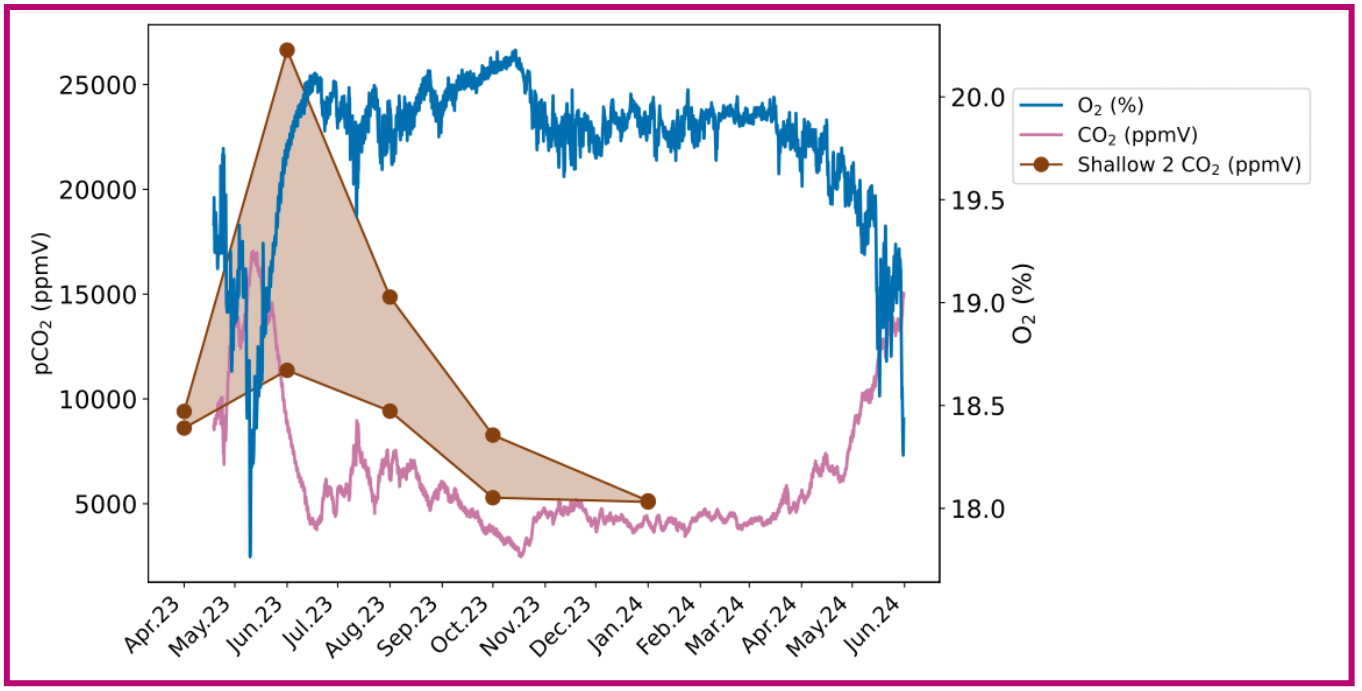

Figure 4. Continuously measured CO_2 (pink) and O_2 (blue) concentrations from the soil zone nearby the Shallow 2 boreholes. CO_2 concentrations from Shallow 2 are also plotted (brown).

4.3 ~~Epikarst CO_2~~¶

~~Epikarst CO_2~~**Unsaturated Zone CO_2**

Unsaturated zone CO_2 concentrations varied widely during the sampling period but ~~generally are~~are generally very high (>~~10'000~~10,000 ppmV). On average, the forest boreholes Deep 1 and Deep 2 have higher concentrations than the meadow boreholes Deep 3 and Deep 4. Concentrations are generally highest in the Deep 1 borehole (forest) (Fig. 5a) with a maximum of ~ ~~37'000~~37,000 ppmV in June 2023 and a similarly high concentration peak in June 2022. The lowest values (~ ~~21'000~~21,000 ppmV) at this borehole are recorded in the winter months. Deep 2 (forest) shows an opposite trend with its highest ~~CO_2~~CO_2 concentrations in autumn, winter, and spring (max = ~ ~~29'000~~29,000 ppmV in December 2022). The lowest ~~CO_2~~CO_2 concentrations were measured during the summer months (min = ~ ~~7900~~7,900 ppmV in June 2023). There is comparatively less variability in the Deep 3 and Deep 4 boreholes (both in the meadow). In Deep 3, concentrations fluctuate from ~ ~~6100~~6,100 to ~ ~~19'000~~19,000 ppmV with no obvious seasonality. Deep 4 has higher concentrations over the winter period and lower during summer, peaking at ~ ~~14'000~~14,000 ppmV in October 2022 and dropping to an overall minimum of ~ ~~3000~~3,000 ppmV in June 2023.

The $\delta^{13}C$ of the majority of ~~epikarst CO_2~~unsaturated zone CO_2 samples is very stable around ~ -26 ‰ (Fig. 5b). Similar to the shallow boreholes, samples from deep meadow boreholes (Deep 3 and 4) have on average slightly lower $\delta^{13}C$ values. In the meadow boreholes Deep 3 and Deep 4, the $\delta^{13}C$ and ~~pCO_2~~pCO_2 are negatively correlated (~~p~~rho = -0.66, p = 0.001, n = 21) (see Appendix A).

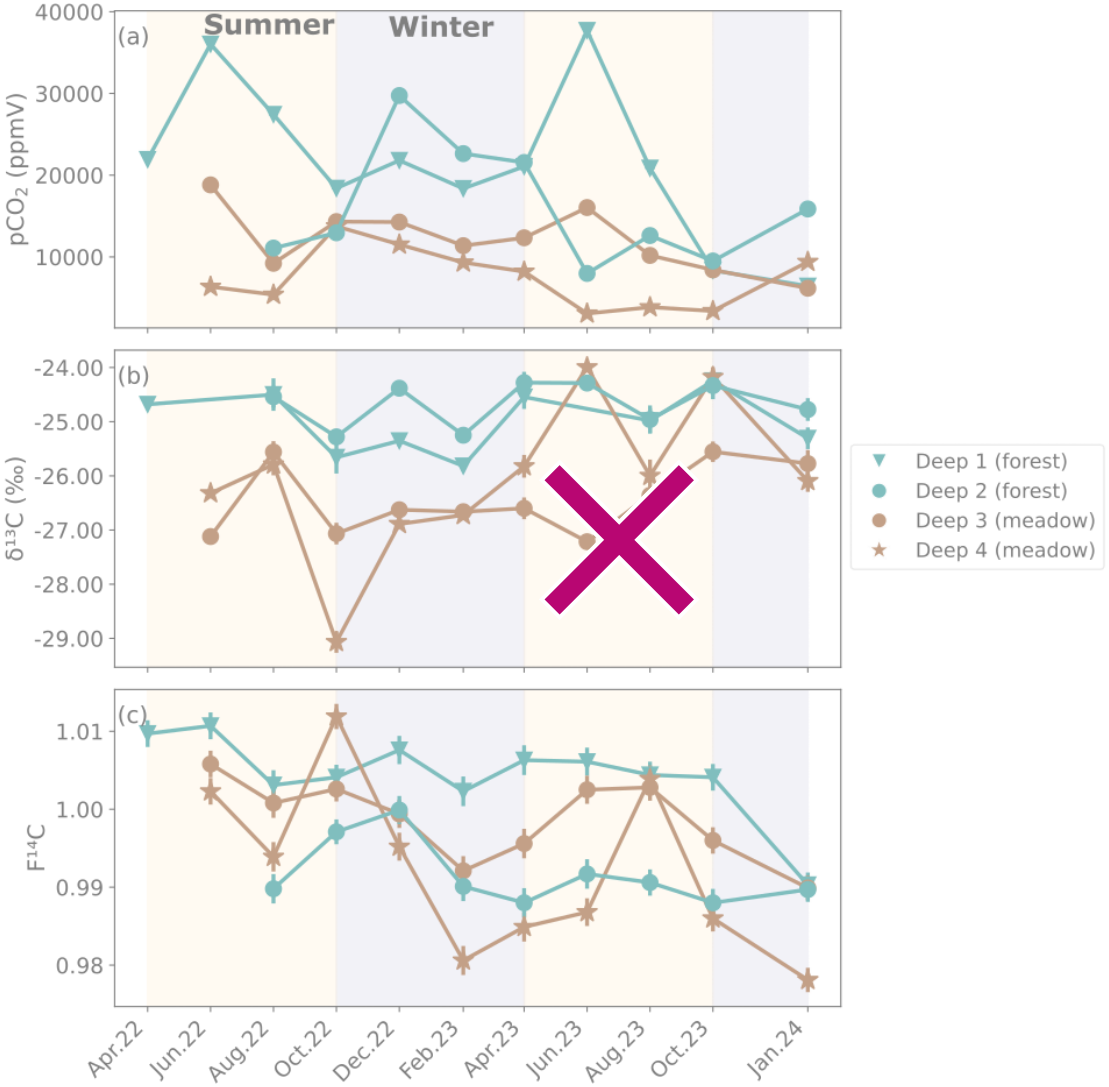
Summer
Winter
(a)
(b)
(c)
pCO2 (ppmV)
δ13C (‰)
F14C
Deep 1 (forest)
Deep 2 (forest)
Deep 3 (meadow)
Deep 4 (meadow)
Apr.22
Jun.22
Aug.22
Oct.22
Dec.22
Feb.23
Apr.23
Jun.23
Aug.23
Oct.23
Jan.24

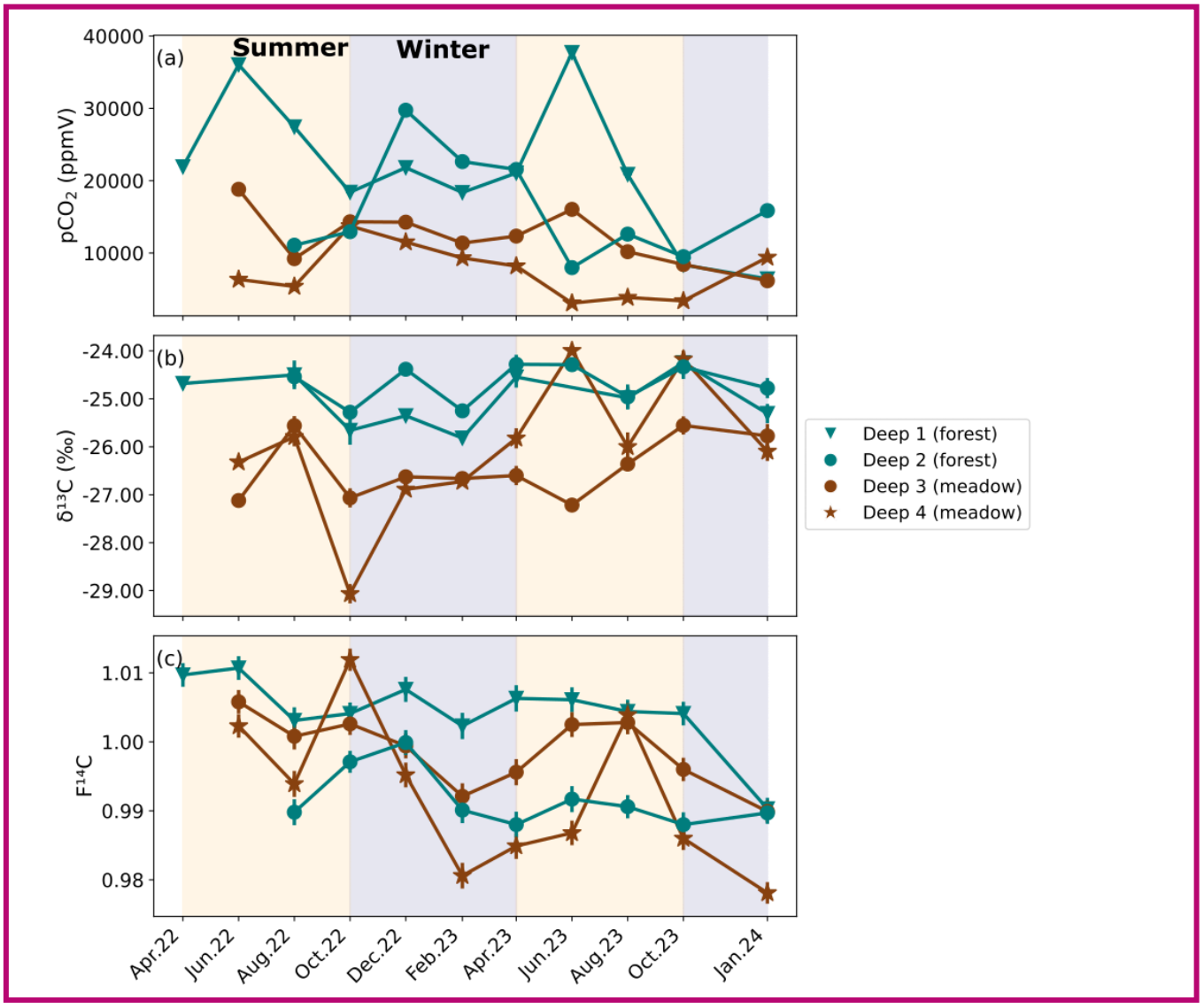

Figure 5. a) CO_2 concentration, b) $\delta^{13}C$ and c) $F^{14}C$ of ~~epikarst~~unsaturated zone borehole samples from forest boreholes Deep 1 and Deep 2 (green), and meadow boreholes Deep 3 and Deep 4 (brown). Summer (yellow) and winter (blue) seasons are highlighted by the coloured background.

The $F^{14}C$ of ~~epikarst CO_2~~unsaturated zone CO_2 samples is relatively stable throughout the sampling period, ranging from 1.01 (Deep 1, June 2022) to 0.98 (Deep 4, October 2022) (Fig. 5c). A possible seasonal pattern can be observed in the meadow boreholes (Deep 3 and Deep 4) with lower $F^{14}C$ values in the winter and spring months and higher $F^{14}C$ during summer, similar to the observation from the shallow meadow boreholes. No clear seasonal pattern is observed for Deep 1 and Deep 2. The $F^{14}C$ ~~epikarst~~ values of unsaturated zone CO_2 samples are negatively correlated with their $\delta^{13}C$ value (~~p~~rho = -0.54, p = 0.01, n = 21) and positively correlated with MMT (~~p~~rho = 0.53, p = 0.01, n = 21). All other tested parameters show no significant correlations.

4.4 Cave ~~CO_2~~¶

~~The CO_2~~CO_2

The CO_2 concentrations at the Downstream and Upstream sampling points in the cave are inversely correlated (Fig. 6a). Downstream shows ~~higher pCO_2~~a higher pCO_2 from June to October in 2022 and 2023, with a maximum of ~ ~~14'000~~14,000 ppmV in August 2023. The lowest concentrations are seen between December and April, reaching ~~close to~~near atmospheric concentrations with a minimum of ~ 420 ppmV in December 2021. Conversely, the highest ~~CO_2~~CO_2 concentrations at the Upstream site were measured during the winter months, with a maximum of ~ ~~30'000~~30,000 ppmV in December 2021. The lowest ~~CO_2~~CO_2 concentrations at Upstream were observed during the summer months with a minimum of ~ ~~2300~~2,300 ppmV in August 2022. Overall, concentrations at the Upstream site reach higher maxima and do not approach atmospheric values at their minimum, as at the Downstream site. The isotopic composition of CO_2 is inversely related to its concentration, with higher CO_2 ~~concentration~~concentrations coinciding with lower $F^{14}C$ and $\delta^{13}C$ values. Seasonal trends differ between sites, at the Downstream site $\delta^{13}C$ and $F^{14}C$ values are higher in winter and lower in summer, whereas at the Upstream site, $\delta^{13}C$ and $F^{14}C$ values show the opposite ~~patten~~pattern (Fig. 6b and c). The $\delta^{13}C$ in Downstream ranged between -25.9 ‰ in June 2023 and -13.6 ‰ in December 2021, and the $F^{14}C$ between 0.91 in October 2023 and 0.98 in February 2023. At Upstream, the opposite relation with ~~CO_2~~CO_2 concentration is well expressed for $F^{14}C$, but not as clear for $\delta^{13}C$, with minimal variability over the entire study period. The $\delta^{13}C$ in Upstream fluctuates slightly around a mean of -24.8 ‰.

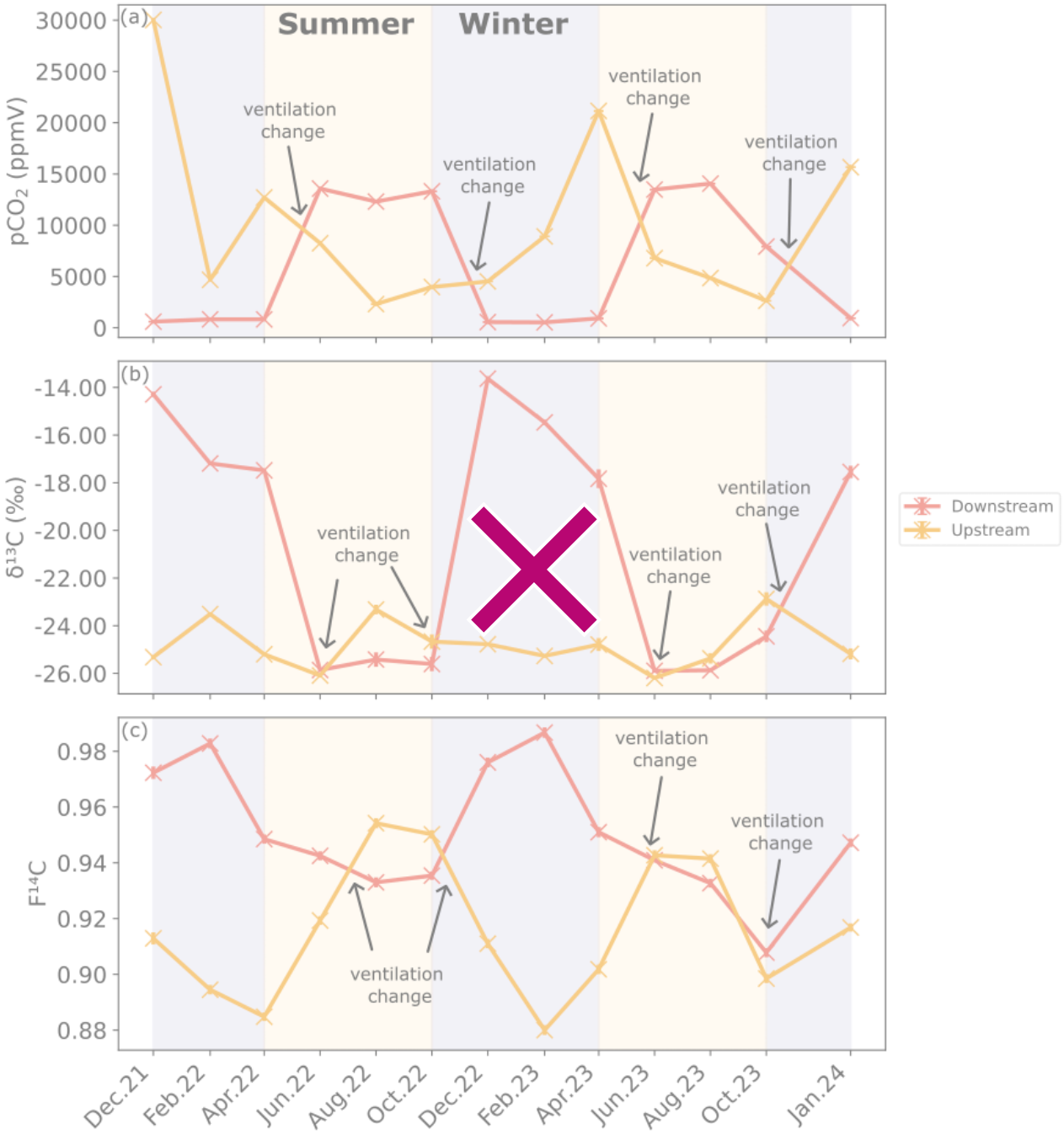
(a)
Summer
Winter
ventilation change
ventilation change
ventilation change
ventilation change
pCO2 (ppmV)
30000
25000
20000
15000
10000
5000
0
(b)
ventilation change
ventilation change
ventilation change
δ13C (‰)
-14.00
-16.00
-18.00
-20.00
-22.00
-24.00
-26.00
Downstream
Upstream
(c)
ventilation change
ventilation change
ventilation change
F14C
0.98
0.96
0.94
0.92
0.90
0.88
Dec.21
Feb.22
Apr.22
Jun.22
Aug.22
Oct.22
Dec.22
Feb.23
Apr.23
Jun.23
Aug.23
Oct.23
Jan.24

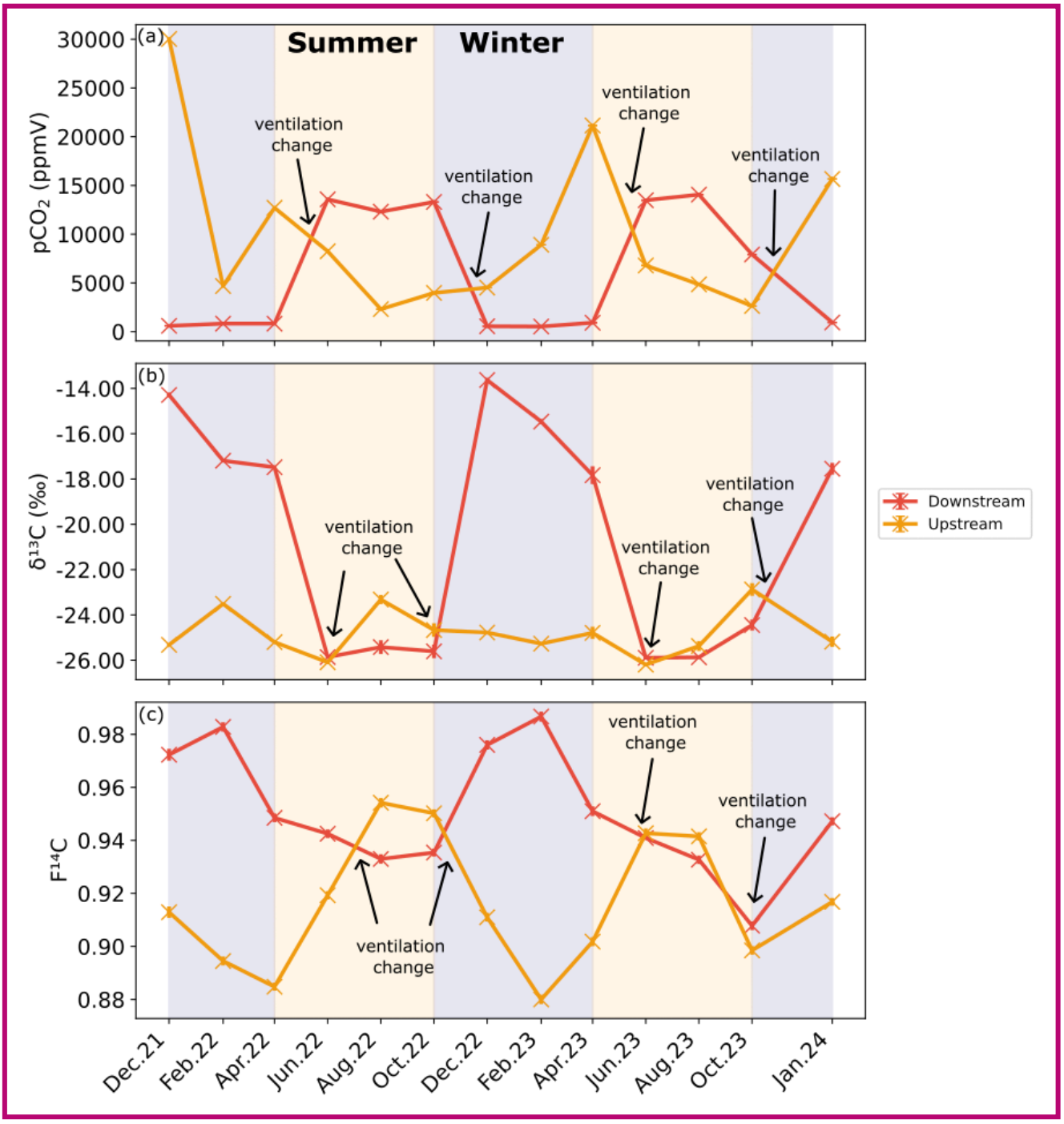

Figure 6. a) CO_2 concentration, b) $\delta^{13}C$ and c) $F^{14}C$ of cave air samples from the Downstream (red) and Upstream (orange) sites. Summer (yellow) and winter (blue) seasons are highlighted by the coloured background. The approximate timing of the temperature driven ventilation direction changes are shown by the annotations.

The $F^{14}C$ of ~~CO_2~~CO_2 in Upstream is overall lower than that of Downstream, increasing over late spring 2022 and into summer, peaking during August 2022 at 0.95. Decreasing $F^{14}C$ is observed during winter and into spring with lows of ~ 0.88 in February 2023. At the Downstream site, the ~~pCO_2~~pCO_2 and $\delta^{13}C$ (~~p~~rho = -0.9, p = 0.0001, n = 14), ~~pCO_2~~pCO_2 and $F^{14}C$ (~~p~~rho = -0.83, p = 0, n = 14), and $\delta^{13}C$ and MMT (~~p~~rho = -0.79, p = 0.0001, n = 14) are negatively correlated. Moreover, the ~~pCO_2~~pCO_2 and MMT (~~p~~rho = 0.53, p = 0.05, n = 14), and $\delta^{13}C$ and $F^{14}C$ (~~p~~rho = 0.74, p = 0, n = 14) are positively correlated. At the Upstream site, ~~pCO_2~~pCO_2 and MMP are positively correlated (~~p~~rho = 0.55, p = 0.04, n = 14), and ~~pCO_2~~pCO_2 and MMT are negatively correlated (~~p~~rho = -0.54, p = 0.05, n = 14) (See Appendix A). All other tested parameters show no significant correlations.

To constrain the isotopic composition of the end members contributing CO_2 to the cave air mixture, we use the Keeling plot approach (Fig. 7a & b). This approach assumes that cave air is a mixture of two main sources, the atmosphere (with known concentration and isotopic values), and a second source of a priori unknown composition. The y-intercepts of the Keeling plots represent the isotopic composition of the contributing end member which mixes with atmospheric air inside the cave (Keeling, 1961; Pataki et al., 2003) (Fig. 7a & b). We find that over time, the isotopic composition of the endmember varies for both $\delta^{13}C$ and $F^{14}C$ (Fig. 7c). The endmember $\delta^{13}C$ value varies ~~slightly~~ by ~ 2.0 ‰ from -26.8 ‰ in June 2023 to -25.0 ‰ in February 2022. The variation in the $F^{14}C$ is larger, ranging from 0.88 in February 2023 to 0.94 in June 2022, August 2022, October 2022, and June 2023 (ca. ~ 0.06 $F^{14}C$). Maxima in the $F^{14}C$ value derived for the endmember through the Keeling plot generally correspond to decreases in $\delta^{13}C$, with two $F^{14}C$ maxima occurring in June to October 2022 and in June to August 2023.

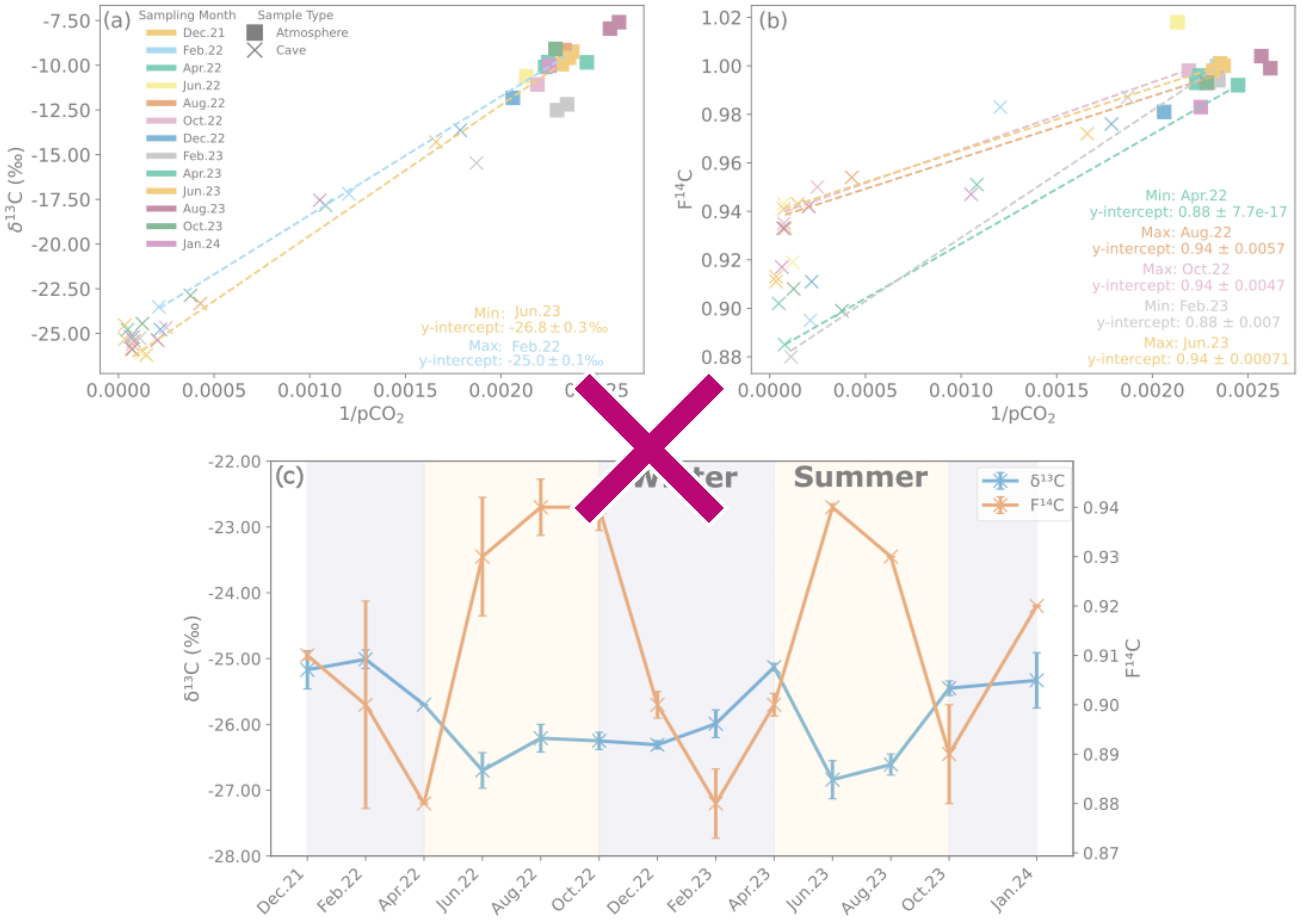
(a)
Sampling Month
Dec.21
Feb.22
Apr.22
Jun.22
Aug.22
Oct.22
Dec.22
Feb.23
Apr.23
Jun.23
Aug.23
Oct.23
Jan.24
Sample Type
Atmosphere
Cave
Min: Jun.23
y-intercept: -26.8 ± 0.3‰
Max: Feb.22
y-intercept: -25.0 ± 0.1‰
δ13C (‰)
1/pCO2
(b)
Min: Apr.22
y-intercept: 0.88 ± 7.7e-17
Max: Aug.22
y-intercept: 0.94 ± 0.0057
Max: Oct.22
y-intercept: 0.94 ± 0.0047
Min: Feb.23
y-intercept: 0.88 ± 0.007
Max: Jun.23
y-intercept: 0.94 ± 0.00071
F14C
1/pCO2
(c)
Summer
δ13C
F14C
δ13C (‰)
F14C
Dec.21
Feb.22
Apr.22
Jun.22
Aug.22
Oct.22
Dec.22
Feb.23
Apr.23
Jun.23
Aug.23
Oct.23
Jan.24

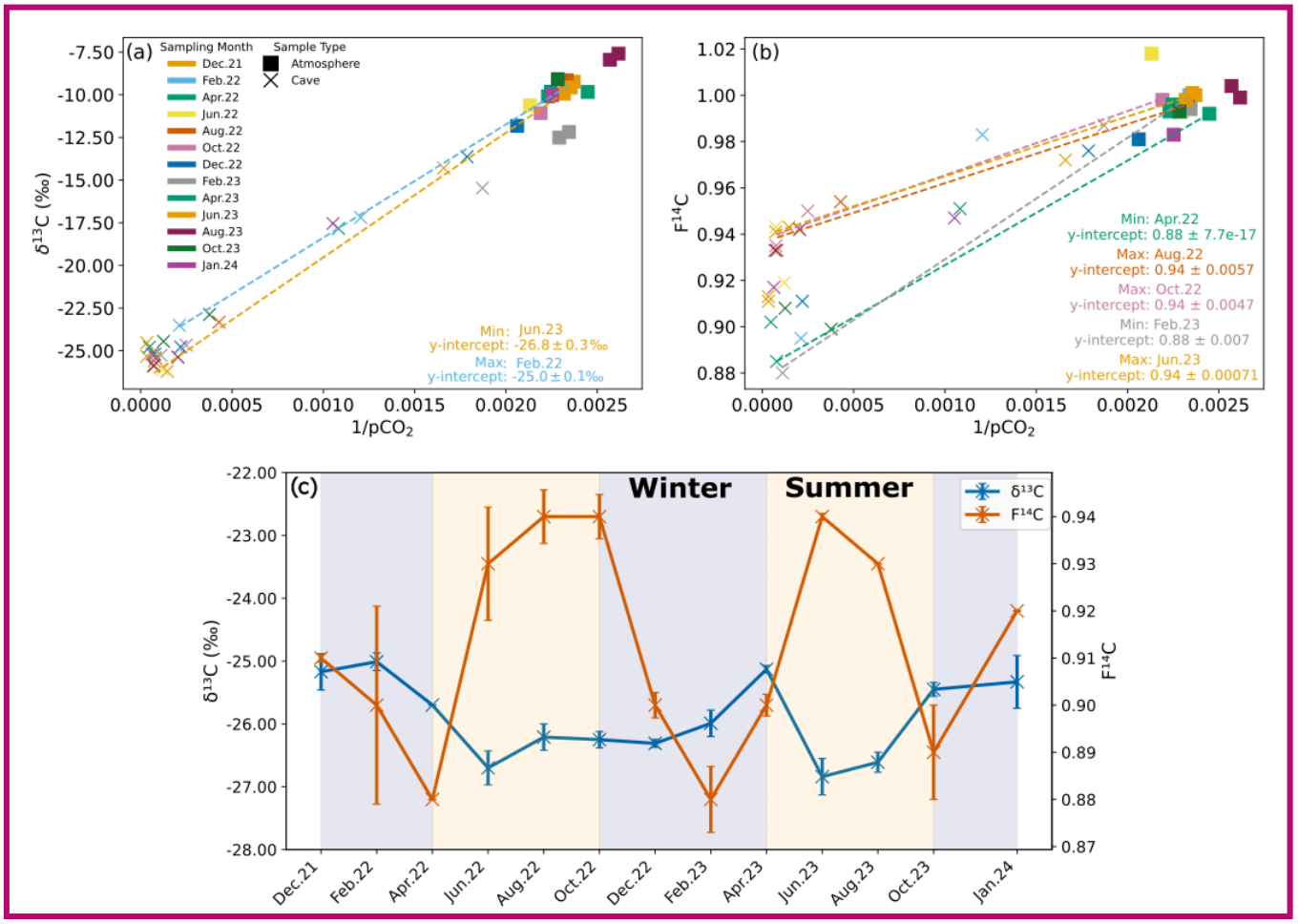

Figure 7. Keeling plots for $\delta^{13}C$ (a) and $F^{14}C$ (b) of cave (Upstream and Downstream sites) and atmospheric samples from all monitored months. The dashed regression lines denote the months with the maximum and minimum y-intercepts for $\delta^{13}C$ and $F^{14}C$. c) Keeling plot y-intercepts for $\delta^{13}C$ (blue) and $F^{14}C$ (orange) over time. Summer (yellow) and winter (blue) seasons are highlighted by the coloured background.

Samples taken along the main passage of the cave during the ~~cross-~~through trip show increasing pCO_2 from the lower entrance (location 1, corresponding to Downstream monitoring site, ~ ~~6900~~6,900 ppmV) to a plateau of ~ ~~14'000~~14,000 ppmV from sample point 4 to 9 towards the centre of the cave (Fig. 8a). The pCO_2 decreases sharply after sample point 9 until point 11 (~ ~~6600~~6,600 ppmV). The pCO_2 ~~then~~ increases briefly at sample point 12 and then decreases again upon approach to the cave exit (Upstream). The $\delta^{13}C$ values remain essentially constant at -25.5 ‰ through the initial segments of the cave, beginning to increase slightly past sample point 9 (Fig. 8b). The $\delta^{13}C$ value is -25.8 ‰ at sample point 9 and progressively increases as pCO_2 levels drop between sampling points 9 and 11, followed by a strong increase toward the Upstream exit (-11 ‰). The $F^{14}C$ values are constant at ~ 0.93 between sample points 1 and 5, followed by more variability

and generally lower $F^{14}C$ values in the middle of the transect, coinciding with the river passage of the cave (minimum 0.89 at sampling point 11; Fig. 9c). Towards the Upstream exit, $F^{14}C$ begins to increase strongly (maximum 0.98 at sampling point 15; Fig. 8c). Sample 13 is excluded due to a ruptured bag during sampling.

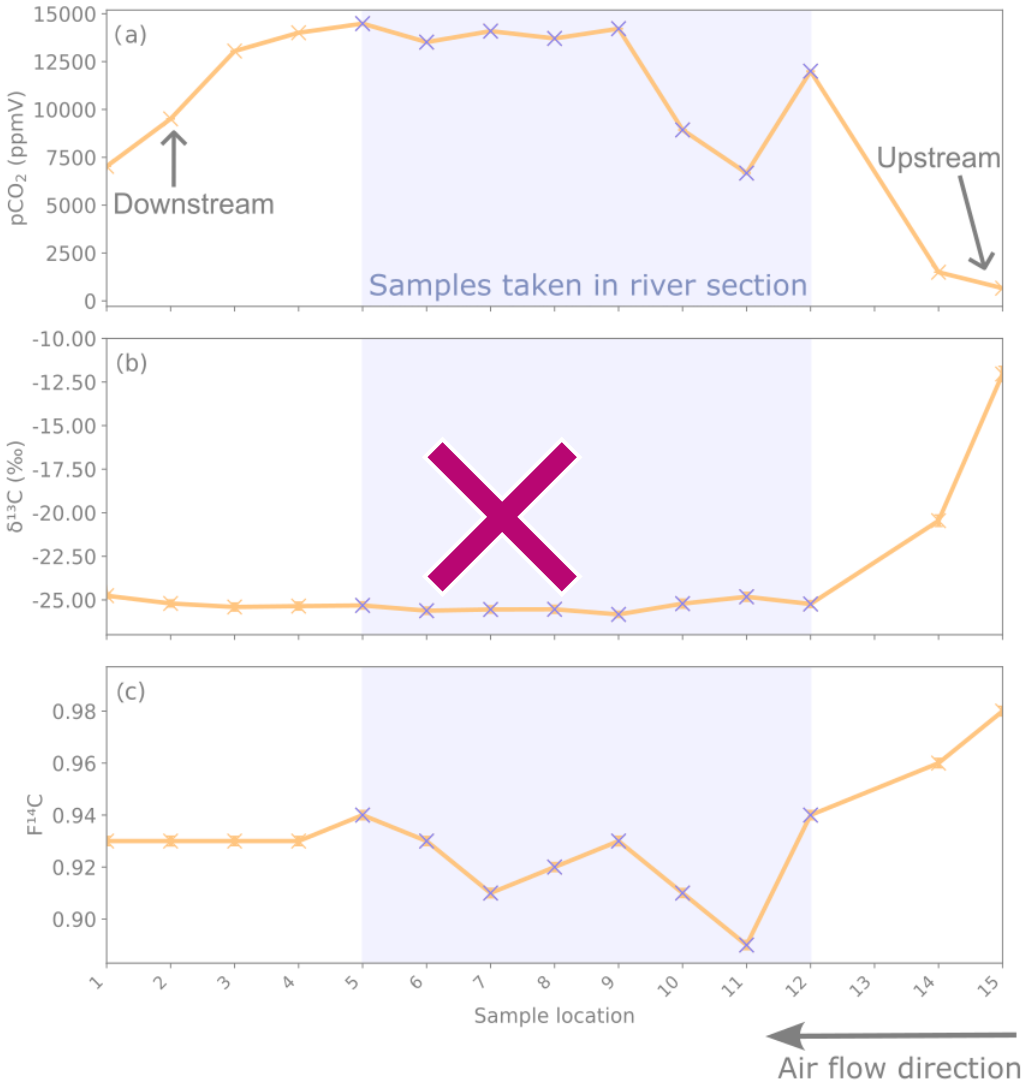
(a)
pCO2 (ppmV)
15000
12500
10000
7500
5000
2500
0
Downstream
Upstream
Samples taken in river section
(b)
δ13C (‰)
-10.00
-12.50
-15.00
-17.50
-20.00
-22.50
-25.00
(c)
F14C
0.98
0.96
0.94
0.92
0.90
1
2
3
4
5
6
7
8
9
10
11
12
13
14
15
Sample location
Air flow direction

379

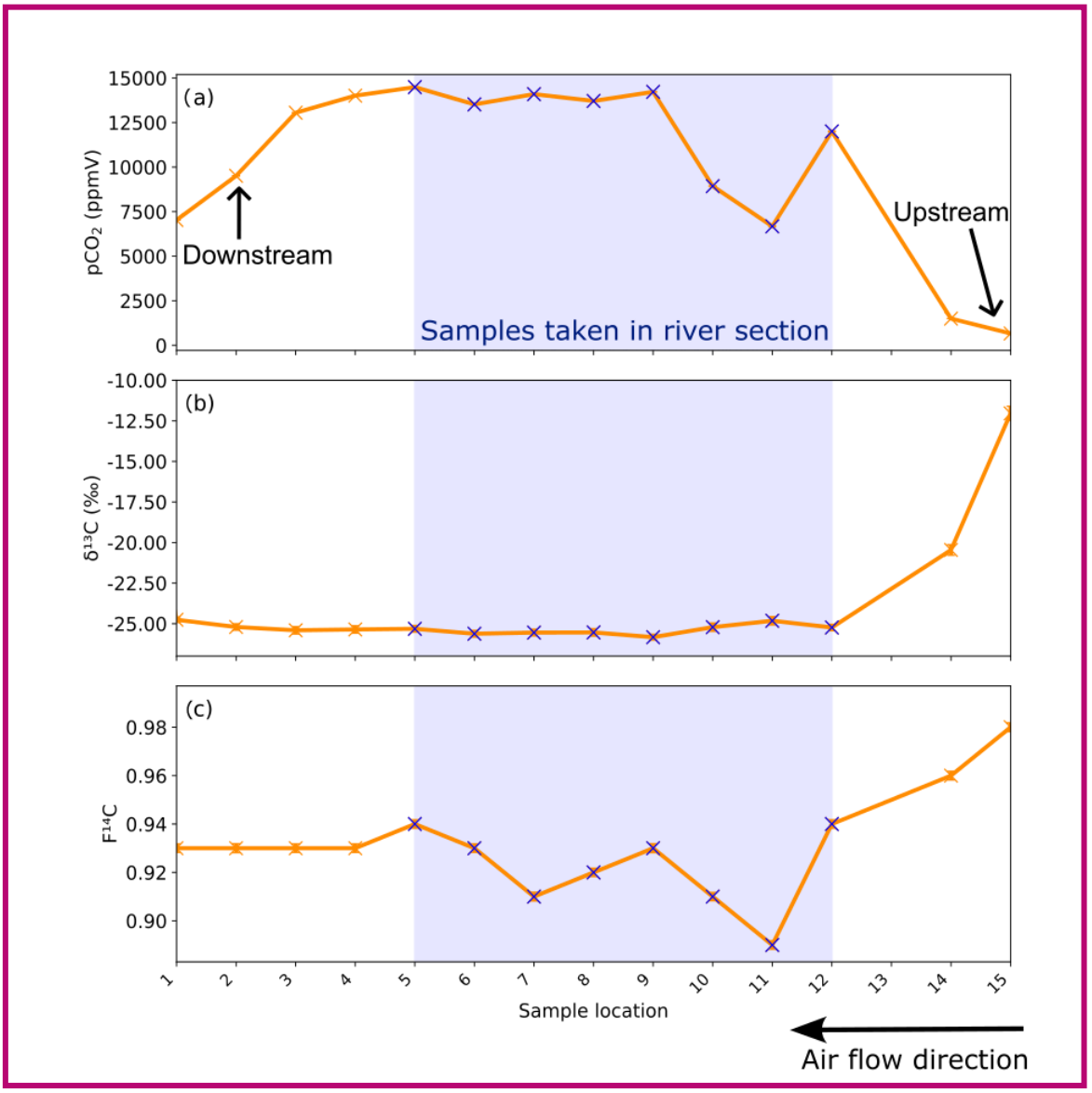

Figure 8. a) CO_2 concentration, b) $\delta^{13}C$ and c) $F^{14}C$ of cave air samples from the different sites sampled during the ~~cross~~through trip. Sampling locations are shown in Fig. 1. The blue crosses and blue bar notate where samples were taken standing in the river. The direction of cave air ventilation is shown by the lower arrow. The approximate locations of the Upstream and Downstream sampling sites are annotated.

5 Discussion

5.1 Sources and variability of shallow depth CO_2

The observed fluctuations in CO_2 concentrations in the Shallow ~~boreholes (0.5 to 1.5 m) varying~~borehole gas samples vary with depth, ~~vegetative~~vegetation cover, and season ~~suggest~~(Fig.3), suggesting complex carbon cycling dynamics taking place

in the soil zone and shallow fractured epikarst. Overall, both samples from forest and meadow locations have similar ~~average~~mean CO_2 concentrations. In the Shallow 1 forest boreholes, higher CO_2 concentrations occur during summer months (Fig. 3a), aligning with increased autotrophic (occurring in plant roots, leaves, and stems) and heterotrophic (microbial) respiration rates during warmer seasons~~ resulting~~. This results in higher CO_2 production compared to losses ~~due to~~from soil efflux to the atmosphere and downward transport in gaseous or dissolved form. Due to our discrete sampling approach, we cannot discern ~~between~~whether higher production ~~and increased losses. The decline in CO_2 concentrations during winter indicates reduced soil microbial respiration, and reduced autotrophic respiration, in response to lower temperatures.~~ or decreased losses are responsible for higher CO_2 concentrations. The decline in CO_2 concentrations during winter suggests that reduced autotrophic and soil microbial respiration in response to lower temperatures is likely an important driver of the seasonal cyclicity. The lower CO_2 concentrations during winter in the forest boreholes (Shallow 1) compared to the meadow boreholes (Shallow 2) could be an indication of frost effects. Soil frost induced by colder temperatures can reduce heterotrophic respiration in soils. Experiments inducing deep frost in forested soils by removing snow cover caused a greater decrease in heterotrophic respiration during winter months compared to snow covered control soils (Muhr et al., 2009). Furthermore, frost-heave can physically damage the extraradical hyphae on plant roots (Lekberg & Koide, 2008). Due to the shielding of the tree canopy, the forested areas in the Milandre catchment likely experience less snow cover compared to the open meadow where snow can accumulate freely. The meadow soils may experience reduced frost effects, meaning that heterotrophic respiration is not impacted to the same extent as the forest soils and can accumulate CO_2 year-round, as seen in borehole Shallow 2. However, during the monitored period, the Milandre catchment experienced little snow cover, suggesting that frost effects were likely minimal overall.

Though CO_2 production is reduced in winter, concentrations of several ~~~~1000~~1,000 ppmV are measured at our sites, perhaps due to~~ the ability of soil bacteria to survive in~~: i) slow, but persisting metabolic microbial activity at low temperatures (possible even below freezing temperatures as low as -5 to -7.5 ˚C (Kähkönen et al., 2001)), ~~to~~ii) reduced, but persisting autotrophic respiration of shallow roots, or iii) because of reduced transportation of CO_2 due to higher soil water content (Hashimoto & Komatsu, 2006). Similar seasonal trends in CO_2 concentrations have been ~~observed~~reported in ~~several~~ other studies (Billings et al; 1998; Pumpanen et al., 2003; Zhang et al., 2023). ~~Comparatively, CO_2 concentrations in the Shallow 2 meadow boreholes do not show as pronounced seasonality due to consistent CO_2 accumulation year-round.~~

The $\delta^{13}C$ values of CO_2 in shallow boreholes located in both the meadow and forest correspond to the typical isotopic signature of C3 plants which dominate the catchment area, supporting our interpretation of a dominant biogenic source of carbon in the soil gas (Fig. 2) (Fig. 3b). Plants using the C3 metabolic pathway (e.g. most temperate vegetation) produce carbon with a $\delta^{13}C$ of ~ -23 to -34 ‰ (Staddon et al., 2004). Furthermore, due to the nature of the sampling, the soil was not sampled in steady state conditions, potentially disturbing any existing CO_2 trends with depth. Another consideration is the symbiotic relationship between arbuscular mycorrhizal fungi (AMF) and plant roots which is ubiquitous globally, occurring

in 80 % of terrestrial plants (Fitter et al., 2000). AMF grows on plant roots and forms arbuscules within root cells, and hyphae which extend into the soil (Zhu & Miller, 2003). Plants benefit from this relationship because of the increased uptake of nutrients such as phosphorus and nitrogen, and improved resistance to environmental stress through more stable soil structure and enhanced water absorption (Kiers et al., 2011; Boyno et al., 2024). The fungi benefit through access to plant derived carbohydrates for energy, and a stable environment for growth and reproduction (Kiers et al., 2011). The respiration of AMF can contribute to the subsurface sequestration of carbon (Treseder & Allen, 2008), and may indeed contribute to the subsurface CO_2 which we measured at Milandre cave. There appears to be a temperature dependance of roots with AMF colonisation, where respiration rates increase at higher temperatures (Atkin et al., 2008). We observe an increase in CO_2 concentration during the higher temperature summer months (Fig. 3a, Fig. 5a), which may be caused in part by a contribution of CO_2 from enhanced respiration of AMF. The isotopic composition of the CO_2 produced by AMF respiration is not currently well constrained. Studies analysing the $\delta^{13}C$ of individual AMF spores showed that the $\delta^{13}C$ broadly corresponded to the C3 or C4 plant that it was associated with (Nakano et al., 1999). Therefore, it can be assumed that CO_2 produced by AMF respiration is similar to that of the C3 host plant dominated catchment of Milandre cave. As carbon is fixed from modern atmospheric CO_2 during host plant photosynthesis, the $F^{14}C$ signature should be modern (~1). Hence, the respiration of AMF may contribute to the modern CO_2 measured in the boreholes in both meadow and forest sites (Fig.3 & 5).

Though both meadow and forest boreholes have C3 plant $\delta^{13}C$ signatures, the $\delta^{13}C$ ~~of the~~ values of CO_2 in meadow soils are on average lower than those in the forest soils. Previous analysis of soil CO_2 from various karstic sites in Slovenia showed a similar trend, whereby the $\delta^{13}C$ values in meadow sites were ~1 ‰ lower compared to forested sites (Stickler et al., 1997). The meadow and forested areas at our site have developed contrasting soil compositions, with the meadow soils deeper, more compacted, and with a higher organic content~~, whilst~~ than the forest soils, which are shallow, unconsolidated, and with more roots. Comparisons of root free and root containing soils have suggested that root respiration contributes lower $\delta^{13}CO_2$ to the soil gas (Diao et al., 2022). This is the opposite trend to what our findings would suggest. Efforts to disentangle the $\delta^{13}C$ of autotrophic and heterotrophic contributions to soil CO_2 have shown a range of results, where autotrophic respiration can produce the same (Wu et al., 2017), higher (Moyes et al., 2010), or lower (Risk et al., 2012) $\delta^{13}C$ than heterotrophic respiration. However, different soil compositions can affect soil moisture, which can cause both increases (Unger et al., 2010), decreases (Powers et al., 2010), and no change (Diao et al., 2022) in soil $\delta^{13}C$. It is therefore difficult in the context of this study to determine the exact reason for the difference in $\delta^{13}C$ between surface covers. Interestingly, we also do not find evidence for contributions to subsurface gas from C4 plants, possibly due to the absence of sampling locations in the fields in the catchment where C4 crops are grown, suggesting limited lateral gas transport.

The CO_2 $F^{14}C$ of meadow boreholes in Shallow 2 shows statistically significant seasonal behaviour (ρrho = 0.67, $p = 0.001$, $n = 30$), with more aged CO_2 dominating the winter and spring months ($F^{14}C \sim 0.88$), and modern CO_2 in summer ($F^{14}C \sim$

1.00) (Fig. 3c). These seasonal shifts suggest a potential influence of temperature-sensitive processes on soil carbon dynamics, with higher autotrophic respiration rates ~~in the warm months, as well as~~and heterotrophic respiration of very recently fixed photosynthates dominating in the warm months (Campeau et al., 2019). Though typically the productive growing season for meadow grasses occurs in spring (Wingler & Hennessy, 2016), there is a lag in the ~~response in the~~ $F^{14}C$ response, which peaks between June and October. This may be due to the time it takes for enough modern CO_2 to accumulate in the soil and ~~dominating~~dominate the average gas age. Similar impacts of seasonality on the contributions of young carbon pools to the soil CO_2 budget have been observed in soils of various environments whereby autotrophic respiration and heterotrophic decomposition of younger carbon dominate in warmer months (Trumbore, 2000; Chiti et al., 2011; Vaughn & Torn, 2018). A contribution of fossil carbon from the dissolution of carbonate bedrock fragments in the soil zone could also be considered to explain the low soil CO_2 $F^{14}C$ values in winter. However, such a bedrock contribution would result in a concomitant increase in $\delta^{13}C$, as marine carbonates, which typically constitute the karstified host rock, are characterized by $\delta^{13}C$ of values of ~ 0 ‰ (Planavsky et al., 2015) and up to + 2 ‰ in the region of Milandre cave (Weissert & Mohr, 1996) (Fig. 2)~~, with~~. This would contribute a gaseous $\delta^{13}C$ ~ 9.54 ‰ lighter when at equilibrium with DIC from carbonate dissolution at 10.5 ˚C (Mook et al., 1974). Since we do not observe increases in $\delta^{13}C$ of soil gas during the periods of lower $F^{14}C$, this is an unlikely scenario. A further explanation for the seasonal variability could be due to the seasonal ventilation dynamics in the karst system, which promote ~~upwards ventilation~~upward movement of cave air during the winter, and downwards ~~ventilation~~movement of soil air in summer (see section 5.4).

The modern $F^{14}C$ CO_2 signature in the Shallow 1 forest ~~boreholes~~borehole (Fig. 3c) suggests a year-round dominant source of CO_2 from autotrophic root respiration and the decomposition of very recently fixed soil organic matter. As the root systems are deeper and more developed in the forest soils, there is a higher input of modern carbon compared to the meadows. The soils in the forested area are shallow (in some areas < 10 cm deep) and are dominated by large pebbles and fragments of the carbonate bedrock and shallow roots. Thus, shallow depth carbon sequestration may be suppressed in the forest soil, resulting in a CO_2 profile dominated by deeper root respiration (Hasenmueller et al., 2017; Tune et al., 2020).

5.2 Sources and variability of CO_2 at 5 m depth

CO_2 concentrations at 5 m depth vary considerably over the sampling period and between individual sites (Fig. 5a). CO_2 concentrations are generally higher in the forest boreholes (Deep 1, Deep 2) than in the meadow boreholes (Deep 3, Deep 4), likely due to the high volumes of CO_2 produced by autotrophic respiration of the mature woodland root system which penetrates deep into the ~~epikarst. The significant negative correlation between pCO_2 and MMT is highly influenced by borehole Deep 1, where very high CO_2 concentrations were measured in June 2022 and June 2023 (Fig. 5b)~~unsaturated zone. The CO_2 $\delta^{13}C$ values across all boreholes ~~reflects the isotopic value of~~reflect the C3 dominated ecosystem of the catchment, and ~~does~~do not indicate any ~~C4 plant input from~~input from C4 plants in the nearby fields. Notably, the ecosystem composition of the overlying vegetation (meadow vs. forest) influences the isotopic composition of CO_2 at 5 m in the same

way as the shallow boreholes, with a slightly lower $\delta^{13}C$ values in the meadow than the forest. The $F^{14}C$ values of ~~epikarst~~unsaturated zone CO_2 vary across all deep boreholes by ± 0.02 around a mean value of 1.00 (Fig. 5c), suggesting that ~~the $F^{14}C$ composition of CO_2 occurring in the shallower soil zone is from modern tree root CO_2 production~~across the catchment, autotrophic tree root respiration may be the dominant source of CO_2 at these depths (Breecker et al., 2012; Tune et al., 2020). Furthermore, the year-round modern CO_2 $F^{14}C$ values in the deeper meadow boreholes Deep 3 and Deep 4 compared to the seasonally pronounced signal in the shallower boreholes of Shallow 2~~.~~; highlights the potential influence of the meadow doline morphology. Boreholes Deep 3 and Deep 4 were drilled on the edge of the doline beneath shallow leptosols like those found in the forest, while Shallow 2 was drilled fully within the doline, where the soil is thicker and much richer in organic matter. Unfortunately, there is no ~~epikarst~~unsaturated zone depth borehole installed within the lower basin of the meadow to verify whether the seasonal signal measured at Shallow 2 translates to the deeper subsurface.

Whilst many studies point to the degradation of exported aged organic matter being the main source of karstic ground air (Breecker et al., 2012; Mattey et al., 2016; Bergel et al., 2017), ~~epikarst~~unsaturated zone borehole CO_2 in the Milandre cave catchment has predominantly modern $F^{14}C$ values, and does not show seasonal isotopic variability. This suggests that the majority of the CO_2 at 5 m depth is likely supplied by contemporaneous C3 tree root respiration. ~~This~~Similarly modern (106.4 pMC (percent modern carbon, corresponding to 1.064 in $F^{14}C$)) biologically sourced CO_2 was also detected in boreholes from Nerja cave, Spain (Vadillo et al., 2016) . Modern, but not substantially above modern $F^{14}C$ also excludes the contribution of substantial amounts of decadal-aged soil material containing bomb spike carbon due the enrichment in ^{14}C by thermonuclear weapons testing during 1950's and 1960's (Trumbore, 2000; Shi et al 2020). This result supports the body of literature stating that, in addition to the export and respiration of older carbon, large volumes of modern carbon are also transported into the unsaturated zone, likely in large part through deep root respiration (Breecker et al., 2012; Campeau et al., 2019; Tune et al., 2020). This suggests that deep roots, as found in mature forest ecosystems, might be more important than previously thought in contributing to the ground air budget.

5.3 Ventilation driven isotopic variation in cave air

The CO_2 dynamics in the cave show distinct variations in ~~concentrations~~concentration and isotopic ~~compositions~~composition between the two sampling points Upstream and Downstream (Fig. 6a, b, c). Cave ventilation dynamics modulate the mixing ratio between the atmosphere and the other contributing pools, and are usually the dominant source of variability (Kukuljan et al., 2021; Buzjak et al., 2024). Recent modelling of air flow dynamics in Milandre cave found that outside temperature controls 95 % of flow variability (Garagnon et al., 2022). During colder months when the outside temperature is ≤ 8 °C, the air in the cave flows topographically upwards from the northern downstream entrance close to the Downstream site, to the higher entrance closer to Upstream. When the temperature increases above 8 °C, the ventilation regime reverses. This seasonality is reflected in the alternating concentrations and isotopic composition of the CO_2 at the cave sampling sites as they experience varying amounts of dilution ~~from~~with atmospheric air during the year. CO_2 degassing ~~of~~from the cave river

at Upstream reduces the dilution effect in the upper passage. The effects of ventilation can also be observed in the higher spatial resolution sampling during the ~~cross~~through trip (Fig. 8a, b, c) whereby the summer regime ventilation resulted in lower concentrations, more positive $\delta^{13}C$, and increased $F^{14}C$ due to atmospheric mixing closer to the upper entrance (Upstream site). Spatially, a marked decrease in CO_2 concentration and $F^{14}C$ occurs at sampling ~~location~~locations 10 and 11 (~750 to ~~1000~~1,000 m~~)~~ from the cave entrance respectively~~;~~) though little change is observed in the $\delta^{13}C$. This air input could be associated with an older organic matter pool which, however, contributes only little to the entire CO_2 mass flux.

5.4 Sources and variability of CO_2 in cave air

The Keeling plot y-intercepts show that the composition of the gas pool (karst endmember) that mixes with atmospheric air in the cave ~~changes~~ varies seasonally (Fig. 7c). It is important to note that, while the isotopic composition of cave CO_2 is influenced by ventilation-driven dynamics, the Keeling plot y-intercept represents the composition of the subsurface gas that mixes with the atmospheric air during ventilation and is not affected by it. The $\delta^{13}C$ of the karst endmember is mostly stable, varying ~~-26 ‰, ± 2~~± 2 ‰ around a mean value of -26 ‰, a value typically associated with the CO_2 produced by the C3 plants which dominate the catchment ecosystem. This value is also very similar to the $\delta^{13}C$ CO_2 values of soil and ~~epikarst~~unsaturated zone gas and reinforces the notion of ~~a common source. Previous work~~the karst endmember being dominated by ecosystem respiration . Previous work at Milandre cave investigating aquifer dynamics using ^{222}Rn ~~at Milandre~~ suggested that the majority of the cave CO_2 comes from the overlying soils (Savoy et al., 2011). The $F^{14}C$ of the Keeling plot y-intercept, on the other hand, shows seasonal variability with distinctly more "modern" (closer to $F^{14}C = 1$) during the summer and "aged" ($F^{14}C < 1$) CO_2 during the winter. The transition from an $F^{14}C$ of 0.94 to 0.88 represents a change in the mean apparent age of CO_2 from ~ 100 to 1000 ~~yrs~~years, well beyond the assumed residence time of water in the ~~epikarst~~unsaturated zone of ~ 5.5 to 6.6 years (Affolter et al., 2020).

Several mechanisms may be responsible for the seasonal $F^{14}C$ fluctuations of the karst endmember. A contribution of carbon from the oxidation of methane, either from methanotrophs or through the evolution of pore fluid waters, must be considered. Methane can be produced by both thermogenic (originating from ancient organic rich sediments) and biogenic (particularly through methanotrophic bacteria) processes (Suess & Whiticar, 1988). The $\delta^{13}C$ CO_2 range of published values for the CO_2 resulting from methane oxidation from both sources is broad, with biogenic spanning from ~ - 20 to -90 ‰, and thermogenic from ~ -30 to -65 ‰ (Suess & Whiticar, 1988). The $\delta^{13}C$ CO_2 produced by thermogenic sources can also evolve to less negative values of ~ - 25 to - 34 ‰ in settings where there is near total conversion of CH_4 to CO_2 (Shoell, 1980; Frieling et al., 2016). Methane that undergoes biogenic oxidation is typically sourced from the atmosphere, meaning the resulting CO_2 will have a modern $F^{14}C$ signature ($F^{14}C \sim 1$). In contrast, CO_2 produced by thermogenic methane oxidation will have a fossil $F^{14}C$ signature, because the methane originates from ancient organic rich sediments that contain no measurable radiocarbon ($F^{14}C \sim 0$). While measuring methane concentrations quantitatively was not possible with our analytical setup, qualitative data shows that methane concentrations in Milandre cave air and catchment borehole samples were exceedingly low (~ 90 to

970 ppb), suggesting methane oxidation may occur in the Milandre subsurface environment. Methanotrophic bacteria have been identified in 98 % of soils sampled from 21 North American caves at a mean bacterial abundance of 0.88 % (Webster et al., 2022). Methanotrophic bacteria in caves significantly contribute to methane consumption, with a study in Pindal Cave (NW Spain) showing how methanotrophic bacteria associated with moonmilk deposits remove 65 % to 90 % of atmospheric methane entering the cave (Martin-Pozas et al., 2022). As our cave and borehole CO_2 samples have a $\delta^{13}C$ of ~ -26 ‰ and a variable $F^{14}C$ in the cave air and shallow meadow samples, we cannot rule out a contribution of methane oxidation from biogenic processes actively occurring in Milandre. However, this would not explain the depleted radiocarbon signature that we measured episodically in the cave air. Methane evolved abiogenically from pore fluids in Oxfordian marls may have an isotopic ratio similar to that measured in our samples if thermogenically derived with a dominant conversion of CH_4 to CO_2. However, it is unlikely that this process occurred in the Milandre cave sediments given the lack of organic rich sedimentary rocks in the stratigraphy. Thus, while we cannot quantify the importance of methane oxidation on the subsurface carbon budget at our site, it is unlikely that methane oxidation processes are responsible for the variation in radiocarbon ages in cave air CO_2.

Despite the apparent limiting factors for microbial growth in caves, it is known that different organisms are able to thrive within this niche including bacteria, archaea, algae, and fungi. In terms of bacteria, Proteobacteria is typically reported as the dominant group in caves (Zhou et al., 2007; Tomczyk-Żak & Zielenkiewicz, 2016). However, in some cases Actinobacteria is the largest group of microbes (Wiseschart et al., 2018). In two Chinese caves with high CO_2 concentrations (> 3,000 ppm), Proteobacteria, Actinobacteria, Bacteroidetes, and Thaumarchaeota were the dominant phyla (Chen et al., 2023). Hundreds of fungi taxa have been described in caves globally, with Ascomycota being the most commonly reported (Gherman et al., 2014). Though not yet thoroughly investigated, diverse communities of protists have also been identified within caves (Gogoleva et al., 2024), as well as archaea (Biagioli et al., 2023), and algae (Kosznik- Kwaśnicka et al., 2022). As biological processes generally favour the incorporation of lighter ^{12}C compared to ^{13}C, the respiration of these organisms would contribute an organic signature (lower $\delta^{13}C$ and a $F^{14}C$ corresponding to the age of the carbon source being consumed, which can range from modern to more aged $F^{14}C$) to the CO_2 composition of cave air at Milandre cave. With the isotopic analysis used in this study, and because we did not analyse the microbial community diversity present in Milandre cave and its catchment, the CO_2 contributions from different types of microbial processes cannot be distinguished from one another. We are only able to distinguish between "organic" processes (in-cave microbial, soil, root, and fungi respiration) which produce a CO_2 with a lower $\delta^{13}C$ signature and a range of $F^{14}C$ depending on the age of the organic material consumed, and "inorganic" processes (carbonate degassing and atmospheric ventilation) which contribute CO_2 with a higher $\delta^{13}C$ and a range of $F^{14}C$.

Varying contributions of host rock-derived carbon to cave air through shifts in the host rock dissolution regime ~~could~~ can affect the isotopic composition of cave air. Dissolution of the host rock carbonate can occur under a wide range of conditions

between two extreme cases: ~~in~~completely closed and completely open systems. In a completely closed system, the aqueous solution becomes isolated from the soil CO_2 reservoir after passing into the ~~epikarst~~unsaturated zone resulting in a theoretical 50:50 contribution ratio of carbon ions in solution from the carbonate host rock and from soil air, and overall decreasing $F^{14}C$ to as low as 0.5 (Fohlmeister et al., 2011; Milanolo & Gabrovšek, 2015). On the other hand, in a completely open system the aqueous solution can continuously exchange with an unlimited soil CO_2 reservoir resulting in most carbon atoms sourced from the soil CO_2 reservoir, and the rock contribution being minimal (Fohlmeister et al., 2011). Most natural systems exist in an intermediate state between ~~fully~~completely open and ~~fully~~completely closed settings.

If the seasonal variability in CO_2 $F^{14}C$ in Milandre cave reflected seasonal shifts in the "openness" of the system, summers (with higher $F^{14}C$) would be characterised by a more open system with higher rates of exchange between the aqueous solution and the soil CO_2 reservoir. The observed shift to lower $F^{14}C$ in winter would reflect a more closed system with a higher contribution of the $F^{14}C$ free carbonate bedrock. Shifts in the open-closed continuum would likely result in changes in the $\delta^{13}C$ of the endmember (Fairchild & Baker, 2012) which is not seen in the cave air, with an expected lower $\delta^{13}C$ in a more open system, and an increase in a more closed system because of the higher ~~solid~~carbonate host rock carbon contribution ($\delta^{13}C \approx 0$ ‰). However, varying amounts of isotopic fractionation can occur when CO_2 is degassed from the drip water DIC pool into the cave atmosphere, potentially influencing the isotopic composition of the measured cave air CO_2 (Mickler et al., 2019).

We constructed a mixing model which allows us to evaluate how much variability in the Keeling plot y-intercept (i.e. the second source of carbon to cave air besides the atmosphere) can be explained by variation in DIC contribution from dissolution regime changes and degassing fractionation. This model assumes that the Keeling plot y-intercept is itself a mixture of two endmembers that contribute CO_2 to cave air, the modern soil ($F^{14}C_{soil} = 1$), and the DIC ($F^{14}C_{DIC}$), where the $F^{14}C_{DIC}$ ~~itself~~ represents a mixture of dissolved soil CO_2 and DIC from carbonate mineral dissolution ~~that is degassed into the cave air~~, which we can constrain with our measured DIC values. The ~~$F^{14}C$ soil~~$F^{14}C_{soil}$ represents direct input of CO_2 soil gas into the cave.

The mixing ratio between $F^{14}C_{soil}$ and $F^{14}C_{DIC}$ results in the $F^{14}C$ of CO_2 ~~entering the cave atmosphere~~of the karst endmember ($F^{14}C_{cave}$). Thus, the cave air CO_2 $F^{14}C$ can be expressed as (where f is fraction, defined as between 0 and 1):

$$F^{14}C_{cave} = f_{soil}F^{14}C_{soil} + f_{DIC}F^{14}C_{DIC} \qquad (3)$$

~~Solve for~~ Since f_{soil} ~~and~~ f_{DIC}, ~~where~~ $f_{DIC} = 1 - f_{soil}$:

$$F^{14}C_{cave} = f_{soil}F^{14}C_{soil} + (1 - f_{soil})F^{14}C_{DIC} \qquad (4)$$

For $F^{14}C$, fractionation is generally negligible during carbonate dissolution and degassing compared to $\delta^{13}C$, due to ~~measurement precision~~ unit conversion i.e. % vs ‰ (Fohlmeister et al., 2011). We use the mixing calculation (Eq. 4) to estimate the contributions of f_{soil} and f_{DIC} using the highest (0.94), an intermediate (0.90), and the lowest (0.88) measured cave CO_2 $F^{14}C$ values ($F^{14}C_{cave}$), and $F^{14}C$ DIC ($F^{14}C_{DIC}$) based on the highest (0.98) intermediate (0.88) and lowest (0.78) measured values of drip water DIC. We find that when $F^{14}C_{DIC} = 0.98$, the mixing model results in impossible scenarios with $f_{soil} > 1$ and $f_{DIC} < 0$ because this value is higher than the highest $F^{14}C_{cave}$, ~~and~~. When $F^{14}C_{DIC} = 0.88$ it results in a highly unlikely scenario based on our observations and the literature where $f_{soil} = 0$ and $f_{DIC} = 1$ ~~when $F^{14}C_{DIC} = 0.88$~~, as this corresponds to the lowest $F^{14}C_{cave}$ value (Fig. 9a). Only the scenario with lowest $F^{14}C_{DIC} = 0.78$ produced realistic mixing fractions. Overall, this implies that there is a discrepancy between the measured $F^{14}C_{DIC}$ and what is derived by a simplified mixing model based on the $F^{14}C$ of cave CO_2, with $F^{14}C_{DIC}$ values too high to result in the $F^{14}C_{cave}$ composition that we observe. Thus, carbonate dissolution and subsequent degassing of CO_2 from drip water DIC to cave air is unlikely to be the dominant process explaining the shifts in cave air $F^{14}C$ over time.

~~The $F^{14}C_{DIC}$ is based on the analysis of 9 drip water sites of varying drip rates and ecosystem coverage. It is possible that the sampling set up did not capture the true range of $F^{14}C_{DIC}$ in the drip water, though rather unlikely due to the diversity in drip rate and hydrological response of drips measured. ¶~~

As our mixing ratios derived from measured DIC values ~~are~~were mostly not ~~possible~~realistic according to the two endmember mixing scenario, we ~~then explored~~considered how a wider theoretical range of $F^{14}C_{DIC}$ values (from closed to mainly open system dissolution conditions, 0.50 to 0.90 $F^{14}C$) would affect the contributing fractions of f_{soil} and f_{DIC}. Variations in $F^{14}C_{DIC}$: 0.50 to 0.85 result in viable mixing fractions across the range of $F^{14}C_{cave}$, with the f_{soil} (20 to 76 %) and f_{DIC} (24 to 80 %) differing widely (Fig. 9b).

As the ~~average~~mean value of cave CO_2 $\delta^{13}C$ is -26 ‰ (we take a range from -25 to -27 ‰), we created a similar two-endmember mixing calculation for $\delta^{13}C$ values to test whether the mixing ratios derived from $F^{14}C$ translate to observed $\delta^{13}C$ values. For this we used the ~~average~~mean $\delta^{13}C$ of soil CO_2 ($\delta^{13}C_{soil}$) = -26 ‰, and the $\delta^{13}C$ of the DIC ($\delta^{13}C_{DIC}$) = -15 ‰ (estimated from ~~an average~~a mean of the $\delta^{13}C$ produced during the $F^{14}C$ DIC AMS measurement (see Appendix B)).

Fractionation effects during degassing must be considered when modelling $\delta^{13}C$. If equilibrium fractionation between DIC and $CO_{2(g)}$ occurs, the fractionation factor ($\Delta^{13}C_{HCO3-CO2,eq}$) at 10.5 ˚C between HCO_3- and CO_2 is 9.54 ‰, with the gas being 9.54 ‰ depleted in ^{13}C relative to the fluid (Mook et al., 1974). Kinetic fractionation can occur during rapid degassing of CO_2 as well as during rapid precipitation of carbonate minerals (Mickler et al., 2019). If kinetic fractionation occurs during degassing, this results in a greater depletion of the dissolved CO_2 in ^{13}C compared to equilibrium fractionation (i.e. a more positive $\delta^{13}C_{DIC}$). The possible ranges reported for the composition of CO_2 generated from kinetic fractionation during degassing in caves vary widely, with some reporting $\Delta^{13}C_{HCO3-CO2,kin}$ close to that resulting from equilibrium fractionation (Dulinski & Rozanski~~ et al.~~, 1990), and others a range of 10~~-~~ to 65 ‰ (Mickler et al., 2019). The extent of kinetic fractionation is expected to depend on the amount of degassing that occurs, which is a function of the disequilibrium between the fluid and the surrounding air (Frisia et al., 2011). In our system with limited geochemical data regarding fluid compositions, it is difficult to determine what extent of kinetic fractionation may have occurred. Hence, we first assume that the fractionation is < -9.54 ‰ (i.e., greater compared to equilibrium conditions) and take a moderate but arbitrary value ballpark of $\Delta^{13}C_{HCO3-CO2,kin}$ = 30 ‰.

A mixing calculation is then applied to assess if the measured range of the karst endmember $\delta^{13}CO_2$ given by the Keeling plot can be consistent with the extended range of $F^{14}C_{DIC}$ (0.50 to 0.85 $F^{14}C$) and measured $F^{14}C_{cave}$ under conditions with equilibrium degassing and kinetic degassing:

Equilibrium degassing:

$$\delta^{13}C_{cave} = f_{soil}\delta^{13}C_{soil} + f_{DIC}(\delta^{13}C_{DIC} - \Delta^{13}C_{HCO3-CO2,\,eq}) \qquad (5)$$

Kinetic degassing:

$$\delta^{13}C_{cave} = f_{soil}\delta^{13}C_{soil} + f_{DIC}(\delta^{13}C_{DIC} - \Delta^{13}C_{HCO3-CO2,kin}) \qquad (6)$$

For the maximum (0.94), intermediate (0.90), and minimum (0.88) values of the endmember $F^{14}C$, only equilibrium fractionation during degassing can explain the observed $\delta^{13}C_{cave}$ value of approximately -26 ‰ (Fig. 9c). Kinetic fractionation scenarios result in very negative $\delta^{13}C_{cave}$ values which do not fit those measured, except when using very small kinetic fractionation factors similar to that of the equilibrium fractionation ($\Delta^{13}C_{HCO3-CO2,kin}$ of -10 ‰, see Appendix C). It is possible that kinetic fractionation occurs between Milandre cave waters and the cave air due to atmospheric ventilation which occurs year-round. The ~~fresh~~ atmospheric air which enters from the upper entrance in the summer and the lower entrance in the winter creates a concentration gradient between the CO_2 present within cave waters and the concentration in the cave atmosphere. However, the rapidly increasing pCO_2 with distance from the cave entrance (Fig. 8a) implies that the concentration gradients required for kinetic fractionation do not occur throughout most of the cave passage and that kinetic influences are probably minimal.

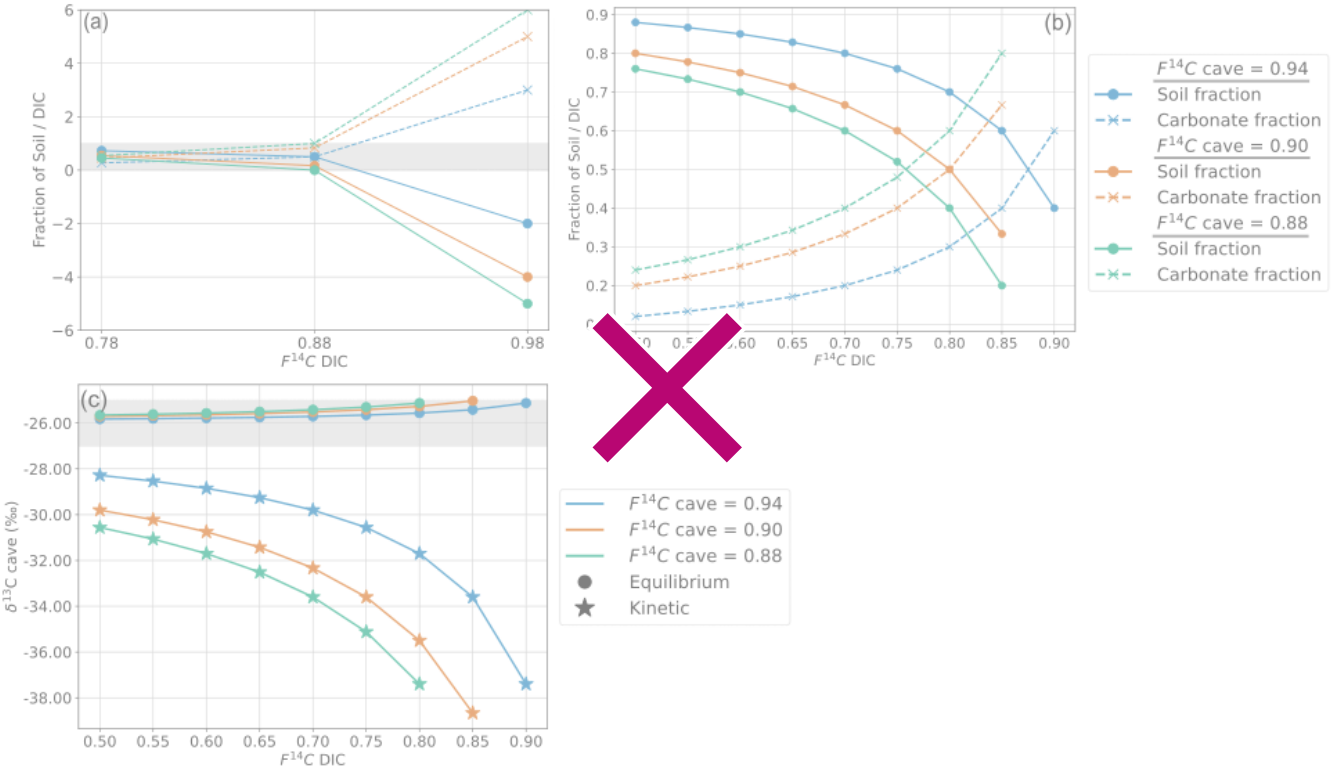
(a)
Fraction of Soil / DIC
$F^{14}C$ DIC
(b)
Fraction of Soil / DIC
$F^{14}C$ DIC
$F^{14}C$ cave = 0.94
Soil fraction
Carbonate fraction
$F^{14}C$ cave = 0.90
Soil fraction
Carbonate fraction
$F^{14}C$ cave = 0.88
Soil fraction
Carbonate fraction
(c)
$\delta^{13}C$ cave (‰)
$F^{14}C$ DIC
$F^{14}C$ cave = 0.94
$F^{14}C$ cave = 0.90
$F^{14}C$ cave = 0.88
Equilibrium
Kinetic

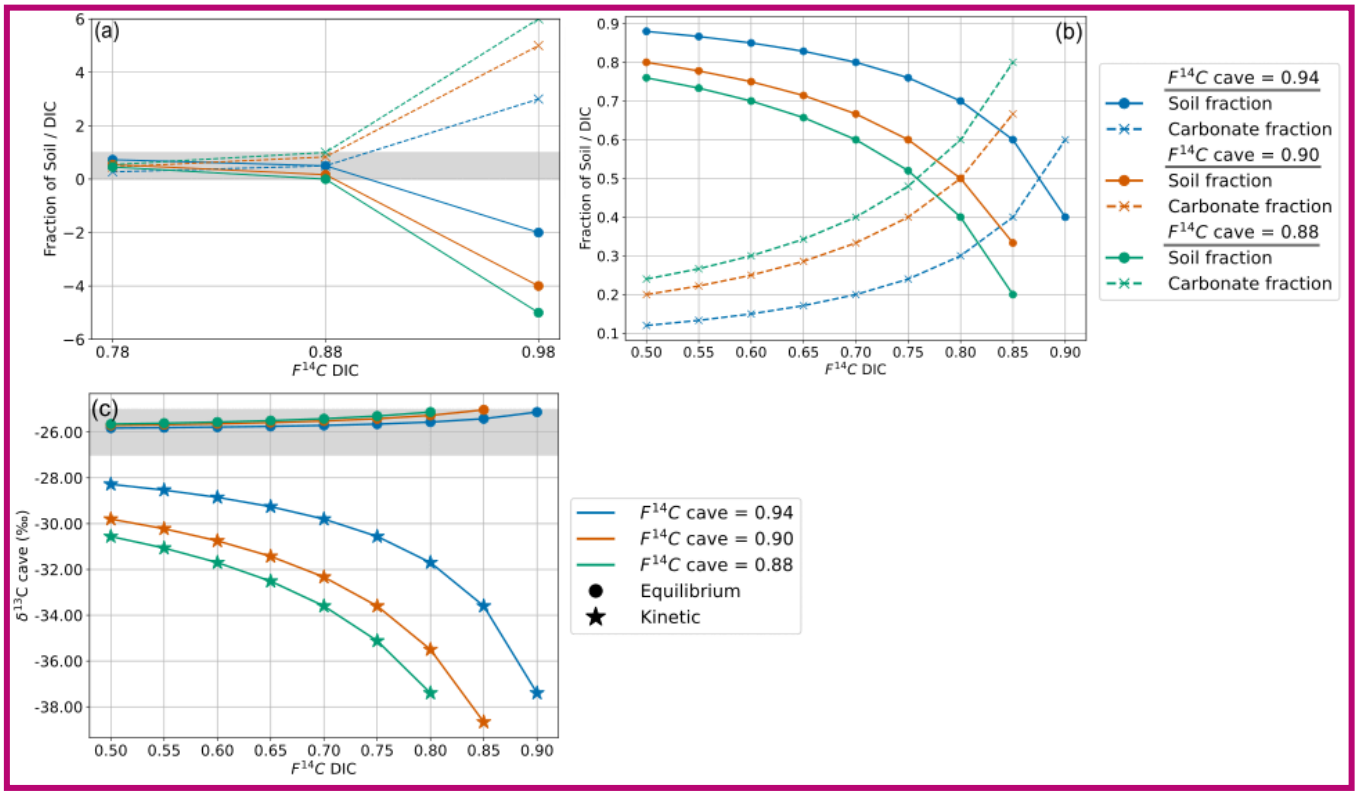

Figure 9. a) Mixing model between f_{soil} and f_{DIC} for the measured range of $F^{14}C$ DIC values and $F^{14}C$ cave values of 0.94 (blue), 0.9 (orange) 0.88 (green). The grey bar shows physically possible mixing ratios between 0 and 1. b) Mixing model between f_{soil} and f_{DIC} using the extended DIC $F^{14}C$ range and cave air $F^{14}C$ values. c) Cave air $\delta^{13}C$ for varying DIC $F^{14}C$ and cave air $F^{14}C$ values with equilibrium fractionation at -9.54 ‰ (circles) and kinetic fractionation at -30 ‰ (stars). The grey bar shows cave air $\delta^{13}C$ range which fits the measured values between -25 ‰ and -27 ‰.

Overall, the $F^{14}C_{DIC}$ measured beyond $F^{14}C$ = 0.90 is too high to reproduce our measured cave air CO_2 $F^{14}C$ and $\delta^{13}C$. ~~We measured the~~The $F^{14}C_{DIC}$ ~~in drips covering diverse locations;~~is based on the analysis of 9 drip water sites of varying drip rates~~,~~ and ecosystem coverage ~~so it is unlikely that~~over the course of one year. It is possible that the sampling set up did not capture the true range of $F^{14}C_{DIC}$ in the drip water, though this hypothesis is highly unlikely due to the diversity in drip rate and hydrological response of drips measured, and we believe our DIC data ~~is not~~to be representative of the system.

The $F^{14}C_{DIC}$ of the cave river was not measured, however previous studies ~~on~~investigating the Milandre cave river have suggested that in non-flooding conditions~~:~~ the river is fed by slow diffuse flow as the ~~epikarst~~unsaturated zone acts as a buffer, storing water and dampening the signal of normal rainfall. During flooding events, the ~~epikarst~~unsaturated zone aquifer is bypassed and the stream is mainly fed ~~by fresh~~through fracture flow (Perrin et al., 2003; Savoy et al., 2011). A diffuse flow fed river is likely to have isotopic characteristics similar to that of the drip waters, which have higher $F^{14}C$

suggesting more open system dissolution conditions. In contrast, times of flooding and soil saturation ~~results~~result in less exchange with the soil gas reservoir, leading to dissolution under more closed conditions (Perrin et al., 2003; Savoy et al., 2011). However, the drip water $F^{14}C_{DIC}$ is relatively stable over one year of monitoring in a variety of hydrological conditions, implying that variations in host rock dissolution and degassing dynamics are not the explanation for the variation in $F^{14}C$ and $\delta^{13}C$ of the endmember.

The meadow soil boreholes in the doline (Shallow 2) have similar patterns in CO_2 composition to the karst endmember, with a $\delta^{13}C$ of -26 ‰ and variable $F^{14}C$ (Fig. 10a & b). In 2022, the $F^{14}C$ in the meadow soil and karst endmember align closely over the seasonal cycle, but ~~this decouples~~then decouple slightly in 2023 during the transitional periods between winter and spring where the karst endmember $F^{14}C$ changes before the meadow. This suggests that, instead of the soils influencing the cave air due to seasonal changes in soil respiration, the cave ventilation regime ~~could~~ may be influencing the soil CO_2 $F^{14}C$. The cave ventilates upwards in winter from Downstream to Upstream in a chimney effect (and vice versa in summer). Here, the lower $F^{14}C$ karst endmember CO_2 may flow upwards through the highly fractured ~~epikarst~~unsaturated zone of the doline and ventilate the meadow soils, resulting in a mixture of low $F^{14}C$ CO_2 from the karst endmember and modern CO_2 from the soils. This possibly reflects a contribution of older CO_2 from within the karst itself, likely from a "ground air" reservoir of older respiring organic material in the ~~epikarst~~unsaturated zone as found by several other studies (Breecker et al., 2012; Noroha et al., 2015; Mattey et al., 2016; Bergel et al., 2017). ~~There are likely~~It is possible that several reservoirs of older organic material exist throughout the downstream catchment of Milandre which may contribute the low $F^{14}C$ CO_2 to the ventilating cave air in winter. In summer the ventilation reverses, and the higher $F^{14}C$ CO_2 from the soil is transported downwards into the cave, increasing the $F^{14}C$ of the cave endmember CO_2. The $F^{14}C$ of the karst endmember is always lower than the meadow soil $F^{14}C$, implying that there is always mixing between the soils and the karst endmember (which additionally also reflects the DIC contribution). Similar upwards transport of CO_2 in karst boreholes has been observed in Nerja Cave, Spain (Benavente et al., 2010; Benavente et al., 2015), and in the Gibraltar karst (Mattey et al., 2016). We do not observe significant effects of the winter upwards ventilation in the $F^{14}C$ CO_2 in any of the deeper boreholes in the meadow or any of the boreholes in the forest. This could be related to the location of Shallow 2 in the doline, whilst the rest of the boreholes are situated higher on the banks (Deep 3 and Deep 4), or further away from the doline in the forest (Deep 1 and Deep 2). The topography difference between the higher forest and lower meadow likely reflects influences of the secondary porosity in the bedrock, which is ~~possibly~~likely more highly fractured in the meadow doline formation compared to the forest. ~~leading to a greater effect of ventilation in the meadow area and an undisturbed modern ^{14}C signature of forest soils.~~ As the doline structure likely has a higher secondary porosity and is more highly fractured than the higher bedrock, ventilation effects may be more important here than at the other locations.

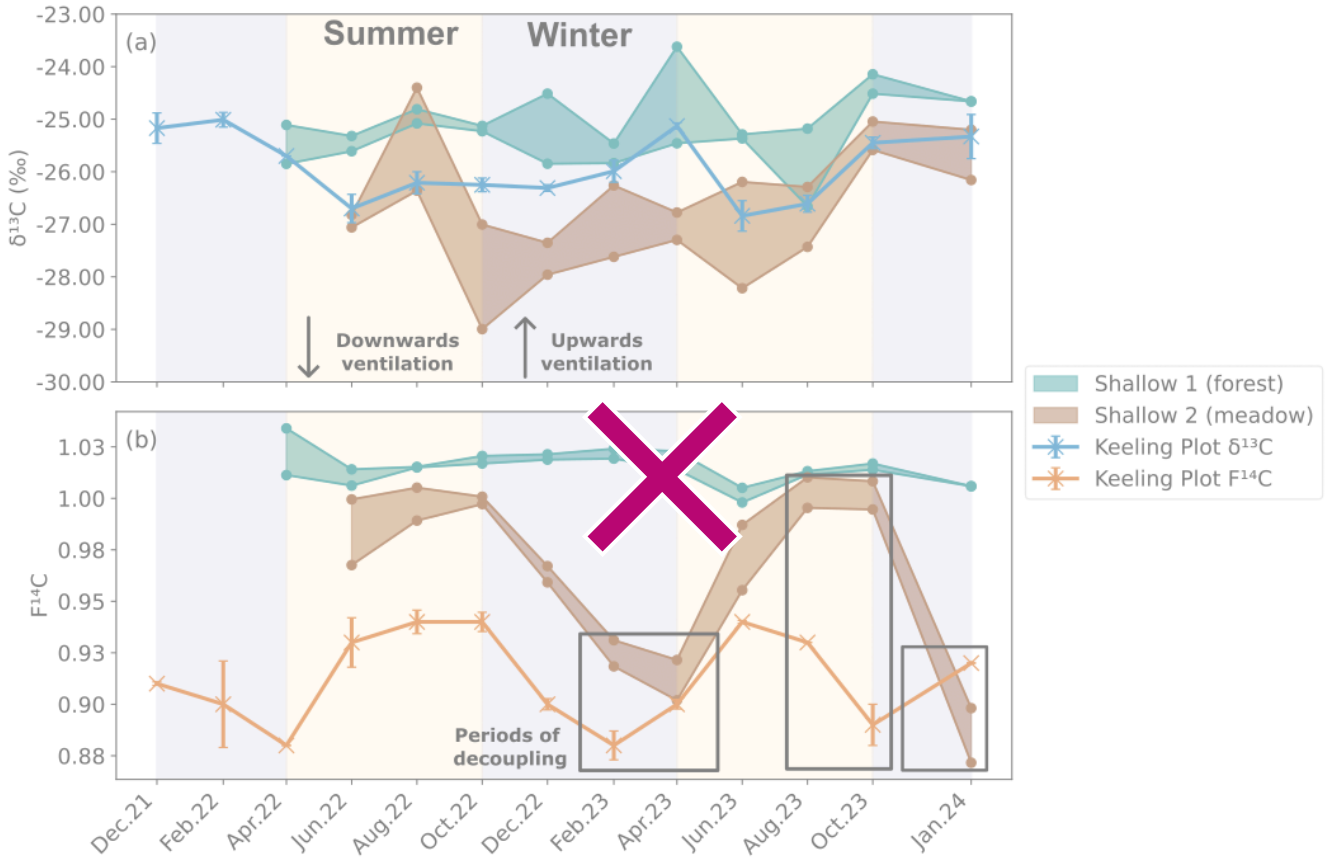
(a)
Summer
Winter
δ13C (‰)
-23.00
-24.00
-25.00
-26.00
-27.00
-28.00
-29.00
-30.00
Downwards ventilation
Upwards ventilation
(b)
F14C
1.03
1.00
0.98
0.95
0.93
0.90
0.88
Periods of decoupling
Dec.21
Feb.22
Apr.22
Jun.22
Aug.22
Oct.22
Dec.22
Feb.23
Apr.23
Jun.23
Aug.23
Oct.23
Jan.24
Shallow 1 (forest)
Shallow 2 (meadow)
Keeling Plot δ13C
Keeling Plot F14C

743

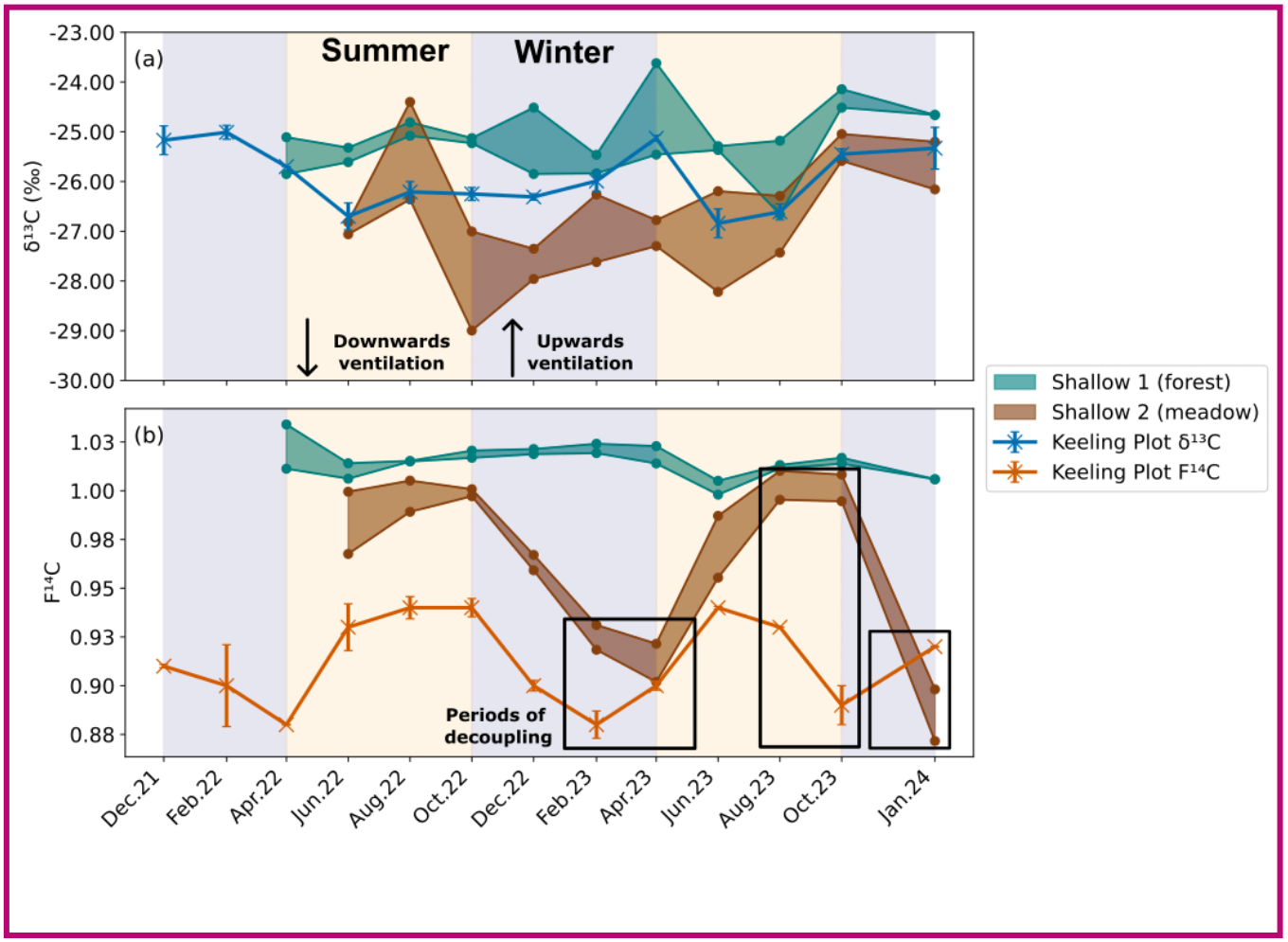

Figure 10. Comparison between the a) $\delta^{13}C$ and b) $F^{14}C$ of the shallow depth boreholes in the forest (Shallow 1, green) and meadow (Shallow 2, brown), and the Keeling plot endmembers $\delta^{13}C$ (blue) and $F^{14}C$ (orange) also show in Figure 7. Summer (yellow) and winter (blue) seasons are highlighted by the coloured background. The direction of cave ventilation is shown by the arrows with downwards ventilation (from Upstream to Downstream) in summer, and upwards ventilation (Downstream to Upstream). Periods of decoupling between the $F^{14}C$ of the meadow borehole and the cave endmember are shown in black boxes.

The accumulation of the older organic carbon in the ~~epikarst~~unsaturated zone likely occurs over time. Soil layers in karst regions often accumulate on bedrock with deep vertical fractures (Cheng et al., 2023). This decreases the ability of long-term storage of older soil carbon pools due to preferential fracture flow, also known as subsurface leakage, which destabilises the oldest soil layer and leads to export of older carbon into the ~~epikarst~~unsaturated zone (Sánchez-Cañete et al., 2018; Wan et al., 2018). Several studies have acknowledged this potential source of CO_2 produced autochthonously inside the ~~epikarst~~unsaturated zone by the microbial degradation of this old soil, plant, or root material which was previously washed

into the unsaturated zone, contributing older CO_2 to the ground air mix (Noronha et al., 2015; Bergel et al., 2017; Ding et al., 2023).

6 Conclusion

We conducted a comprehensive investigation over two years into the dynamics of CO_2 concentrations, $\delta^{13}C$ and $F^{14}C$ ~~composition~~values across different land covers and soil types within the Critical Zone at Milandre cave in northern Switzerland. Our analysis found distinct seasonal fluctuations in CO_2 levels in soil boreholes in both forest and meadow areas, with higher concentrations during summer compared to winter. Low $\delta^{13}C$ values of ~ -26 ‰ indicate respiration of C3 plants which dominate the catchment area. The stable modern $F^{14}C$ of ~ 1.00 in shallow forest boreholes indicated a year-round modern CO_2 contribution from tree and plant roots to the subsurface, consistent with a well-ventilated soil. On the other hand, samples from meadow boreholes situated in a doline with a thick, well developed soil cover displayed seasonality in $F^{14}C$ from ~ 0.88 in the winter and spring to ~ 1.00 in summer.

In the ~~epikarst~~unsaturated zone we observed substantial variability in CO_2 concentrations across the catchment (~ ~~3000~~3,000 to ~ ~~37'000~~37,000 ppmV), with higher concentrations in boreholes with forest cover than those with meadow cover. Despite differences in surface vegetation, the isotopic compositions of $\delta^{13}C$ and $F^{14}C$ remained stable in both forest and meadow environments, reflecting the dominant modern C3 vegetation signature contributing to the ground air. The year-round modern ~~epikarst~~unsaturated zone CO_2 in meadow boreholes Deep 3 and Deep 4~~, in contrast to~~ contrasts with the seasonally attenuated signal in the thicker meadow soils.

Large variations in cave air CO_2 concentrations (atmospheric to ~ ~~30'000~~30,000 ppmV), $\delta^{13}C$ (~ -9 to -25 ‰), and $F^{14}C$ (0.88 to 0.98), are controlled by ~~direction changes in the~~ seasonal temperature~~-~~-driven cave ventilation~~ regime~~. The seasonal changes in the isotopic composition of the Keeling plot derived karst endmember cannot be explained with the observed DIC $F^{14}C$ range, suggesting that bedrock dissolution and degassing dynamics are likely not the cause of the isotopic variation in the cave air. The isotopic characteristics of the cave air are comparable to those of the meadow doline soil. The seasonal variability in karst endmember CO_2 $F^{14}C$ ~~changes before the soil in times of variation~~precedes that in the soil, and is always older. This suggests that ~~the~~ cave ventilation contributes older CO_2 to the doline soils, likely sourced from a reservoir of aged organic material in the ~~epikarst~~unsaturated zone, during the upward winter ventilation regime. In summer, the reversed downwards ventilation contributes younger soil CO_2 to the cave, mixing with the older ~~epikarst~~unsaturated zone reservoir. ~~The consistently low $\delta^{13}C$ signature of the karst endmember implies that the impact of carbonate dissolution on the system is low, and that the CO_2 is contributed from either modern soils or aged organic material in the epikarst.~~

Our study provides important insights into how carbon is transported to the subsurface in karstic Critical Zones. Understanding these processes is crucial for accurate estimation of the size of subsurface CO_2 pools (ground air), and to refine terrestrial CO_2 budgets. Moving forward, it would be beneficial ~~for future research~~ to undertake more detailed investigation of CO_2 transport into the subsurface implementing ^{14}C analysis to further constrain the sources of ground air. Furthermore, higher resolution monitoring over periods of interest, could assist us in understanding short-term variations.

Appendix A

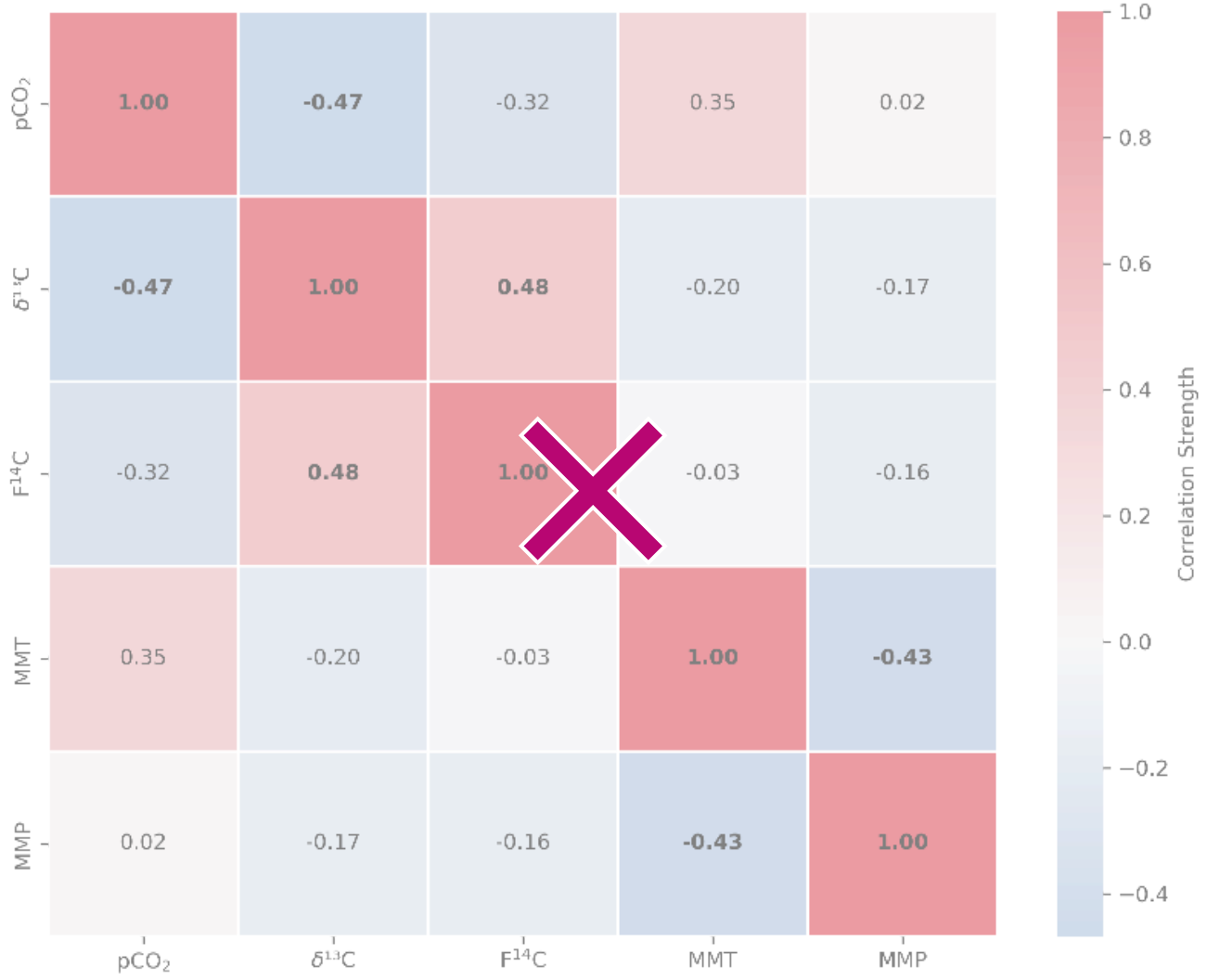
pCO2
δ13C
F14C
MMT
MMP
1.00
-0.47
-0.32
0.35
0.02
-0.47
1.00
0.48
-0.20
-0.17
-0.32
0.48
1.00
-0.03
-0.16
0.35
-0.20
-0.03
1.00
-0.43
0.02
-0.17
-0.16
-0.43
1.00
1.0
0.8
0.6
0.4
0.2
0.0
−0.2
−0.4
Correlation Strength

A1 Spearman's rank correlation matrix displaying the Spearman's rho of CO_2 concentration, $\delta^{13}C$ and $F^{14}C$, Mean Monthly Temperature (MMT) and Mean Monthly Precipitation (MMP) from Fahy weather station from samples from soil depth boreholes Shallow 1. Parameters with a significant correlation (positive or negative) are bolded and the strength of the correlation is indicated by the blue – red colour bar.

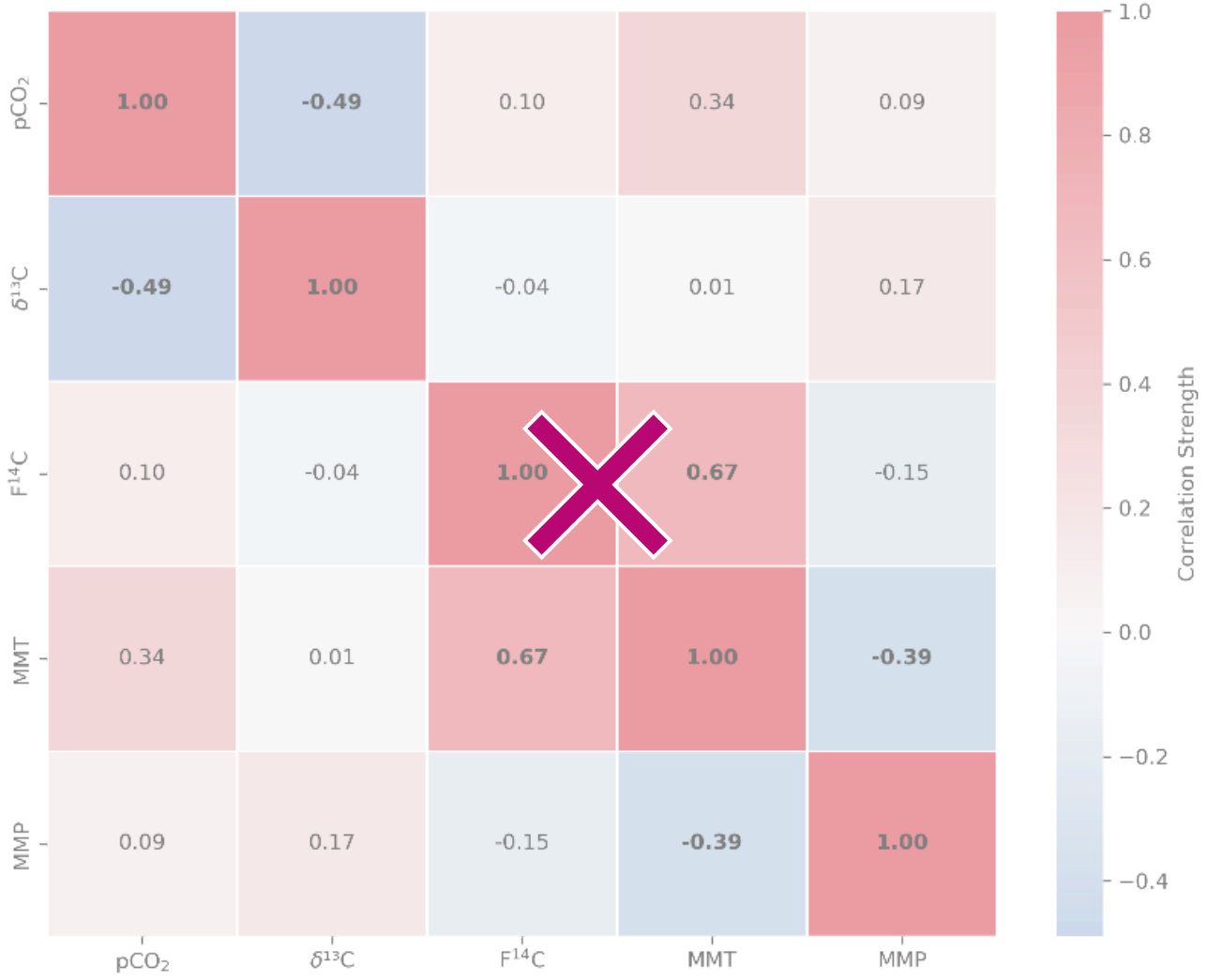
pCO2
δ13C
F14C
MMT
MMP
1.00
-0.49
0.10
0.34
0.09
-0.49
1.00
-0.04
0.01
0.17
0.10
-0.04
1.00
0.67
-0.15
0.34
0.01
0.67
1.00
-0.39
0.09
0.17
-0.15
-0.39
1.00
Correlation Strength
1.0
0.8
0.6
0.4
0.2
0.0
−0.2
−0.4

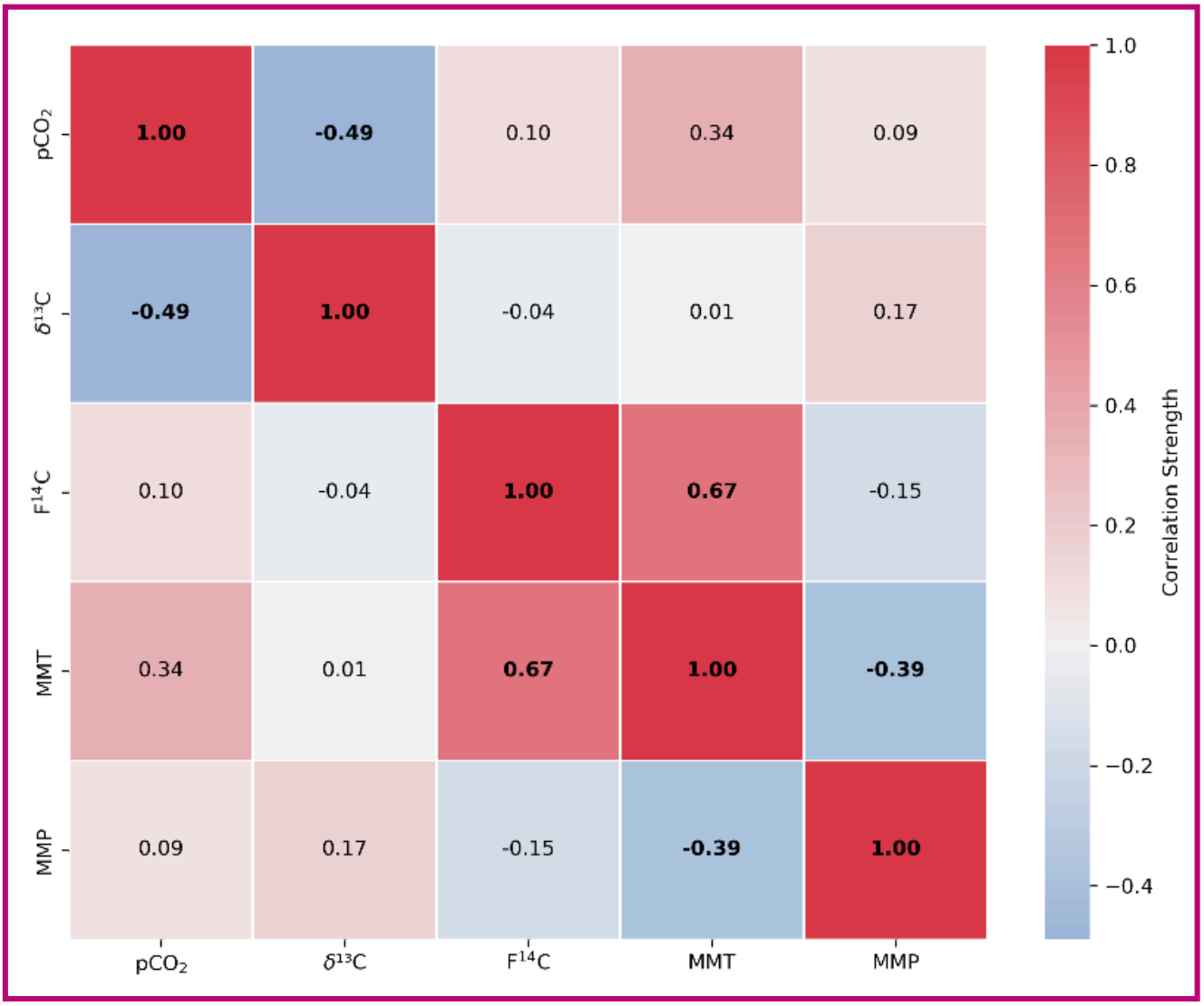

A2 Spearman's rank correlation matrix displaying the Spearman's rho of CO_2 concentration, $\delta^{13}C$ and $F^{14}C$, Mean Monthly Temperature (MMT) and Mean Monthly Precipitation (MMP) from Fahy weather station from samples from soil depth borehole Shallow 2. Parameters with a significant correlation (positive or negative) are bolded and the strength of the correlation is indicated by the blue – red colour bar.

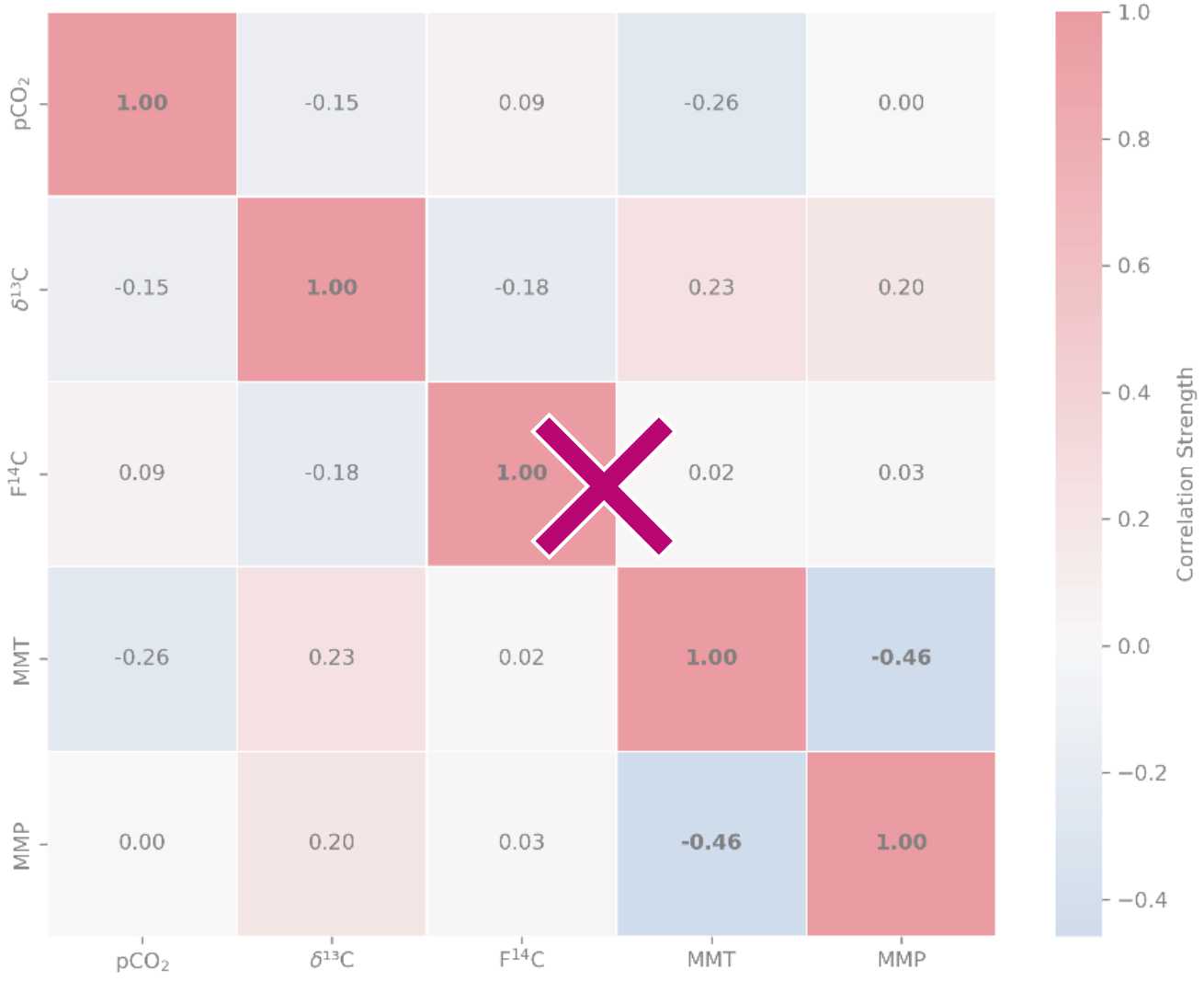
pCO2
δ13C
F14C
MMT
MMP
1.00
-0.15
0.09
-0.26
0.00
-0.15
1.00
-0.18
0.23
0.20
0.09
-0.18
1.00
0.02
0.03
-0.26
0.23
0.02
1.00
-0.46
0.00
0.20
0.03
-0.46
1.00
Correlation Strength
1.0
0.8
0.6
0.4
0.2
0.0
−0.2
−0.4

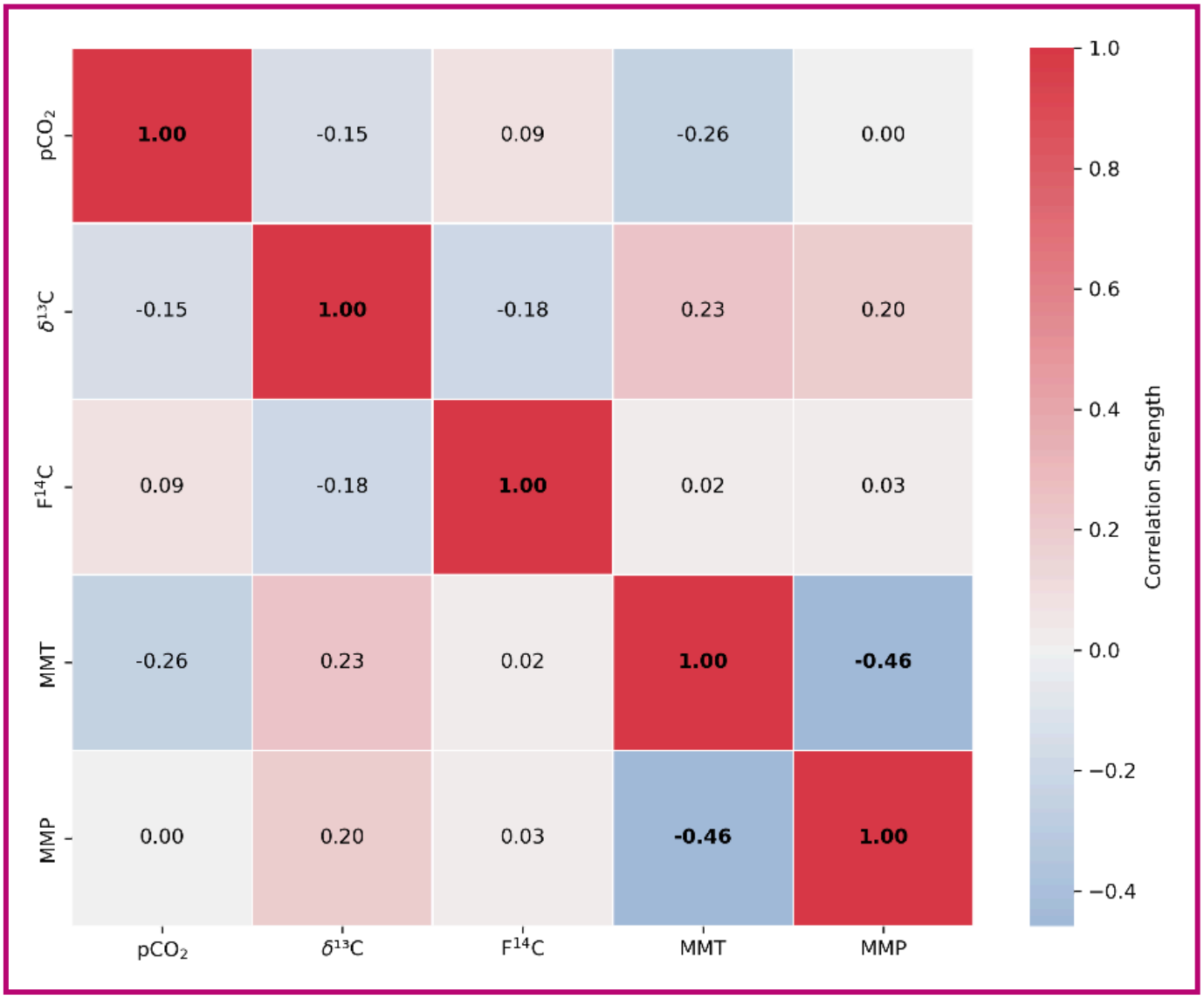

A3 Spearman's rank correlation matrix displaying the Spearman's rho of CO_2 concentration, $\delta^{13}C$ and $F^{14}C$, Mean Monthly Temperature (MMT) and Mean Monthly Precipitation (MMP) from Fahy weather station from samples from ~~epikarst~~unsaturated zone depth boreholes Deep 1 and Deep 2. Parameters with a significant correlation (positive or negative) are bolded and the strength of the correlation is indicated by the blue – red colour bar.

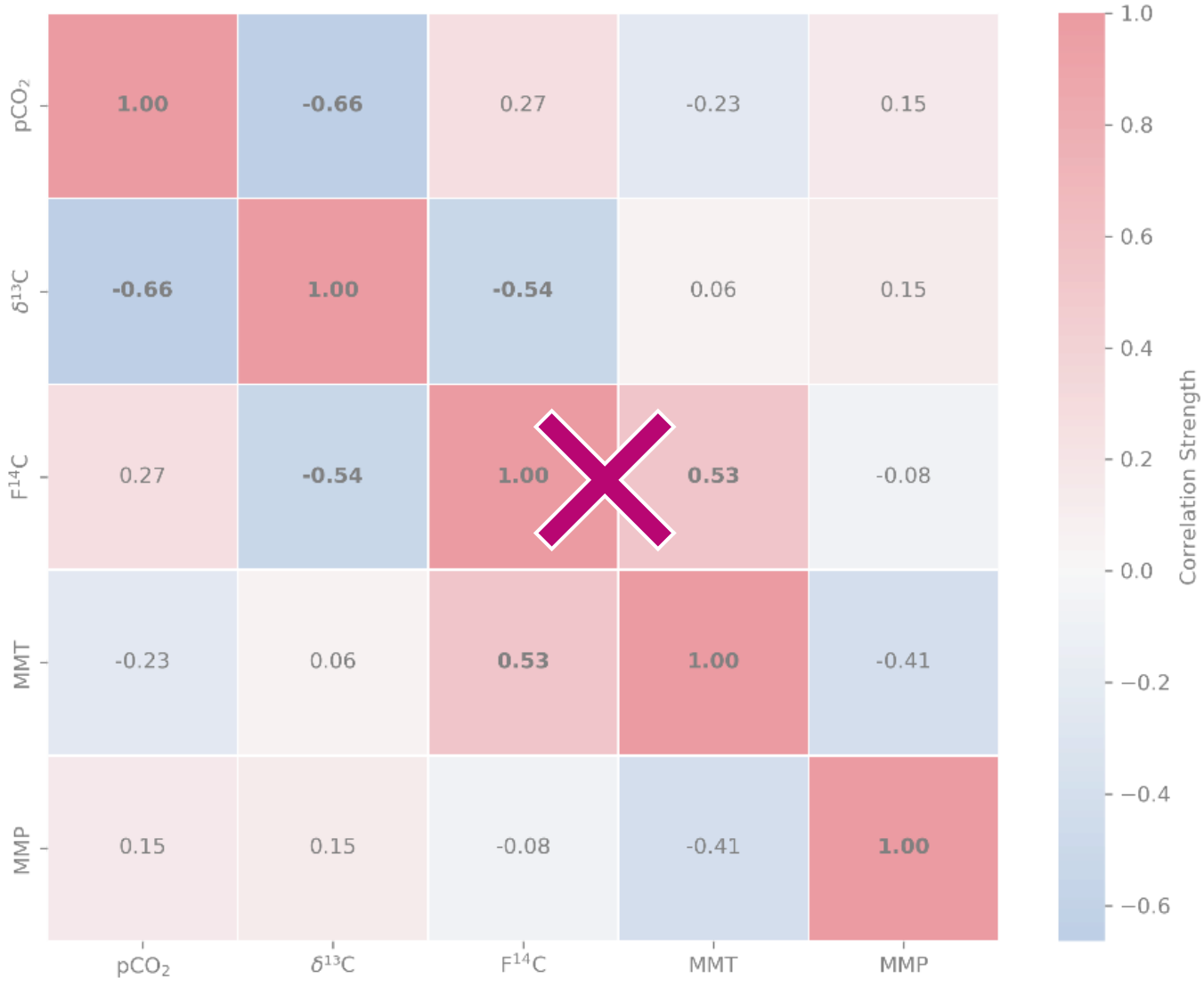
pCO2
δ13C
F14C
MMT
MMP
1.00
-0.66
0.27
-0.23
0.15
-0.66
1.00
-0.54
0.06
0.15
0.27
-0.54
1.00
0.53
-0.08
-0.23
0.06
0.53
1.00
-0.41
0.15
0.15
-0.08
-0.41
1.00
Correlation Strength
1.0
0.8
0.6
0.4
0.2
0.0
−0.2
−0.4
−0.6

A4 Spearman's rank correlation matrix displaying the Spearman's rho of CO_2 concentration, $\delta^{13}C$ and $F^{14}C$, Mean Monthly Temperature (MMT) and Mean Monthly Precipitation (MMP) from Fahy weather station from samples from ~~epikarst~~unsaturated zone depth boreholes Deep 3 and Deep 4. Parameters with a significant correlation (positive or negative) are bolded and the strength of the correlation is indicated by the blue – red colour bar.

829

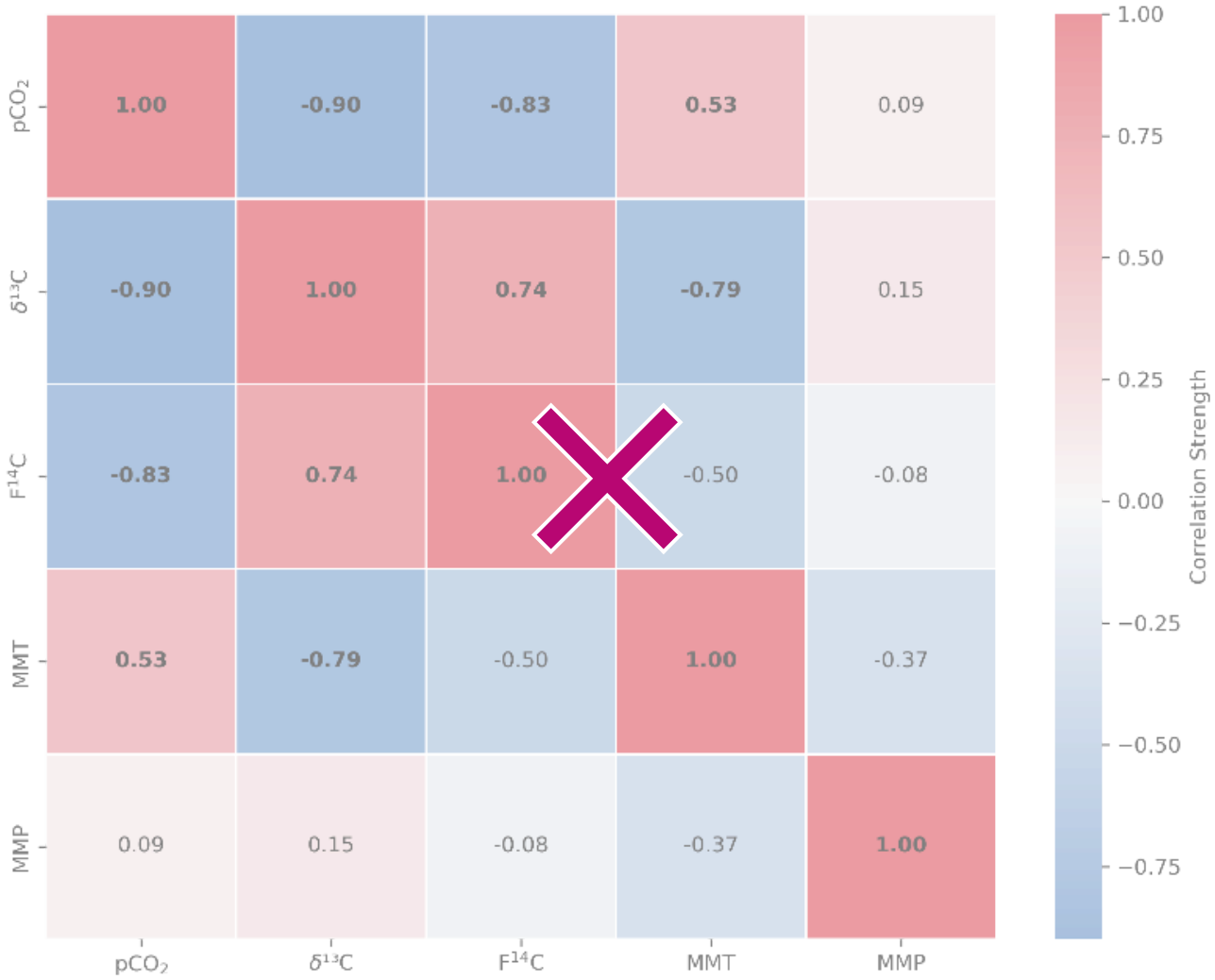
pCO2
δ13C
F14C
MMT
MMP
1.00
-0.90
-0.83
0.53
0.09
-0.90
1.00
0.74
-0.79
0.15
-0.83
0.74
1.00
-0.50
-0.08
0.53
-0.79
-0.50
1.00
-0.37
0.09
0.15
-0.08
-0.37
1.00
pCO2
δ13C
F14C
MMT
MMP
1.00
0.75
0.50
0.25
0.00
−0.25
−0.50
−0.75
Correlation Strength

A5 Spearman's rank correlation matrix displaying the Spearman's rho of CO_2 concentration, $\delta^{13}C$ and $F^{14}C$, Mean Monthly Temperature (MMT) and Mean Monthly Precipitation (MMP) from Fahy weather station from samples from the Downstream cave site. Parameters with a significant correlation (positive or negative) are bolded and the strength of the correlation is indicated by the blue – red colour bar

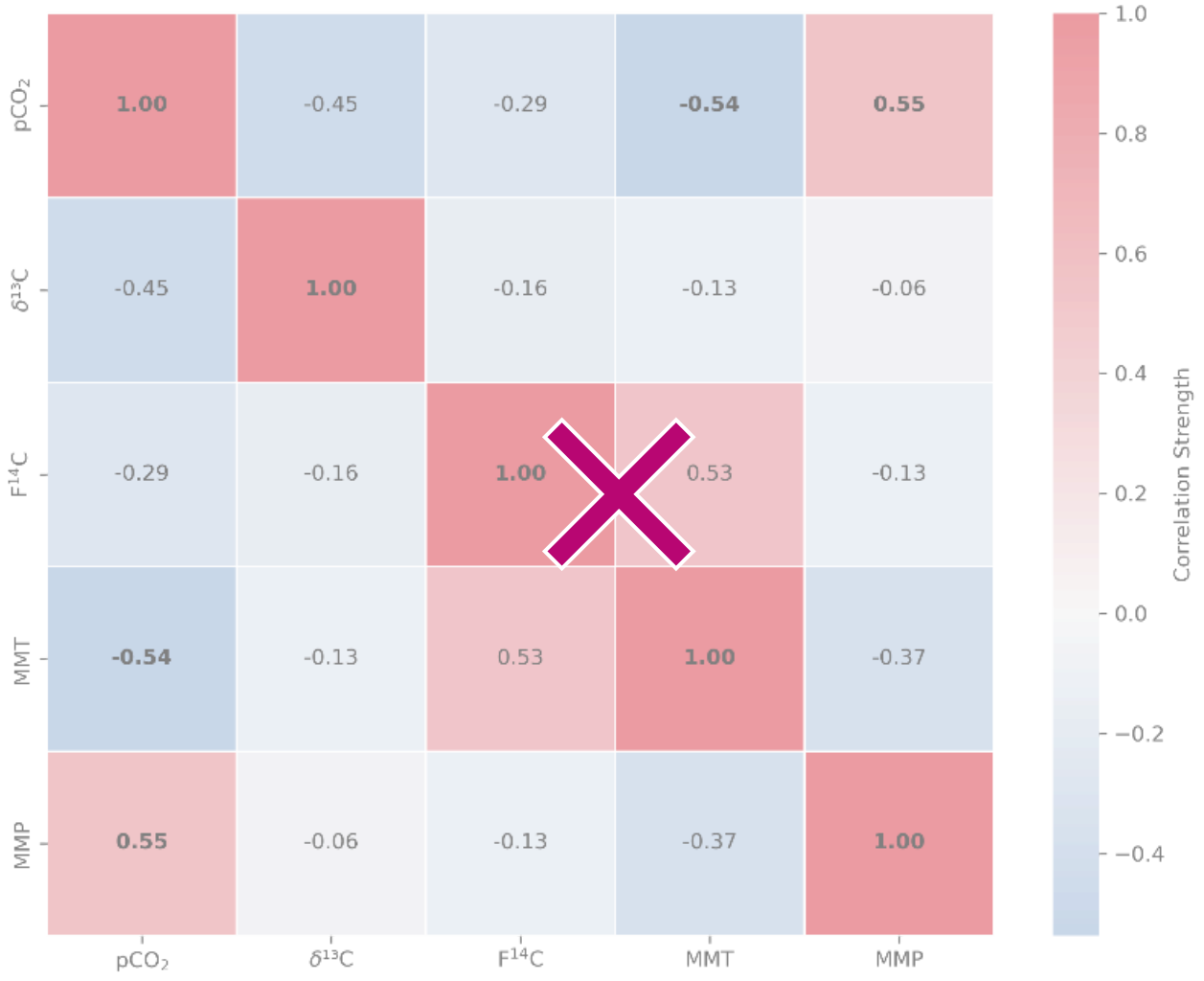
pCO2
δ13C
F14C
MMT
MMP
1.00
-0.45
-0.29
-0.54
0.55
-0.45
1.00
-0.16
-0.13
-0.06
-0.29
-0.16
1.00
0.53
-0.13
-0.54
-0.13
0.53
1.00
-0.37
0.55
-0.06
-0.13
-0.37
1.00
Correlation Strength
1.0
0.8
0.6
0.4
0.2
0.0
−0.2
−0.4

836

A6 Spearman's rank correlation matrix displaying the Spearman's rho of CO_2 concentration, $\delta^{13}C$ and $F^{14}C$, Mean Monthly Temperature (MMT) and Mean Monthly Precipitation (MMP) from Fahy weather station from samples from the Upstream cave stie. Parameters with a significant correlation (positive or negative) are bolded and the strength of the correlation is indicated by the blue – red colour bar.

B1 Drip water dissolved inorganic carbon $F^{14}C$ and AMS derived $\delta^{13}C$ from the actively dripping galleries nearby Upstream and Downstream.

Drip	Sampling date	$F^{14}C$	$F^{14}C$ % error	AMS $\delta^{13}C$ (‰)
GF1	Dec.21	0.86	0.92	-13.6
GF2	Dec.21	0.94	0.91	-14.3
GR2	Dec.21	0.91	0.92	-12.4
GR3	Dec.21	0.98	0.93	-13.5
GR4	Dec.21	0.91	0.97	-14.7
GR5	Dec.21	0.90	0.97	-14.2
GR6	Dec.21	0.85	1.02	-13.6
GF1	Feb.22	0.87	0.99	-12.6
GF3	Feb.22	0.95	0.96	-12.7
GR3	Feb.22	0.90	0.97	-14.1
GR4	Feb.22	0.89	0.99	-12.7
GR6	Feb.22	0.84	1.00	-11.9
GR6	Feb.22	0.88	0.99	-10.6
GF1	Apr.22	0.88	0.93	-12.8
GF2	Apr.22	0.93	0.89	-11.6
GF3	Apr.22	0.98	0.86	-12.1
GR1	Apr.22	0.87	0.90	-12.6
GR2	Apr.22	0.89	0.92	-12.1
GR3	Apr.22	0.90	0.93	-12.2
GR4	Apr.22	0.90	0.93	-13.4
GR5	Apr.22	0.89	0.98	-13.7
GR6	Apr.22	0.90	0.99	-13.6
GF1	Jun.22	0.87	1.11	-18.0
GF2	Jun.22	0.93	1.11	-18.9
GF3	Jun.22	0.96	1.07	-18.6
GR1	Jun.22	0.88	1.12	-17.4
GR2	Jun.22	0.93	1.09	-17.6
GR3	Jun.22	0.89	1.12	-17.9
GR4	Jun.22	0.89	1.12	-18.9
GR5	Jun.22	0.90	1.11	-17.9
GR6	Jun.22	0.92	1.12	-19.0
GF1	Aug.22	0.86	1.10	-17.1
GF2	Aug.22	0.92	1.12	-19.8

GR1	Aug.22	0.87	1.03	-8.9
GR2	Aug.22	0.91	1.09	-18.3
GR4	Aug.22	0.93	1.10	-19.2
GR5	Aug.22	0.91	1.10	-19.5
GR6	Aug.22	0.93	1.11	-20.8
GF1	Oct.22	0.84	1.05	-9.4
GF2	Oct.22	0.94	1.12	-20.3
GF3	Oct.22	0.95	1.11	-20.8
GR1	Oct.22	0.86	1.14	-17.2
GR2	Oct.22	0.88	1.14	-22.6
GR4	Oct.22	0.91	1.13	-18.7
GR5	Oct.22	0.89	1.13	-18.3
GR6	Oct.22	0.91	1.11	-19.1
GF1	Dec.22	0.86	1.01	-14.1
GF2	Dec.22	0.88	0.94	-14.1
GF3	Dec.22	0.94	0.95	-11.1
GR1	Dec.22	0.86	1.00	-11.5
GR4	Dec.22	0.89	0.98	-11.5
GR5	Dec.22	0.89	1.01	-12.6
GR6	Dec.22	0.78	1.02	-12.9

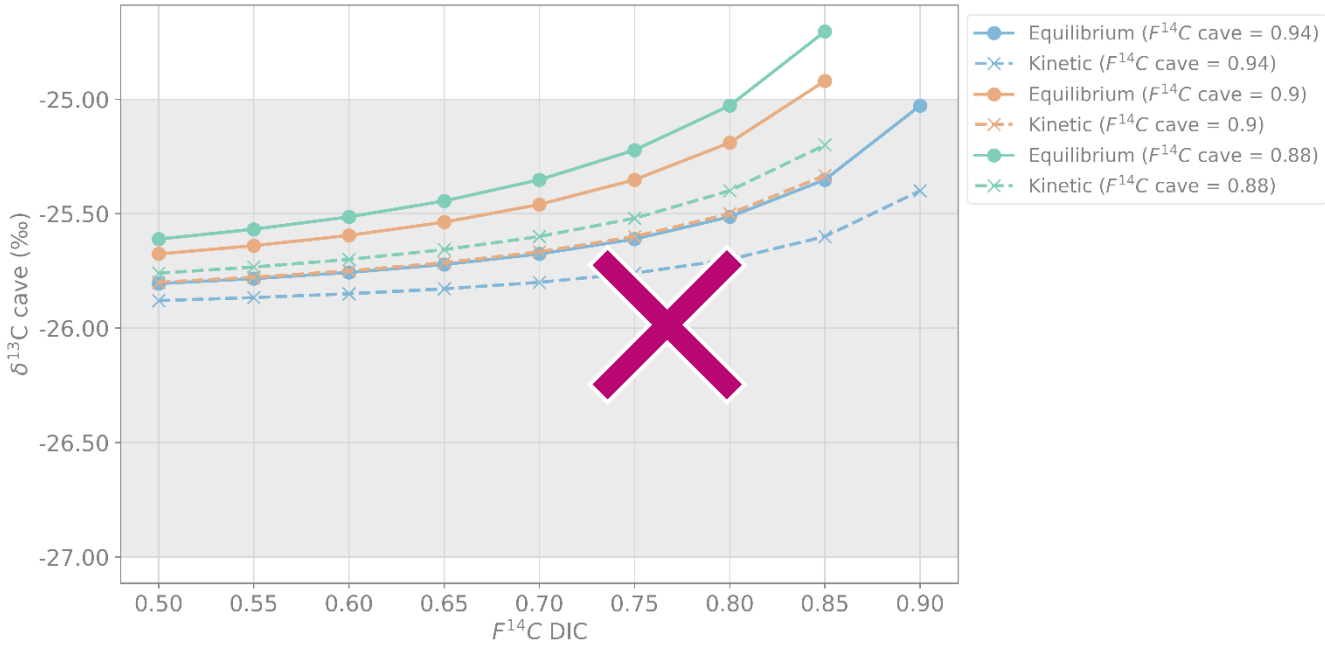

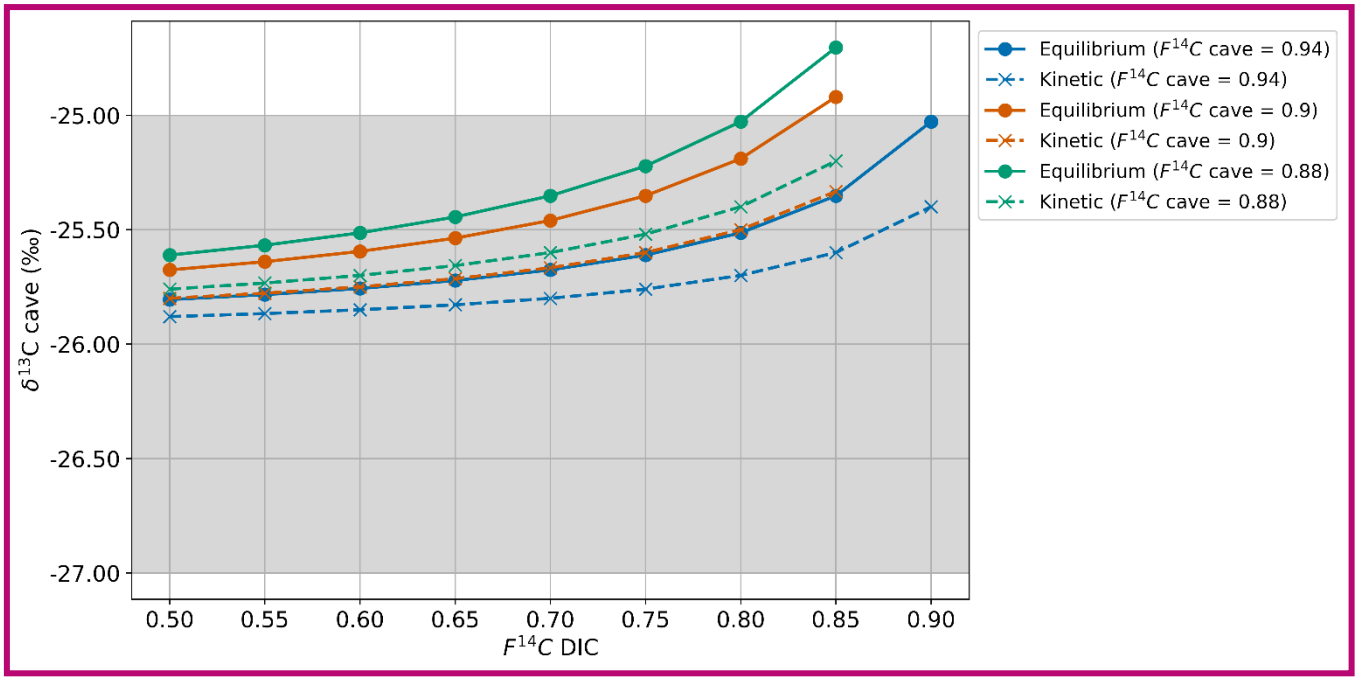

C1 Cave air $\delta^{13}C$ for varying DIC $F^{14}C$ and cave air $F^{14}C$ values with equilibrium fractionation at -9.54 ‰ (solid lines) and kinetic fractionation at -10 ‰ (dashed lines).

Code and data availability

The data, code for Spearman's rank statistics, and code to reproduce the model results are publicly available on Zenodo at https://doi.org/10.5281/zenodo.14253707.

Author contributions

Sarah Rowan: Conceptualization, Formal analysis, Investigation, Methodology, Visualization, Software, Writing – original draft preparation.

Marc Luetscher: Conceptualization, Resources, Visualization, Writing – review & editing.

Thomas Laemmel: Methodology, Validation, Writing – review & editing.

Anna Harris: Methodology, Writing – review & editing.

Sönke Szidat: Writing – review & editing.

Franziska Lechleitner: Conceptualization, Funding acquisition, Project administration, Resources, Supervision, Writing – review & editing.

Competing interests

The authors declare that they have no conflict of interest.

Disclaimer

Acknowledgements

This work was supported by the Swiss National Science Foundation Ambizione grant number 186135. We gratefully thank the staff of the Swiss Institute of Speleology and Karst Studies for their previous and continued work in Milandre cave, and for their contribution of field assistance and expertise in karst science. Special thanks to Claudio Pastore for his assistance during the ~~cross~~through trip. We express our gratitude to the Spéléo Club Jura for the initial exploration of Milandre cave, and for their persistent work and maintenance of the area. We also appreciate Daniel Pape, for continued access to the cave entrance and boreholes. Thank you also to Madalina Jaggi, Dr. Oliver Kost, and Prof. Heather Stoll for providing access and support using the Picarro system. Graphitizations and AMS measurements were also assisted by Michael Staub and Dr. Gary Salazar. Generative AI (ChatGPT versions 3.5, 4 and 4o) was used for code troubleshooting.

References

Affolter, S., Steinmann, P., Aemisegger, F., Purtschert, R., & Leuenberger, M. (2020). Origin and percolation times of Milandre Cave drip water determined by tritium time series and beryllium-7 data from Switzerland. *Journal of Environmental Radioactivity*, 222, 106346. https://doi.org/10.1016/j.jenvrad.2020.106346

Atkin, O. K., Sherlock, D., Fitter, A. H., Jarvis, S., Hughes, J. K., Campbell, C., Hurry, V., & Hodge, A. (2009). Temperature dependence of respiration in roots colonized by arbuscular mycorrhizal fungi. *New Phytologist*, 182(1), 188–199. https://doi.org/10.1111/j.1469-8137.2008.02727.x

Atkinson, T. C. (1977). Carbon dioxide in the atmosphere of the unsaturated zone: An important control of groundwater hardness in limestones. *Journal of Hydrology*, *35*(1), 111–123. https://doi.org/10.1016/0022-1694(77)90080-4

Baldini, J. U. L., Bertram, R. A., & Ridley, H. E. (2018). Ground air: A first approximation of the Earth's second largest reservoir of carbon dioxide gas. *Science of The Total Environment*, *616–617*, 1007–1013. https://doi.org/10.1016/j.scitotenv.2017.10.218

Benavente, J., Vadillo, I., Carrasco, F., Soler, A., Liñán, C., & Moral, F. (2010). Air Carbon Dioxide Contents in the Vadose Zone of a Mediterranean Karst. *Vadose Zone Journal*, 9(1), 126–136. https://doi.org/10.2136/vzj2009.0027

Benavente, J., Vadillo, I., Liñán, C., del Rosal, Y., & Carrasco, F. (2015). Influence of the ventilation of a karst show cave on the surrounding vadose CO2 reservoir (Nerja, South Spain). *Environmental Earth Sciences*, 74(12), 7731–7740. https://doi.org/10.1007/s12665-015-4709-8

Bergel, S. J., Carlson, P. E., Larson, T. E., Wood, C. T., Johnson, K. R., Banner, J. L., & Breecker, D. O. (2017). Constraining the subsoil carbon source to cave-air ~~CO2and~~CO2 and speleothem calcite in central Texas. *Geochimica et Cosmochimica Acta*, *217*, 112–127. https://doi.org/10.1016/j.gca.2017.08.017

~~Billings, S., Richter, D., & Yarie, J. (1998). Soil carbon dioxide fluxes and profile concentrations in two boreal forests. *Canadian Journal of Forest Research*, *28*. https://doi.org/10.1139/cjfr-28-12-1773~~Biagioli, F., Coleine, C., Piano, E., Nicolosi, G., Poli, A., Prigione, V., Zanellati, A., Varese, C., Isaia, M., & Selbmann, L. (2023). Microbial diversity and proxy species for human impact in Italian karst caves. *Scientific Reports*, 13(1), 689. https://doi.org/10.1038/s41598-022-26511-5

Billings, S., Richter, D., & Yarie, J. (1998). Soil carbon dioxide fluxes and profile concentrations in two boreal forests. *Canadian Journal of Forest Research*, *28*. https://doi.org/10.1139/cjfr-28-12-1773

Boyno, G., Yerli, C., Çakmakci, T., Sahin, U., & Demir, S. (2024). The effect of arbuscular mycorrhizal fungi on carbon dioxide (CO2) emission from turfgrass soil under different irrigation intervals. *Journal of Water and Climate Change*, 15(2), 541–553. https://doi.org/10.2166/wcc.2024.482

Brantley, S. L., Goldhaber, M. B., & Vala, R. K. (2007). Crossing disciplines and scales to understand the critical zone. *Elements* (Vol. 3, Issue 5, p. 8). https://doi.org/10.2113/gselements.3.5.307

Breecker, D. O. (2017). Atmospheric pCO2 control on speleothem stable carbon isotope compositions. *Earth and Planetary Science Letters*, *458*, 58–68. https://doi.org/10.1016/j.epsl.2016.10.042

Breecker, D. O., Payne, A. E., Quade, J., Banner, J. L., Ball, C. E., Meyer, K. W., & Cowan, B. D. (2012). The sources and sinks of CO2 in caves under mixed woodland and grassland vegetation. *Geochimica et Cosmochimica Acta*, *96*, 230–246. https://doi.org/10.1016/j.gca.2012.08.023

Buzjak, N., Gabrovšek, F., Perșoiu, A., Pennos, C., Paar, D., & Bočić, N. (2024). CO2 Emission from Caves by Temperature-Driven Air Circulation—Insights from Samograd Cave, Croatia. *Climate*, 12(12), Article 12. https://doi.org/10.3390/cli12120199

Campeau, A., Bishop, K., Amvrosiadi, N., Billett, M. F., Garnett, M. H., Laudon, H., Öquist, M. G., & Wallin, M. B. (2019). Current forest carbon fixation fuels stream CO2 emissions. *Nature Communications*, *10*(1), Article 1. https://doi.org/10.1038/s41467-019-09922-3

Chen, J., Li, Q., He, Q., Schröder, H. C., Lu, Z., & Yuan, D. (2023). Influence of CO2/HCO3− on Microbial Communities in Two Karst Caves with High CO2. *Journal of Earth Science*, 34(1), 145 155. https://doi.org/10.1007/s12583-020-1368-9

Cheng, K., Liu, Z., Xiong, K., He, Q., Li, Y., Cai, L., & Chen, Y. (2023). Migration of Dissolved Organic Matter in the Epikarst Fissured Soil of South China Karst. *Land*, *12*(4), Article 4. https://doi.org/10.3390/land12040887

Chiodini, G., Caliro, S., Cardellini, C., Avino, R., Granieri, D., & Schmidt, A. (2008). Carbon isotopic composition of soil CO2 efflux, a powerful method to discriminate different sources feeding soil CO2 degassing in volcanic-hydrothermal areas. *Earth and Planetary Science Letters*, *274*(3), 372–379. https://doi.org/10.1016/j.epsl.2008.07.051

Chiti, T., Neubert, R., Janssens, I., Curiel Yuste, J., Sirignano, C., & Certini, G. (2011). Radiocarbon based assessment of soil organic matter contribution to soil respiration in a pine stand of the Campine region, Belgium. *Plant and Soil*, *344*, 273–282. https://doi.org/10.1007/s11104-011-0745-7

Diao, H., Wang, A., Yuan, F., Guan, D., & Wu, J. (2022). Autotrophic respiration modulates the carbon isotope composition of soil respiration in a mixed forest. *Science of The Total Environment*, 807, 150834. https://doi.org/10.1016/j.scitotenv.2021.150834

Ding, Y., Wang, D., Zhao, G., Chen, S., Sun, T., Sun, H., Wu, C., Li, Y., Yu, Z., Li, Y., & Chen, Z. (2023). The contribution of wetland plant litter to soil carbon pool: Decomposition rates and priming effects. *Environmental Research*, *224*, 115575. https://doi.org/10.1016/j.envres.2023.115575

Dulinski, M., & Rozanski, K. (1990). 'Formation of 13C/12C Isotope Ratios in Speleothems: A Semi-Dynamic Model'. *Radiocarbon*, *32*(1), 7–16. https://doi.org/10.1017/S0033822200039904

Fairchild, I. J., & Baker, A. (2012). *Speleothem Science: From Process to Past Environments*. John Wiley & Sons. https://doi.org/10.1002/9781444361094.ch5

Fohlmeister, J., Scholz, D., Kromer, B., & Mangini, A. (2011). Modelling carbon isotopes of carbonates in cave drip water. *Geochimica et Cosmochimica Acta*, *75*(18), 5219–5228. https://doi.org/10.1016/j.gca.2011.06.023

~~Frisia, S., Fairchild, I. J., Fohlmeister, J., Miorandi, R., Spötl, C., & Borsato, A. (2011). Carbon mass-balance modelling and carbon isotope exchange processes in dynamic caves. *Geochimica et Cosmochimica Acta*, *75*(2), 380–400. https://doi.org/10.1016/j.gca.2010.10.021¶~~

~~¶~~

~~Garagnon, J., Luetscher, M., & Weber, E. (2022, July 1). *Ventilation regime in a karstic system (Milandre Cave, Switzerland)*. Conference: 18th International Congress of Speleology, Savoie Mont Blanc.~~Frieling, J., Svensen, H. H., Planke, S., Cramwinckel, M. J., Selnes, H., & Sluijs, A. (2016). Thermogenic methane release as a cause for the long duration of the PETM. *Proceedings of the National Academy of Sciences*, 113(43), 12059–12064. https://doi.org/10.1073/pnas.1603348113

Frisia, S., Fairchild, I. J., Fohlmeister, J., Miorandi, R., Spötl, C., & Borsato, A. (2011). Carbon mass-balance modelling and carbon isotope exchange processes in dynamic caves. *Geochimica et Cosmochimica Acta*, *75*(2), 380–400. https://doi.org/10.1016/j.gca.2010.10.021

Fitter, A. H., Heinemeyer, A., & Staddon, P. L. (2000). The impact of elevated CO2 and global climate change on arbuscular mycorrhizas: A mycocentric approach. New *Phytologist*, 147(1), 179–187. https://doi.org/10.1046/j.1469-8137.2000.00680.x

Garagnon, J., Luetscher, M., & Weber, E. (2022, July 1). *Ventilation regime in a karstic system (Milandre Cave, Switzerland)*. Conference: 18th International Congress of Speleology, Savoie Mont Blanc.

Gherman, V. D., Boboescu, I. Z., Pap, B., Kondorosi, É., Gherman, G., & Maróti, G. (2014). An Acidophilic Bacterial-Archaeal-Fungal Ecosystem Linked to Formation of Ferruginous Crusts and Stalactites. *Geomicrobiology Journal*, 31(5), 407–418. https://doi.org/10.1080/01490451.2013.836580

Gigon, R. and Wenger, R. (1986): *Inventaire spe´le´ologique de la Suisse, canton du Jura*. La Chaux-de-Fonds: Commission Spéléologie de la ~~Socie´te´ helve´tique~~Société helvétique des sciences naturelles.

Girault, F., Adhikari, L. B., France-Lanord, C., Agrinier, P., Koirala, B. P., Bhattarai, M., Mahat, S. S., Groppo, C., Rolfo, F., Bollinger, L., & Perrier, F. (2018). Persistent CO2 emissions and hydrothermal unrest following the 2015 earthquake in Nepal. *Nature Communications*, *9*(1), 2956. https://doi.org/10.1038/s41467-018-05138-z

Gogoleva, N. E., Nasyrova, M. A., Balkin, A. S., Chervyatsova, O. Y., Kuzmina, L. Y., Shagimardanova, E. I., Gogolev, Y. V., & Plotnikov, A. O. (2024). Flourishing in Darkness: Protist Communities of Water Sites in Shulgan-Tash Cave (Southern Urals, Russia). *Diversity*, 16(9), Article 9. https://doi.org/10.3390/d16090526

Hasenmueller, E. A., Gu, X., Weitzman, J. N., Adams, T. S., Stinchcomb, G. E., Eissenstat, D. M., Drohan, P. J., Brantley, S. L., & Kaye, J. P. (2017). Weathering of rock to regolith: The activity of deep roots in bedrock fractures. *Geoderma*, 300, 11–31. https://doi.org/10.1016/j.geoderma.2017.03.020

Hashimoto, S., & Komatsu, H. (2006). Relationships between soil CO2 concentration and CO2 production, temperature, water content, and gas diffusivity: Implications for field studies through sensitivity analyses. *Journal of Forest Research*, 11(1), 41–50. https://doi.org/10.1007/s10310-005-0185-4

Jeannin, P.-Y. (1998). *Structure et comportement hydraulique des aquifères karstiques*, [Unpublished doctoral dissertation], University of Neuchâtel.

Jeannin, P.-Y., Hessenauer, M., Malard, A., & Chapuis, V. (2016). Impact of global change on karst groundwater mineralization in the Jura Mountains. *Science of The Total Environment*, 541, 1208–1221. https://doi.org/10.1016/j.scitotenv.2015.10.008

Kähkönen, M., Wittmann, C., Kurola, J., Ilvesniemi, H., & Salkinoja-Salonen, M. (2001). Microbial activity of boreal forest soil in a cold climate. *Boreal Environment Research*, *6*, 19–28.

Keeling, C. D. (1961). The concentration and isotopic abundances of carbon dioxide in rural and marine air. *Geochimica et Cosmochimica Acta*, *24*(3), 277–298. https://doi.org/10.1016/0016-7037(61)90023-0

Keller, C. K. (2019). Carbon Exports from Terrestrial Ecosystems: A Critical-Zone Framework. *Ecosystems*, *22*(8), 1691–1705. https://doi.org/10.1007/s10021-019-00375-9

~~Kokoska, S., & Zwillinger, D. (2000). *CRC Standard Probability and Statistics Tables and Formulae, Student Edition*. CRC Press.~~Kiers, E. T., Duhamel, M., Beesetty, Y., Mensah, J. A., Franken, O., Verbruggen, E., Fellbaum, C. R., Kowalchuk, G. A., Hart, M. M., Bago, A., Palmer, T. M., West, S. A., Vandenkoornhuyse, P., Jansa, J., & Bücking, H. (2011). Reciprocal Rewards Stabilize Cooperation in the Mycorrhizal Symbiosis. *Science*, 333(6044), 880–882. https://doi.org/10.1126/science.1208473

Kokoska, S., & Zwillinger, D. (2000). *CRC Standard Probability and Statistics Tables and Formulae, Student Edition*. CRC Press.

Kosznik-Kwaśnicka, K., Golec, P., Jaroszewicz, W., Lubomska, D., & Piechowicz, L. (2022). Into the Unknown: Microbial Communities in Caves, Their Role, and Potential Use. *Microorganisms*, 10(2), Article 2. https://doi.org/10.3390/microorganisms10020222

Kottek, M., Grieser, J., Beck, C., Rudolf, B., & Rubel, F. (2006). World Map of the Köppen-Geiger Climate Classification Updated. *Meteorologische Zeitschrift*, *15*, 259–263. https://doi.org/10.1127/0941-2948/2006/0130

Kukuljan, L., Gabrovšek, F., Covington, M. D., & Johnston, V. E. (2021). CO2 dynamics and heterogeneity in a cave atmosphere: Role of ventilation patterns and airflow pathways. *Theoretical and Applied Climatology*, *146*(1), 91–109. https://doi.org/10.1007/s00704-021-03722-w

Lekberg, Y., & Koide, R. T. (2008). Effect of soil moisture and temperature during fallow on survival of contrasting isolates of arbuscular mycorrhizal fungi. *Botany*, *86*(10), 1117–1124. https://doi.org/10.1139/B08-077

Li, Y., Yang, Y., Wang, X., Luo, W., Zhao, J., Sun, Z., Ye, Z., Chen, X., Shi, X., Xu, Y., & Baker, J. L. (2024). Sources and transport of CO2 in the karst system of Jiguan Cave, Funiu Mountains, China. *Science of The Total Environment*, *918*, 170507. https://doi.org/10.1016/j.scitotenv.2024.170507

Martin-Pozas, T., Cuezva, S., Fernandez-Cortes, A., Cañaveras, J. C., Benavente, D., Jurado, V., Saiz-Jimenez, C., Janssens, I., Seijas, N., & Sanchez-Moral, S. (2022). Role of subterranean microbiota in the carbon cycle and greenhouse gas dynamics. *Science of The Total Environment*, 831, 154921. https://doi.org/10.1016/j.scitotenv.2022.154921

Mattey, D. P., Atkinson, T. C., Barker, J. A., Fisher, R., Latin, J.-P., Durrell, R., & Ainsworth, M. (2016). Carbon dioxide, ground air and carbon cycling in Gibraltar karst. *Geochimica et Cosmochimica Acta*, *184*, 88–113. https://doi.org/10.1016/j.gca.2016.01.041

McDonough, L. K., Iverach, C. P., Beckmann, S., Manefield, M., Rau, G. C., Baker, A., & Kelly, B. F. J. (2016). Spatial variability of cave-air carbon dioxide and methane concentrations and isotopic compositions in a semi-arid karst environment. *Environmental Earth Sciences*, *75*(8), 700. https://doi.org/10.1007/s12665-016-5497-5

MeteoSwiss. Retrieved 26 August 2024, from https://www.meteoswiss.admin.ch/

Mickler, P. J., Carlson, P., Banner, J. L., Breecker, D. O., Stern, L., & Guilfoyle, A. (2019). Quantifying carbon isotope disequilibrium during in-cave evolution of drip water along discreet flow paths. *Geochimica et Cosmochimica Acta*, *244*, 182–196. https://doi.org/10.1016/j.gca.2018.09.027

Milanolo, S., & Gabrovšek, F. (2015). Estimation of carbon dioxide flux degassing from percolating waters in a karst cave: Case study from Bijambare cave, Bosnia and Herzegovina. *Geochemistry*, *75*(4), 465–474. https://doi.org/10.1016/j.chemer.2015.10.004

Mook, W. G., Bommerson, J. C., & Staverman, W. H. (1974). Carbon isotope fractionation between dissolved bicarbonate and gaseous carbon dioxide. *Earth and Planetary Science Letters*, *22*(2), 169–176. https://doi.org/10.1016/0012-821X(74)90078-8

Moyes, A. B., Gaines, S. J., Siegwolf, R. T. W., & Bowling, D. R. (2010). Diffusive fractionation complicates isotopic partitioning of autotrophic and heterotrophic sources of soil respiration. *Plant, Cell and Environment*, 33(11), 1804–1819. Scopus. https://doi.org/10.1111/j.1365-3040.2010.02185.x

Muhr, J., Borken, W., & Matzner, E. (2009). Effects of soil frost on soil respiration and its radiocarbon signature in a Norway spruce forest soil. *Global Change Biology*, *15*(4), 782–793. https://doi.org/10.1111/j.1365-2486.2008.01695.x

Nakano, A., Takahashi, K., & Kimura, M. (1999). The carbon origin of arbuscular mycorrhizal fungi estimated from δ13C values of individual spores. *Mycorrhiza*, 9(1), 41–47. https://doi.org/10.1007/s005720050261

Noronha, A. L., Johnson, K. R., Southon, J. R., Hu, C., Ruan, J., & McCabe-Glynn, S. (2015). Radiocarbon evidence for decomposition of aged organic matter in the vadose zone as the main source of speleothem carbon. *Quaternary Science Reviews*, *127*, 37–47. https://doi.org/10.1016/j.quascirev.2015.05.021

Pataki, D. E., Ehleringer, J. R., Flanagan, L. B., Yakir, D., Bowling, D. R., Still, C. J., Buchmann, N., Kaplan, J. O., & Berry, J. A. (2003). The application and interpretation of Keeling plots in terrestrial carbon cycle research. *Global Biogeochemical Cycles*, 17(1). https://doi.org/10.1029/2001GB001850

Perrin, J., Jeannin, P.-Y., & Zwahlen, F. (2003). Epikarst storage in a karst aquifer: A conceptual model based on isotopic data, Milandre test site, Switzerland. *Journal of Hydrology*, 279(1), 106–124. https://doi.org/10.1016/S0022-1694(03)00171-9

Planavsky, N., Partin, C., & Bekker, A. (2015). Carbon Isotopes as a Geochemical Tracer. *Encyclopedia of Astrobiology*, (pp. 366–371). https://doi.org/10.1007/978-3-662-44185-5_228

Powers, H. H., Hunt, J. E., Hanson, D. T., & McDowell, N. G. (2010). A dynamic soil chamber system coupled with a tunable diode laser for online measurements of δ13C, δ18O, and efflux rate of soil-respired CO2. *Rapid Communications in Mass Spectrometry*, 24(3), 243–253. https://doi.org/10.1002/rcm.4380

Pumpanen, J., Ilvesniemi, H., ~~PERÄMÄKI~~Perämäki, M., & Hari, P. (2003). Seasonal patterns of soil CO2 efflux and soil air CO2 concentration in a Scots pine forest: Comparison of two chamber techniques. *Global Change Biology*, *9*(3), 371–382. https://doi.org/10.1046/j.1365-2486.2003.00588.x

Ravn, N. R., Michelsen, A., & Reboleira, A. S. P. S. (2020). Decomposition of Organic Matter in Caves. *Frontiers in Ecology and Evolution*, *8*. https://doi.org/10.3389/fevo.2020.554651

Reimer, P., Brown, T., & Reimer, R. (2004). Discussion: Reporting and Calibration of Post-Bomb 14C Data. *Radiocarbon*, 46, 1299–1304. https://doi.org/10.1017/S0033822200033154

Risk, D., Nickerson, N., Phillips, C. L., Kellman, L., & Moroni, M. (2012). Drought alters respired δ13CO2 from autotrophic, but not heterotrophic soil respiration. *Soil Biology and Biochemistry*, 50, 26–32. https://doi.org/10.1016/j.soilbio.2012.01.025

Sánchez-Cañete, E. P., Barron-Gafford, G. A., & Chorover, J. (2018). A considerable fraction of soil-respired CO2 is not emitted directly to the atmosphere. *Scientific Reports*, *8*(1), 13518. https://doi.org/10.1038/s41598-018-29803-x

Savoy, L., Surbeck, H., & Hunkeler, D. (2011). Radon and CO2 as natural tracers to investigate the recharge dynamics of karst aquifers. *Journal of Hydrology*, 406(3), 148–157. https://doi.org/10.1016/j.jhydrol.2011.05.031

Schoell, M. (1980). The hydrogen and carbon isotopic composition of methane from natural gases of various origins. *Geochimica et Cosmochimica Acta*, 44(5), 649–661. https://doi.org/10.1016/0016-7037(80)90155-6

Shi, Z., Allison, S. D., He, Y., Levine, P. A., Hoyt, A. M., Beem-Miller, J., Zhu, Q., Wieder, W. R., Trumbore, S., & Randerson, J. T. (2020). The age distribution of global soil carbon inferred from radiocarbon measurements. *Nature Geoscience*, *13*(8), 555–559. https://doi.org/10.1038/s41561-020-0596-z

Sommaruga, A. (2011). From the central Jura mountains to the molasse basin (France and Switzerland). *Swiss Bulletin Fuer Angewandte Geologie*, *16*(2), 63–75.

Staddon, P. (2004). Carbon isotopes in functional soil ecology. *Trends in Ecology & Evolution*, 19, 148–154. https://doi.org/10.1016/j.tree.2003.12.003

Stewart, B., Zhi, W., Sadayappan, K., Sterle, G., Harpold, A., & Li, L. (2022). Soil CO2 Controls Short-Term Variation but Climate Regulates Long-Term Mean of Riverine Inorganic Carbon. *Global Biogeochemical Cycles*, 36(8), e2022GB007351. https://doi.org/10.1029/2022GB007351

Stickler, W., Trimborn, P., Maloszewski, P., Rank, D., Papesch, W., Reichert, B. (1997). Environmental Isotope Investigations. *Acata Carsologica*, 26/1, 236 – 259.

Suess, E., & Whiticar, M. J. (1989). Methane-derived CO2 in pore fluids expelled from the Oregon subduction zone. *Palaeogeography, Palaeoclimatology, Palaeoecology*, 71(1), 119–136. https://doi.org/10.1016/0031-0182(89)90033-3

Swisstopo. Retrieved 1 December 2024, from https://www.swisstopo.admin.ch/en

Synal, H.-A., Stocker, M., & Suter, M. (2007). MICADAS: A new compact radiocarbon AMS system. *Nuclear Instruments and Methods in Physics Research Section B: Beam Interactions with Materials and Atoms*, *259*(1), 7–13. https://doi.org/10.1016/j.nimb.2007.01.138

Szidat, S. (2020). ^{14}C Research at the Laboratory for the Analysis of Radiocarbon with AMS (LARA), University of Bern. *CHIMIA*, *74*(12), Article 12. https://doi.org/10.2533/chimia.2020.1010

Treseder, K. K., & Allen, M. F. (2000). Mycorrhizal fungi have a potential role in soil carbon storage under elevated CO2 and nitrogen deposition. *New Phytologist*, 147(1), 189–200. https://doi.org/10.1046/j.1469-8137.2000.00690.x

Tomczyk-Żak, K., & Zielenkiewicz, U. (2016). Microbial Diversity in Caves. *Geomicrobiology Journal*, 33(1), 20–38. https://doi.org/10.1080/01490451.2014.1003341

Trumbore, S. (2000). Age of Soil Organic Matter and Soil Respiration: Radiocarbon Constraints on Belowground C Dynamics. *Ecological Applications*, *10*(2), 399–411. https://doi.org/10.1890/1051-0761(2000)010[0399:AOSOMA]2.0.CO;2

Tune, A., Druhan, J., Wang, J., Bennett, P., & Rempe, D. (2020). Carbon Dioxide Production in Bedrock Beneath Soils Substantially Contributes to Forest Carbon Cycling. *Journal of Geophysical Research: Biogeosciences*, *125*. https://doi.org/10.1029/2020JG005795

Unger, S., Máguas, C., Pereira, J. S., Aires, L. M., David, T. S., & Werner, C. (2010). Disentangling drought-induced variation in ecosystem and soil respiration using stable carbon isotopes. *Oecologia*, 163(4), 1043–1057. https://doi.org/10.1007/s00442-010-1576-6

Vadillo, I., Ojeda, L., Benavente, J., Liñán, C., Carrasco, F., del Padial, R. (2016). Datación del CO2 mediante 14C del aire de la zona no saturada en la parcela experimental de la Cueva de Nerja (Andalucía, Málaga). En: Andreo, B. y Durán, J.J. (Eds). *El karst y el hombre: las cuevas como Patrimonio Mundial*. Asociación Cuevas Turísticas Españolas, 327–334.

Van Rossum, G. & Drake, F.L., 2009. *Python 3 Reference Manual*, Scotts Valley, CA: CreateSpace.

Vaughn, L. J. S., & Torn, M. S. (2018). Radiocarbon measurements of ecosystem respiration and soil pore-space CO_2 in Utqiaġvik (Barrow), Alaska. *Earth System Science Data*, *10*(4), 1943–1957. https://doi.org/10.5194/essd-10-1943-2018

Vuilleumier, C., Jeannin, P.-Y., Hessenauer, M., & Perrochet, P. (2021). Hydraulics and turbidity generation in the Milandre Cave (Switzerland). *Water Resources Research*, 57. https://doi. org/10.1029/2020WR029550

Wacker, L., Christl, M., & Synal, H.-A. (2010b). Bats: A new tool for AMS data reduction. *Nuclear Instruments and Methods in Physics Research Section B: Beam Interactions with Materials and Atoms*, *268*(7), 976–979. https://doi.org/10.1016/j.nimb.2009.10.078

Wacker, L., Němec, M., & Bourquin, J. (2010a). A revolutionary graphitisation system: Fully automated, compact and simple. *Nuclear Instruments and Methods in Physics Research Section B: Beam Interactions with Materials and Atoms*, *268*(7), 931–934. https://doi.org/10.1016/j.nimb.2009.10.067

Wan, J., Tokunaga, T. K., Dong, W., Williams, K. H., Kim, Y., Conrad, M. E., Bill, M., Riley, W. J., & Hubbard, S. S. (2018). Deep Unsaturated Zone Contributions to Carbon Cycling in Semiarid Environments. *Journal of Geophysical Research: Biogeosciences*, *123*(9), 3045–3054. https://doi.org/10.1029/2018JG004669

Webster, K.D. et al. (2022) 'Diversity and Composition of Methanotroph Communities in Caves', *Microbiology Spectrum*, 10(4), pp. e01566-21. Available at: https://doi.org/10.1128/spectrum.01566-21.

Wiseschart, A., Mhuanthong, W., Thongkam, P., Tangphatsornruang, S., Chantasingh, D., & Pootanakit, K. (2018). Bacterial Diversity and Phylogenetic Analysis of Type II Polyketide Synthase Gene from Manao-Pee Cave, Thailand. *Geomicrobiology Journal*, 35, 518–527. https://doi.org/10.1080/01490451.2017.1411993

Weissert, H., & Mohr, H. (1996). Late Jurassic climate and its impact on carbon cycling. *Palaeogeography, Palaeoclimatology, Palaeoecology*, 122(1), 27–43. https://doi.org/10.1016/0031-0182(95)00088-7

Wingler, A., & Hennessy, D. (2016). Limitation of Grassland Productivity by Low Temperature and Seasonality of Growth. *Frontiers in Plant Science*, 7. https://doi.org/10.3389/fpls.2016.01130

Wu, J., Zhang, Q., Yang, F., lei, Y., Zhang, Q., & Cheng, X. (2017). Does short-term litter input manipulation affect soil respiration and its carbon-isotopic signature in a coniferous forest ecosystem of central China? *Applied Soil Ecology*, 113, 45–53. https://doi.org/10.1016/j.apsoil.2017.01.013

Zhang, H., Zhou, Z., Dong, H., Yan, L., Ding, S., Huang, J., Gong, X., & Su, D. (2023). Seasonal variations of cave dripwater hydrogeochemical parameters and δ13CDIC in the subtropical monsoon region and links to regional hydroclimate. *Science of The Total Environment,* 881, 163509. https://doi.org/10.1016/j.scitotenv.2023.163509

Zhou, J., Gu, Y., Zou, C., Mo, M. (2007). Phylogenetic diversity of bacteria in an earth-cave in Guizhou province, southwest of China. *The Journal of Microbiology,* 45(2).

Zhu, Y.-G., & Miller, R. M. (2003). Carbon cycling by arbuscular mycorrhizal fungi in soil–plant systems. *Trends in Plant Science*, 8(9), 407–409. https://doi.org/10.1016/S1360-1385(03)00184 5